Contents lists available at ScienceDirect

Advances in Colloid and Interface Science

journal homepage: www.elsevier.com/locate/cis

Calculation of scattering-patterns of ordered nano- and mesoscale materials

S. Förster [a,*], S. Fischer [b], K. Zielske [b], C. Schellbach [b], M. Sztucki [c], P. Lindner [d], J. Perlich [e]

[a] Physikalische Chemie I, Universität Bayreuth, Universitätsstrasse 30, D-95447 Bayreuth, Germany
[b] Institut für Physikalische Chemie, Universität Hamburg, Grindelallee 117, D-20146 Hamburg, Germany
[c] ESRF, 6 rue Jules Horowitz, F-38043 Grenoble Cedex 9, France
[d] Institut-Laue-Langevin, 6 rue Jules Horowitz, F-38042 Grenoble Cedex 9, France
[e] HASYLAB, DESY, Notkestrasse 85, D-22603 Hamburg, Germany

ARTICLE INFO

ABSTRACT

Analytical expressions for the scattering patterns of ordered nano- and mesoscopic materials are derived and compared to measured scattering patterns. Ordered structures comprising spheres (*fcc, bcc, hcp, sc,* and *bct*), cylinders (*hex* and *sq*), lamellae (*lam*) and vesicles, as well as bicontinuous cubic structures (*Ia3d, Pn3m,* and *Im3m*) are considered. The expressions take into account unit cell dimensions, particle sizes and size distributions, lattice point deviations, finite domain sizes, orientational distributions, core/shell-structures as well a variety of peak shapes. The expressions allow to quantitatively describe, model and even fit measured SAXS and SANS-patterns of ordered or oriented micellar solutions, lyotropic phases, block copolymers, colloidal solutions, nanocomposites, photonic crystals, as well as mesoporous materials.

© 2011 Published by Elsevier B.V.

Contents

* Corresponding author. Tel.: +49 921 552760; fax: +49 921 552780.
  E-mail address: forster@chemie.uni-hamburg.de (S. Förster).

1. Introduction

Modern materials science is achieving amazing control in assembling materials to provide desired functions and properties. Nano- and mesoscale building blocks of high regularity in size, shape and crystallinity are assembled into well-defined ordered superstructures. Building blocks include a wide variety of materials such as surfactants, lipids, block copolymers, nanoparticles, polymer colloids and biopolymers. The structures that can be realized become increasingly complex, consisting of multiple components and materials with sometimes hierarchically structured levels. Such materials are not only fascinating in their own right, but are also of great importance in biomedical applications, in catalysis, photonics, and in high-performance materials [1].

For the characterization of structural properties such as geometry, regularity, periodicity, order and orientation, scattering and diffraction techniques are naturally the most adequate methods. They are intrinsically sensitive to periodic and regular features since they detect the Fourier transform of the structure. With the advent of modern x-ray optics in sealed tube or rotating anode x-ray devices, and with the use of high-brilliance synchrotron-SAXS and SANS beamlines, high-resolution scattering patterns can now be obtained within short accumulation times (down to milliseconds) enabling a fast and detailed measurement and analysis of ordered nano- and mesoscopic materials over a size range of 1 nm up to several μm.

Knowledge, understanding, and control of the materials structure is at the core of current material science. The structural information that can be obtained from measured scattering patterns can greatly advance materials development and processing. However, a quantitative analysis of the scattering patterns of ordered or partially ordered nano- and mesoscale materials is much restricted by the lack of available modeling methods. Very often only a fraction of the available structural information, such as unit cell dimensions and space groups, are derived from measured scattering patterns. In view of the enormous progress on the experimental side, a significant step towards a more adequate data analysis is needed.

Here we present a mathematical treatment of the most common structures of nano- and mesoscale materials to calculate the corresponding scattering patterns using closed analytical expressions that allow fast numerical calculations and even fitting of measured scattering patterns. We consider the most prevalent building block shapes including spheres, cylinders, disks, and vesicles (hollow spheres) and the most common 1-dimensional (lamellae), 2-dimensional (hexagonal, square, centered rectangular), and 3-dimensional superstructures (bcc, fcc, hcp, sc, bct, gyroid, double diamond, plumbers nightmare). The most common structural imperfections such as polydispersity, lattice distortions, finite domain sizes, and orientational distributions are considered. The mathematical treatment is based on the decoupling approximation [2,3] that yields analytical expressions for the scattering patterns. We discuss advantages and limitations of the method and demonstrate – using examples from literature and own experiments – the applicability of this model to quantitatively describe high-resolution SAXS- and SANS-patterns of oriented cylindrical micelles, thermoplastic elastomers, lyotropic liquid crystals, nanocomposites, and mesoporous solids.

2. Experimental part

2.1. Small-angle neutron scattering at ILL, Grenoble

2.1.1. Shear-oriented cylindrical micelles

A Bohlin CVO stress-controlled rheometer was set-up in the neutron beam at D11 (ILL, Grenoble) for performing rheo-SANS experiments. The quartz shear cell consisted of an outer stator (48 mm diameter) and an inner rotor (46 mm diameter, Searle geometry) with a 1 mm gap and can be mounted in the radial and tangential beam direction to probe the orientational distribution of the micelles in the flow–vorticity plane and in the gradient–vorticity plane, respectively. This set-up allows to cover a range of shear rates $\dot{\gamma} = 0.2$–$1000\ \mathrm{s}^{-1}$. Data were collected on a 2D-^{3}He-filled area detector (64×64 pixels) at a distance of 5.0 m. The neutron wavelength was $\lambda = 0.6$ nm with $\Delta\lambda/\lambda = 9\%$. Details of the instrumentation and data reduction can be found elsewhere [4]. The sample was a 2% solution of a poly(butadiene-b-ethylene oxide) (PB-PEO) block copolymer in D_2O which forms cylindrical micelles that can easily be shear-oriented. The recorded scattering patterns at different shear rates are shown in Fig. 17 and compared to the calculated scattering patterns.

2.2. Synchrotron small-angle x-ray scattering at HASYLAB/DESY, Hamburg

2.2.1. Stretching of thermoplastic elastomers

The stretching experiments with the thermoplastic elastomers (SBS from Kraton) were performed with a homebuilt stretching device at the beamline BW4. It allows stretching elastic samples to a maximum distance of 640 mm with velocities between 0.1 and 1200 mm/min. The sample detector distance was $d = 4500$ mm and the wavelength was $\lambda = 0.1380$ nm. A CCD-detector (mar research) was used with a pixel size of 0.079 mm (2048×2048 pixels). The samples were prepared by roll-casting of concentrated solutions (35%) in toluene at a rotation speed of 80 rpm over 10 minutes. The recorded scattering pattern in the stretched state is shown in Fig. 18A and compared to the calculated scattering pattern.

2.2.2. Shear-oriented nanocomposite gel

The shear orientation experiments were performed at the beamline BW4. For shear-orientation a Linkam shear cell (CSS450) in oscillatory shear mode was used, which was equipped with Kapton windows. The sample was a 30% solution of polystyrene-coated magnetite nanoparticles in toluene. The recorded scattering pattern is shown in Fig. 19A and compared the calculated scattering pattern.

2.2.3. Rotating crystal measurement of mesoporous single crystal

A mesoporous silica single crystal was mounted on a goniometer at the beamline BW4 such that the 111-direction was parallel to the x-ray beam and the 110-direction was parallel to the direction vertical to the x-ray beam. The sample was rotated stepwise by 1° where at each angle the scattering patterns were measured. The sample was prepared by impregnating a shear-oriented lyotropic fcc phase with prehydrolyzed tetramethoxysilane, followed by solidification during a sol/gel-reaction. The preparation of the ordered mesoporous single crystal is described in refs. [5,6]. The recorded scattering patterns at a rotation angle of 39° is shown in Fig. 19B and compared to the calculated scattering pattern.

2.3. Synchrotron small-angle x-ray scattering at ESRF, Grenoble

2.3.1. Shear-oriented lyotropic phase

The rheo-SAXS experiments were performed at the beamline ID02 at ESRF, Grenoble. The Couette shear cell is built from polycarbonate consisting of an outer rotator (22 mm diameter) and an inner stator (20 mm diameter) with a 1 mm gap. The sample detector distance was $d = 5010$ mm. The detector was a FReLoN Kodak CCD-detector with 2048×2048 pixels. The sample was a solution of poly(isoprene-b-ethylene oxide) (PI-PEO) at a concentration of 17% in water, where it forms an fcc-phase that can be easily shear-oriented. The recorded scattering pattern after shearing at $500\ s^{-1}$ is shown in Fig. 18B and compared the calculated scattering pattern.

3. Scattering patterns of ordered particle systems

3.1. Coordinate system and scattering vector

For the calculation of scattering patterns we need to specify the orientation of particles and unit cells with respect to a laboratory-fixed coordinate system based on the three orthogonal unit vectors ($\mathbf{e}_x$, $\mathbf{e}_y$, $\mathbf{e}_z$). They are arranged such that the x-direction coincides with the x-direction of the detector, and the y-direction coincides with the y-direction of the detector as shown in Fig. 1. We assume the primary beam of wavelength λ is aligned in the direction $\mathbf{n} = -\mathbf{e}_z$. The wave vector $\mathbf{k}_i$ of the incoming beam is then given by

$$\mathbf{k}_i = \begin{pmatrix} k_{i,x} \\ k_{i,y} \\ k_{i,z} \end{pmatrix} = \frac{2\pi}{\lambda} \begin{pmatrix} 0 \\ 0 \\ -1 \end{pmatrix} \tag{1}$$
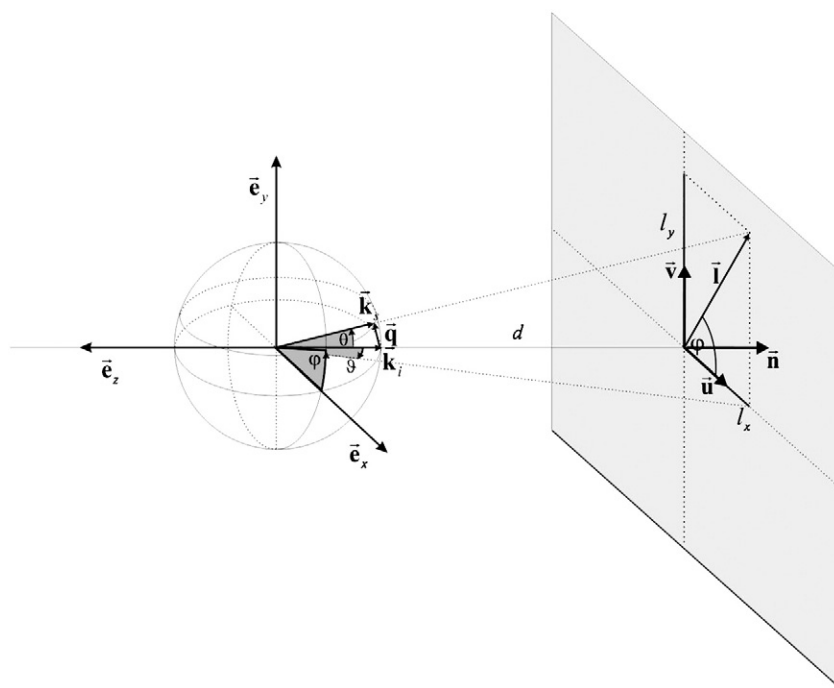
Fig. 1. Scheme showing the position and orientation of the detector specified in terms of the horizontal and vertical vectors **u** and **v**, the primary beam **n**, and the distance d to the sample. Also shown is the wave vector of the primary beam, $\mathbf{k}_i$, the scattered beam, $\mathbf{k}_s$, and the scattering vector **q**. All vectors are defined with respect to the lab-based coordinate system ($\mathbf{e}_x$, $\mathbf{e}_y$, $\mathbf{e}_z$) with the polar angles φ and ϑ and the scattering angle θ. l_x and l_y are the positions on the detector with respect to the position of the primary beam.

The wave vector $\mathbf{k}_s$ of the scattered beam can be specified by the polar angles φ and ϑ as shown in Fig. 1 and is given by

$$\mathbf{k}_s = \begin{pmatrix} k_{s,x} \\ k_{s,y} \\ k_{s,z} \end{pmatrix} = \frac{2\pi}{\lambda} \begin{pmatrix} \cos(\varphi)\sin(\vartheta) \\ \sin(\varphi)\sin(\vartheta) \\ -\cos(\vartheta) \end{pmatrix} \tag{2}$$

The moduli of the wave vectors are $|\mathbf{k}_i| = |\mathbf{k}_s| = 2\pi/\lambda$. The scattering vector $\mathbf{q}$ is defined by the difference $\mathbf{k}_s - \mathbf{k}_i$

$$\mathbf{q} = \begin{pmatrix} q_x \\ q_y \\ q_z \end{pmatrix} = \mathbf{k}_s - \mathbf{k}_i = \frac{2\pi}{\lambda} \begin{pmatrix} \cos(\varphi)\sin(\vartheta) \\ \sin(\varphi)\sin(\vartheta) \\ 1-\cos(\vartheta) \end{pmatrix} \tag{3}$$

In this coordinate system the scattering angle θ is equal to the polar angle ϑ. Using the identity $1 - \cos(\vartheta) = 2\sin^2(\vartheta/2)$ we obtain for the modulus of the scattering vector

$$q = |\mathbf{q}| = \frac{4\pi}{\lambda}\sin\left(\frac{\vartheta}{2}\right) = \frac{4\pi}{\lambda}\sin\left[\frac{1}{2}\arctan\left(\frac{l}{d}\right)\right] \tag{5}$$

where d is the distance between sample and detector. On the detector we define a vector

$$\mathbf{l} = \begin{pmatrix} l_x \\ l_y \\ 0 \end{pmatrix} = \begin{pmatrix} d\cos(\varphi)\tan(\vartheta) \\ d\sin(\varphi)\tan(\vartheta) \\ 0 \end{pmatrix} \tag{4}$$

of length $l = |\mathbf{l}| = d\tan(\vartheta)$. The scattering vector can also be expressed in terms of the vector $\mathbf{l}$ as

$$\mathbf{q} = \frac{2\pi}{\lambda} \begin{pmatrix} l_x\cos(\vartheta)/d \\ l_y\cos(\vartheta)/d \\ 1-\cos(\vartheta) \end{pmatrix}. \tag{6}$$

which is useful for later calculations in Section 4. For small angles $\vartheta \to 0$ we can approximate $\lim_{\vartheta \to 0}\cos(\vartheta) \approx 1$ so that the scattering vector becomes equal to

$$\lim_{\vartheta \to 0}\mathbf{q} = \frac{2\pi}{\lambda} \begin{pmatrix} l_x/d \\ l_y/d \\ 0 \end{pmatrix} = \frac{2\pi}{d\lambda}\mathbf{l} \tag{7}$$

with its z-component being equal to zero, $q_z = 0$. This will be later used for the consideration of the Ewald sphere which in this case can be approximated by its tangential plane. The approximation
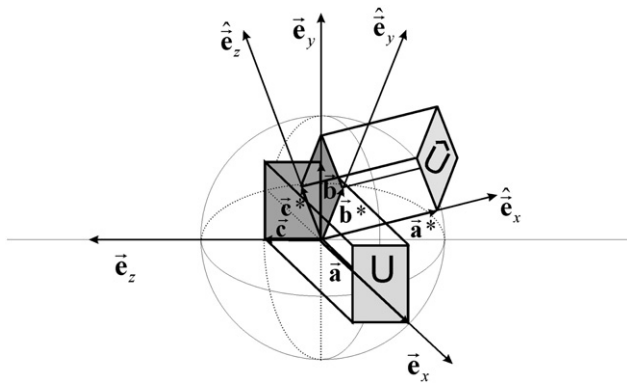

Fig. 2. Scheme showing the position and orientation of a unit cell **U** defined in terms of the orthonormal lab-based coordinate system $\mathbf{E} = (\mathbf{e}_x, \mathbf{e}_y, \mathbf{e}_z)$. Specific examples are given in Fig. 10. Also shown is the position and orientation of the rotated unit cell $\hat{\mathbf{U}}$ defined in terms of the orthonormal crystal-based coordinate system $\hat{\mathbf{E}} = (\hat{\mathbf{e}}_x, \hat{\mathbf{e}}_y, \hat{\mathbf{e}}_z)$, the set of direct space base vectors $\mathbf{A} = (\mathbf{a}, \mathbf{b}, \mathbf{c})$, and the set of reciprocal space base vectors $\mathbf{A}^* = (\mathbf{a}^*, \mathbf{b}^*, \mathbf{c}^*)$. The relation between $\mathbf{E}$ and $\hat{\mathbf{E}}$ is specified by the Eulerian angles corresponding to the rotation of the lab-based unit cell **U** to the actual unit cell $\hat{\mathbf{U}}$.

$\lim_{\vartheta \to 0}\cos(\vartheta) \approx 1$ leads to deviations of less than 0.1% of its exact value for angles <2.6° and deviations of less than 1% for values for angles <8°, which is the usual range of small-angle scattering experiments. Throughout the following calculations the general case of arbitrary values of the scattering angle ϑ is considered.

Positions and directions may be specified in terms of a vector $\mathbf{r}$ based on four different coordinate systems:

- the orthonormal lab coordinate system $\mathbf{E} = (\mathbf{e}_x, \mathbf{e}_y, \mathbf{e}_z)$ where a vector is specified in terms of the coordinates $\mathbf{r}_{xyz} = x\mathbf{e}_x + y\mathbf{e}_y + z\mathbf{e}_z = (x, y, z)$,
- the orthonormal crystal real space coordinate system $\hat{\mathbf{E}} = (\hat{\mathbf{e}}_x, \hat{\mathbf{e}}_y, \hat{\mathbf{e}}_z)$ where a vector is specified in terms of the coordinates $\mathbf{r}_{\hat{x}\hat{y}\hat{z}} = \hat{x}\hat{\mathbf{e}}_x + \hat{y}\hat{\mathbf{e}}_y + \hat{z}\hat{\mathbf{e}}_z = (\hat{x}, \hat{y}, \hat{z})$,
- the crystal direct space bases vector system $\mathbf{A} = (\mathbf{a}, \mathbf{b}, \mathbf{c})$ where a vector is specified in terms of the coordinates $\mathbf{r}_{uvw} = u\mathbf{a} + v\mathbf{b} + w\mathbf{c} = (u, v, w)$, and
- the crystal reciprocal space bases vector system $\mathbf{A}^* = (\mathbf{a}^*, \mathbf{b}^*, \mathbf{c}^*)$ where a vector is specified in terms of the coordinates $\mathbf{r}_{hkl} = h\mathbf{a}^* + k\mathbf{b}^* + l\mathbf{c}^* = (h, k, l)$, i.e. the Miller indices

The four coordinate systems $\mathbf{E}$, $\hat{\mathbf{E}}$, $\mathbf{A}$, and $\mathbf{A}^*$ are shown in Fig. 2. The set of reciprocal space vectors $\mathbf{A}^*$ is only co-linear with the set of orthonormal space vectors $\hat{\mathbf{E}}$ and the set of direct space base vectors $\mathbf{A}$ for rectangular unit cells (cubic, tetragonal, and orthorhombic), which is the case that is shown in Fig. 2. For hexagonal and other unit cells, they are linear combinations with orientations different from $\hat{\mathbf{E}}$ and $\mathbf{A}$.

The transformations between the three crystal-based coordinate systems $\hat{\mathbf{E}}$, $\mathbf{A}$, and $\mathbf{A}^*$ are given by

$$\mathbf{r}_{\hat{x}\hat{y}\hat{z}} = (\hat{x}, \hat{y}, \hat{z}) = \mathbf{M}^T\mathbf{r}_{uvw} = \mathbf{N}^T\mathbf{r}_{hkl} \tag{8}$$

$$\mathbf{r}_{uvw} = (u, v, w) = \left(\mathbf{M}^T\right)^{-1}\mathbf{r}_{\hat{x}\hat{y}\hat{z}} = \left(\mathbf{M}^T\right)^{-1}\mathbf{N}^T\mathbf{r}_{hkl} \tag{9}$$

$$\mathbf{r}_{hkl} = (h, k, l) = \left(\mathbf{N}^T\right)^{-1}\mathbf{r}_{\hat{x}\hat{y}\hat{z}} = \left(\mathbf{N}^T\right)^{-1}\mathbf{M}^T\mathbf{r}_{uvw} \tag{10}$$

with the matrices

$$\mathbf{M} = \begin{pmatrix} a & 0 & 0 \\ 0 & b & 0 \\ 0 & 0 & c \end{pmatrix} \quad \mathbf{N} = \begin{pmatrix} 1/a & 0 & 0 \\ 0 & 1/b & 0 \\ 0 & 0 & 1/c \end{pmatrix} \tag{11}$$

for rectangular unit cells (cubic, tetragonal, and orthorhombic), and

$$\mathbf{M} = \begin{pmatrix} a & 0 & 0 \\ -a/2 & \sqrt{3}a/2 & 0 \\ 0 & 0 & \sqrt{8/3}a \end{pmatrix} \quad \mathbf{N} = \begin{pmatrix} 1/a & 1/\left(\sqrt{3}a\right) & 0 \\ 0 & 2/\left(\sqrt{3}a\right) & 0 \\ 0 & 0 & \sqrt{3/8}/a \end{pmatrix} \tag{12}$$

for hexagonal lattices.

Following crystallographic conventions [7], throughout the manuscript crystallographic directions are given in terms of the Miller indices $\mathbf{r}_{hkl} = h\mathbf{a}^* + k\mathbf{b}^* + l\mathbf{c}^* = (h, k, l)$. In particular, the direction of the primary beam is specified by the vector $\mathbf{n}_{hkl} = h_n\mathbf{a}^* + k_n\mathbf{b}^* + l_n\mathbf{c}^* = (h_n, k_n, l_n)$. The coordinates (h_n, k_n, l_n) can be transformed into the crystal real space orthonormal coordinate system with a unit vector $\tilde{\mathbf{n}}_{\hat{x}\hat{y}\hat{z}} = \hat{x}_n\hat{\mathbf{e}}_x + \hat{y}_n\hat{\mathbf{e}}_y + \hat{z}_n\hat{\mathbf{e}}_z = (\hat{x}_n, \hat{y}_n, \hat{z}_n)$ using Eqs. (8) and (11) or (12). The respective direction in the lab-based coordinate system is given by the unit vector $\tilde{\mathbf{n}}_{xyz} = -\mathbf{e}_z = (0, 0, -1)$ (see Fig. 1). Further, the vector $\mathbf{u}_{hkl} = h_u\mathbf{a}^* + k_u\mathbf{b}^* + l_u\mathbf{c}^* = (h_u, k_u, l_u)$ orthogonal to the beam direction is given (see Fig. 1). It corresponds to the x-direction in the lab-based coordinate system. $\tilde{\mathbf{u}}_{xyz} = \mathbf{e}_x = (1, 0, 0)$ and specifies the orientation of the detector. The two vectors $\mathbf{n}_{hkl}$ and $\mathbf{u}_{hkl}$ define the orientation of the unit cell $\hat{\mathbf{U}}$.

The relation between vectors in the lab-based coordinate system and the crystal-based coordinate system can be expressed by the rotation matrix

$$\mathbf{R} = \begin{pmatrix} \cos\psi\,\cos\varphi - \sin\psi\,\cos\theta\,\sin\varphi & -\cos\psi\,\sin\varphi - \sin\psi\,\cos\theta\,\cos\varphi & \sin\psi\,\sin\theta \\ \sin\psi\,\cos\varphi + \cos\psi\,\cos\theta\,\sin\varphi & \cos\psi\,\cos\theta\,\cos\varphi - \sin\psi\,\sin\varphi & -\cos\psi\,\sin\theta \\ \sin\theta\,\sin\varphi & \sin\theta\,\cos\varphi & \cos\theta \end{pmatrix}$$

$$(13)$$

which is given in terms of the Eulerian angles (ψ, θ, φ). The angle ψ specifies the rotation around the z-axis $\mathbf{e}_z$, the angle θ the subsequent rotation around the new x-axis $\mathbf{e}'_x$, and φ the final rotation around the final z-axis $\mathbf{e}''_z$, whereby the unit cell $\mathbf{U}$ in the lab-based coordinate system is transformed into its rotated orientation in the primary beam, $\hat{\mathbf{U}}$. Since $\hat{\mathbf{U}}$ has been specified by the directions $\tilde{\mathbf{n}}_{\hat{x}\hat{y}\hat{z}}$ and $\tilde{\mathbf{u}}_{xyz}$, we can use the relation employing $\tilde{\mathbf{n}}_{\hat{x}\hat{y}\hat{z}}$

$$\tilde{\mathbf{n}}_{\hat{x}\hat{y}\hat{z}} = \begin{pmatrix} \hat{x} \\ \hat{y} \\ \hat{z} \end{pmatrix} = \mathbf{R}\tilde{\mathbf{n}}_{xyz} = \mathbf{R}\begin{pmatrix} 0 \\ 0 \\ -1 \end{pmatrix} = \begin{pmatrix} -\sin\psi\,\sin\theta \\ \cos\psi\,\sin\theta \\ -\cos\theta \end{pmatrix} \qquad (14)$$

and $\tilde{\mathbf{u}}_{xyz} = \mathbf{e}_x = (1,0,0)$

$$\tilde{\mathbf{u}}_{\hat{x}\hat{y}\hat{z}} = \begin{pmatrix} \hat{x}_u \\ \hat{y}_u \\ \hat{z}_u \end{pmatrix} = \mathbf{R}\tilde{\mathbf{u}}_{xyz} = \mathbf{R}\begin{pmatrix} 1 \\ 0 \\ 0 \end{pmatrix} = \begin{pmatrix} \cos\psi\,\cos\varphi - \sin\psi\,\cos\theta\,\sin\varphi \\ \sin\psi\,\cos\varphi + \cos\psi\,\cos\theta\,\sin\varphi \\ \sin\theta\,\sin\varphi \end{pmatrix}$$

$$(15)$$

to derive the Eulerian angles as

$$\theta = \arccos(-\hat{z}_n)$$
$$\psi = \arcsin(-\hat{x}_n / \sin\theta) \qquad\qquad (16)$$
$$\varphi = \arcsin(\hat{z}_u / \sin\theta)$$

These angles fully specify the rotation matrix $\mathbf{R}$, so that the coordinates of any vector in the lab-based coordinate system can be transformed into the corresponding coordinates of the crystal unit cell, and *vice versa*. i.e., $\mathbf{r}_{\hat{x}\hat{y}\hat{z}} = \mathbf{R}\mathbf{r}_{xyz}$ or $\mathbf{r}_{xyz} = \mathbf{R}^{-1}\mathbf{n}_{\hat{x}\hat{y}\hat{z}}$ with $\mathbf{R}^{-1}$ being the inverse matrix of $\mathbf{R}$. These equations are used in Section 4.1 (Eq. (99)) to calculate the real space projections of the unit cells from measured scattering patterns.

3.2. Scattered intensity and decoupling approximation

For a two-phase system consisting of particles (phase "1") with scattering length b_1 and volume fraction ϕ_1 in a matrix (phase "2") of scattering length b_2 and a volume fraction $\phi_2 = 1 - \phi_1$, separated by sharp interfaces, the scattered intensity per unit volume is given by [3,8,9]

$$I(\mathbf{q}) = (b_1 - b_2)^2 \rho_N F^2(\mathbf{q}) Z(\mathbf{q}) \qquad (17)$$

where $F(\mathbf{q})$ is the scattering amplitude or Fourier transform of the particle form, $\rho_N = N/V$ is the number density of the particles, $Z(\mathbf{q})$ is the lattice factor describing the spatial distribution of the particles, and $\mathbf{q}$ is the scattering vector. For x-ray, neutron, and light scattering experiments the scattering lengths b_i have units of [m], which together with the unit of the number density ρ_N (in [m^{-3}]) yields for the scattered intensity the usual units of [m^{-1}].

Eq. (17) is valid for monodisperse particles that are located exactly on the lattice points (see Fig. 3A). When the particles are displaced from the lattice points and the displacement probabilities can be described by a Gaussian function (thermal disorder) we have

$$I(\mathbf{q}) = (b_1 - b_2)^2 \rho_N \left[F^2(\mathbf{q})(1 - G(\mathbf{q})) + F^2(\mathbf{q})G(\mathbf{q})Z(\mathbf{q}) \right] \qquad (18)$$
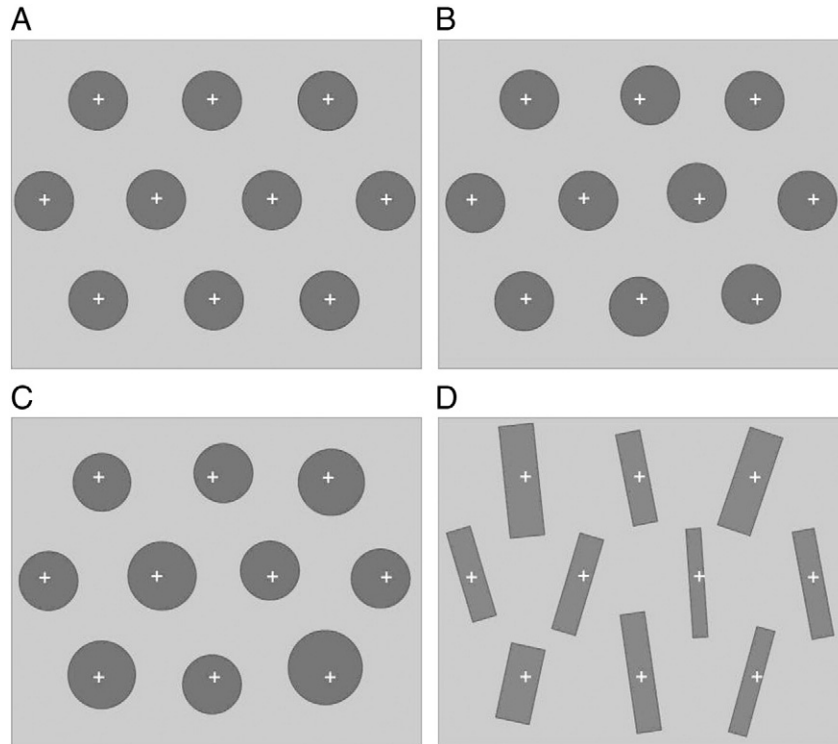
Fig. 3. Scheme showing the stepwise introduction of lattice disorder. Idealized lattice with monodisperse spherical particles exactly located on the lattice points (A), monodisperse spherical particles showing displacements from the lattice points (B), polydisperse spherical particles displaced from the lattice points (C), and partially oriented cylindrical particles with different lengths and widths displaced from their lattice points (D).
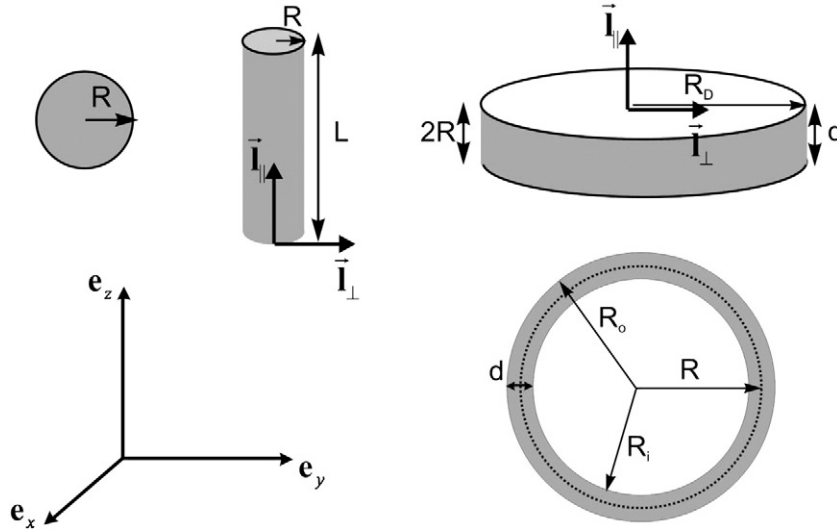
Fig. 4. Schematic representation of spheres, cylinders, disks, and vesicles with their characteristic dimensions and orientation with respect to the lab-based coordinate system ($\mathbf{e}_x$, $\mathbf{e}_y$, $\mathbf{e}_z$). R is the sphere radius, the cross-sectional cylinder radius, half the thickness of the disk, or the mean vesicle radius, L is the cylinder length, R_D the lateral disk radius, d the disk thickness or the vesicle bilayer thickness, R_o the outer radius of the vesicle, and R_i the inner radius of the vesicle. The unit vectors $\mathbf{l}_{II}$ and $\mathbf{l}_{\perp}$ specify the axial and cross-sectional direction.

$G(\mathbf{q})$ is known as the Debye–Waller factor. The second term in the brackets, $Z(\mathbf{q})G(\mathbf{q})$, describes the decay of the intensity of the Bragg peaks due to the displacements, whereas the first term, $1 - G(\mathbf{q})$, describes the concomitant increase of the diffuse scattering. For a perfect lattice, for which $G(\mathbf{q}) = 1$, Eq. (18) reduces to Eq. (17).

In the following we consider common particle shapes that include spherically symmetric particles such as spheres and vesicles, as well as anisometric particles such as cylinders and disks. Spheres are characterized by one parameter, their radius R. For vesicles and anisometric particles two parameters are needed, which for vesicles are their radius R and the thickness of the bilayer, d, for cylinders the length L and the cross-sectional radius R, and for disks the lateral disk radius R_D and the thickness d (Fig. 4). For the use of more generalized expressions for the particle form factor, it is useful to consider half the thickness of the disk being $R = d/2$.

For polydisperse particles it is necessary to specify their size distribution. For particles which are characterized by two structural parameters, the corresponding size distributions are assumed to be independent, which is generally a very good approximation. To be specific, we will in the following give the equations for cylinders, characterized two structural parameters, i.e. the length L and the cross-sectional radius R. For disks and vesicles, analogous equations can be derived, where the final equations are summarized in Tables 1 and 2.

For the calculation of the scattered intensity of cylinders, the dependence on the variables L and R has to be considered in the

scattering amplitudes $F(\mathbf{q}, L, R)$. Therefore for polydisperse cylinders Eq. (18) has to be rewritten as

$$I(\mathbf{q}) = (b_1 - b_2)^2 \rho_N \left[\left\langle F^2(\mathbf{q}, L, R) \right\rangle_{L,R} + \left\langle F(\mathbf{q}, L, R) \right\rangle_{L,R}^2 G(\mathbf{q})(Z(\mathbf{q}) - 1) \right]$$

(19)

where $\langle \dots \rangle_{L,R}$ denotes the average over the distributions of lengths L and radii R. In the monodisperse case, $\langle F^2(\mathbf{q}, L, R) \rangle_{L,R} = \langle F(\mathbf{q}, L, R) \rangle_{L,R}^2 = F^2(\mathbf{q}, L, R)$, so that the Eq. (19) reduces to Eq. (18).

In case of anisometric particles we have to further consider their spatial orientation. For cylinders, the scalar quantities L and R are associated with the vectors $\mathbf{L} = L\mathbf{l}_{II}$ and $\mathbf{R} = R\mathbf{l}_{\perp}$, where $\mathbf{l}_{II}$ and $\mathbf{l}_{\perp}$ are unit vectors in direction of the cylinder axis and perpendicular to the cylinder axis, respectively (see Fig. 4). Also the spatial orientation of the unit cell has to be specified. This can be done by giving the orientation of the reciprocal lattice vectors $\mathbf{g}$. For a given orientational distribution of the particles and their unit cells, Eq. (19) is then rewritten as

$$I(\mathbf{q}) = (b_1 - b_2)^2 \rho_N \left[\left\langle \left\langle F^2(\mathbf{q}, \mathbf{L}, \mathbf{R}) \right\rangle_{L,R} - \left\langle F(\mathbf{q}, \mathbf{L}, \mathbf{R}) \right\rangle_{L,R}^2 G(\mathbf{q}, \mathbf{g}) \right. \right.$$

(20)

$$\left. \left. + \left\langle F(\mathbf{q}, \mathbf{L}, \mathbf{R}) \right\rangle L, R 2 G(\mathbf{q}, \mathbf{g}) Z(\mathbf{q}, \mathbf{g}) \right\rangle_{or} \right]$$

where $\langle \dots \rangle_{or}$ denotes the average over the orientational distribution.

In Eq. (20) we have to consider the orientational distribution of the particles which affects the scattering amplitude $F(\mathbf{q})$, and the orientational distribution of the unit cells, which affects the lattice factor $Z(\mathbf{q})$. Because unit cells are defined by the location and orientation of the particles that they contain, the orientational distribution of particles and unit cells should be the same. The following treatment of the orientational distribution is motivated by the observation that typically in nano- and mesoscale materials [10] the lattice structure is subdivided into a large number of small ordered domains. The orientational distribution of the particles is then a result of the orientational distribution of the particles within the domains, and the orientational distribution of the domains. The orientational distribution may be nearly uniform inside a domain. Adjacent domains may have different, mutually uncorrelated orientations. Such a domain structure is schematically shown in Fig. 5. If the orientations of the domains are similar (Fig. 5D), this results in a mosaic-type domain

Table 1
Weight-factors m for longitudinal and cross-sectional scattering amplitudes and form factors for homogeneous particles needed for the evaluation of the integral in Eq. (42). The volume of a vesicle is approximated as $V = 4\pi R^2 d + \frac{\pi}{3} d^3 \approx 4\pi R^2 d$ for $d \ll R$.

Geometry	Volume	Function	Variable	m
Sphere	$V = \frac{4\pi}{3} R^3$	$\langle P(q, R) \rangle$	R	6
Cylinder	$V = \pi R^2 L$	$\langle F_{d\|\|}(q, L) \rangle_L, \langle F_{d\|\|}^2(q, L) \rangle_L$	L	2
		$\langle F_{d\perp}(q, R) \rangle_R, \langle F_{d\perp}^2(q, R) \rangle_R$	R	4
Disk	$V = 2\pi R_D^2 R$	$\langle F_{d\|\|}(q, R_d) \rangle_{R_D}, \langle F_{d\|\|}^2(q, R_d) \rangle_{R_D}$	R_D	4
		$\langle F_{d\perp}(q, R) \rangle_R, \langle F_{d\perp}^2(q, R) \rangle_R$	R	2
Vesicle*	$V \cong 4\pi R^2 d$	$\langle \dots \rangle_R$	R	4
		$\langle \dots \rangle_d$	d	2

Table 2
Summary of formfactors $P(q)$ and longitudinal and cross-sectional scattering amplitudes $F(q)$ for the particles considered in the calculations. Also given are the Porod-asymptotes $P_{d\infty}$ of the form factors for the isotropic case and the particle volumes V_{dp}. The arguments of the hypergeometric functions $_1F_2(x)$ and $_2F_3(x)$ involve the z-weighted mean radius $R_z = \bar{R}/(z+1)$. The subscripts R and d denote the variable, with respect to which the average over the size distribution has been taken.

Spheres	$\langle F_3(q,R)\rangle = 3\left(\left\langle \dfrac{\sin(qR)}{(qR)^3}\right\rangle - \left\langle\dfrac{\cos(qR)}{(qR)^2}\right\rangle\right)$	T1
	$\langle F_3^2(q,R)\rangle = 9\left(\left\langle\dfrac{\sin^2(qR)}{(qR)^6}\right\rangle - 2\left\langle\dfrac{\sin(qR)\cos(qR)}{(qR)^5}\right\rangle + \left\langle\dfrac{\cos^2(qR)}{(qR)^4}\right\rangle\right)$	T2
	$P_{3\infty} = \dfrac{9}{2R^4}$ $\qquad\qquad$ $V_{3p} = \dfrac{4\pi R^3}{3}$	
Cylinders	$\langle F_2(\mathbf{q},\mathbf{L},\mathbf{R})\rangle_{L,R} = \langle F_2(\mathbf{q},\mathbf{L})\rangle_L \langle F_\perp(\mathbf{q},\mathbf{R})\rangle_R$	T3
	$\langle F_{2\parallel}(\mathbf{q},\mathbf{L})\rangle_L = \left\langle\dfrac{\sin(\mathbf{qL}/2)}{(\mathbf{qL}/2)}\right\rangle_L$	T4
	$\langle F_{2\perp}(\mathbf{q},\mathbf{R})\rangle_R = {_2}F_1\left[\dfrac{z+m+1}{2},\dfrac{z+m+2}{2},2;-(\mathbf{qR}_z)^2\right]$	T5
	$\langle F_2^2(\mathbf{q},\mathbf{L},\mathbf{R})\rangle_{L,R} = \langle F_{2\parallel}^2(\mathbf{q},\mathbf{L})\rangle_L \langle F_{2\perp}^2(\mathbf{q},\mathbf{R})\rangle_R$	T6
	$\left\langle F_{2\parallel}^2(\mathbf{q},\mathbf{L})\right\rangle_L = \left\langle\dfrac{\sin^2(\mathbf{qL}/2)}{(\mathbf{qL}/2)^2}\right\rangle_L$	T7
	$\langle F_{2\perp}^2(\mathbf{q},\mathbf{R})\rangle_R = {_3}F_2\left[\dfrac{3}{2},\dfrac{z+m+1}{2},\dfrac{z+m+2}{2},2,3;-4(\mathbf{qR}_z)^2\right]$	T8
	$P_{2\infty} = \dfrac{4}{LR^3}$ $\qquad\qquad$ $V_{2p} = \pi R^2 L$	
Disks	$\langle F_1(\mathbf{q},\mathbf{R}_D,\mathbf{R})\rangle_{R_D,R} = \langle F_1(\mathbf{q},\mathbf{R}_D)\rangle_{R_D}\langle F_{1\perp}(\mathbf{q},\mathbf{R})\rangle_R$	T9
	$\left\langle F_{1\parallel}(\mathbf{q},\mathbf{R}_D)\right\rangle = {_2}F_1\left[\dfrac{z+m+1}{2},\dfrac{z+m+2}{2},2;-(\mathbf{qR}_{Dz})^2\right]$	T10
	$\langle F_{1\perp}(\mathbf{q},\mathbf{R})\rangle = \left\langle\dfrac{\sin(\mathbf{qR})}{(\mathbf{qR})}\right\rangle$	T11
	$\langle F_1^2(\mathbf{q},\mathbf{R}_D,\mathbf{R})\rangle_{R_D,R} = \langle F_1^2(\mathbf{q},\mathbf{R}_D)\rangle_{R_D}\langle F_{1\perp}^2(\mathbf{q},\mathbf{R})\rangle_R$	T12
	$\left\langle F_{1\parallel}^2(\mathbf{q},\mathbf{R}_D)\right\rangle_{R_D} = {_3}F_2\left[\dfrac{3}{2},\dfrac{z+m+1}{2},\dfrac{z+m+2}{2},2,3;-4(\mathbf{qR}_{Dz})^2\right]$	T13
	$\langle F_{1\perp}^2(\mathbf{q},\mathbf{R})\rangle_R = \left\langle\dfrac{\sin^2(\mathbf{qR})}{(\mathbf{qR})^2}\right\rangle_R$	T14
	$P_{1\infty} = \dfrac{1}{R_D^2 R^2}$ $\qquad\qquad$ $V_{1p} = \pi d R_D^2$	
Vesicles	$\langle F(q,R,d)\rangle = \dfrac{1}{\left(1+\frac{d^2}{12R^2}\right)}\left[\left\langle\dfrac{\cos x_R}{x_R^2}\right\rangle_R\left\langle\dfrac{\sin x_d}{x_d}\right\rangle_d - \left\langle\dfrac{\cos x_R}{x_R^2}\right\rangle_R\langle\cos x_d\rangle_d + \left\langle\dfrac{\sin x_R}{x_R}\right\rangle_R\left\langle\dfrac{\sin x_d}{x_d}\right\rangle_d\right]$	T15
	$\langle F^2(q,R,d)\rangle = \dfrac{1}{\left(1+\frac{d^2}{12R^2}\right)^2}\left[\left\langle\dfrac{\sin^2 x_R}{x_R^4}\right\rangle_R\left\langle\dfrac{\sin^2 x_d}{x_d^2}\right\rangle_d - 2\left\langle\dfrac{\sin x_R\cos x_R}{x_R^3}\right\rangle_R\left\langle\dfrac{\sin x_d\cos x_d}{x_d}\right\rangle_d + 2\left\langle\dfrac{\sin x_R\cos x_R}{x_R^3}\right\rangle_R\left\langle\dfrac{\sin^2 x_d}{x_d^2}\right\rangle_d$	T16
	$\qquad + \left\langle\dfrac{\cos^2 x_R}{x_R^4}\right\rangle_R\langle\cos^2 x_d\rangle_d - 2\left\langle\dfrac{\cos^2 x_R}{x_R^4}\right\rangle_R\left\langle\dfrac{\sin x_d\cos x_d}{x_d}\right\rangle_d + \left\langle\dfrac{\cos^2 x_R}{x_R^4}\right\rangle_R\left\langle\dfrac{\sin^2 x_d\cos x_d}{x_d^2}\right\rangle_d\right]$	
	$P_{3\infty} = \dfrac{1}{4R^2 d^2}$ $\qquad\qquad$ $V = 4\pi R^2 d + \frac{\pi}{3}d^3 \approx 4\pi R^2 d$ for $d \ll R$.	

structure. This type of domain structure is usually found in soft nano- and mesoscale materials that have been oriented by external fields. If the orientational distribution of the cylinders within the domains is sufficiently uniform, the measured orientational distribution is practically identical to the orientational distribution of the domains. If the orientation of the domains is sufficiently uniform, the measured orientational distribution function is practically identical to the orientational distribution of the cylinders within the domains. This is more formally treated in the Appendix (Section A.1).

If the lattice factor function $Z(\mathbf{q})$ is sufficiently peaked and the domains are sufficiently oriented as for mosaic-type domain structures, then according to Eq. (A4) the orientational average of the product of the formfactor and the lattice factor, as in Eq. (20) can be factorized into the orientational average of the scattering amplitude $F(\mathbf{q})$ and the orientational average of the lattice factor $Z(\mathbf{q})$, i.e.

$$\left\langle\left\langle F(\mathbf{q},\mathbf{L},\mathbf{R})\right\rangle_{L,R}^2 G(\mathbf{q},\mathbf{g})Z(\mathbf{q},\mathbf{g})\right\rangle_{or} = \left\langle\left\langle F(\mathbf{q},\mathbf{L},\mathbf{R})\right\rangle_{L,R}^2\right\rangle_{or}\langle G(\mathbf{q},\mathbf{g})Z(\mathbf{q},\mathbf{g})\rangle_{or}$$

(21)

The orientational distribution results in an azimuthal intensity distribution of the scattering amplitude $F(\mathbf{q})$ and affects the azimuthal peak width of the Bragg-peaks in the lattice factor $Z(\mathbf{q})$. However, for structures with small, nanometer-sized domains such as depicted in Fig. 5, the peak width will mainly be determined by the domain size. The effect of the orientational distribution on the peak width is mostly negligible, but can be implicitly considered within a more general treatment that involves the lattice coherence, which provides a relation between peak widths, domain sizes and orientational distributions, which will be outlined in Section 3.9.

Only for the case of sufficiently large domains with broad orientational distributions would the orientational distribution determine the azimuthal intensity distribution of the peaks. For a discrete number of large domains this distribution of crystallographic orientations is called 'texture'. In this case, one can always use the exact calculation employing Eq. (20). For nano- and mesoscale system with mosaic-type domain structures such as in Fig. 5, Eq. (21) is a very good approximation for the calculation of scattering patterns. If the orientational distributions of adjacent domains are uncorrelated, the azimuthal peak width is q-independent. The examples shown in Section 4 and the vast majority of examples found in literature show this to be quite generally the case.
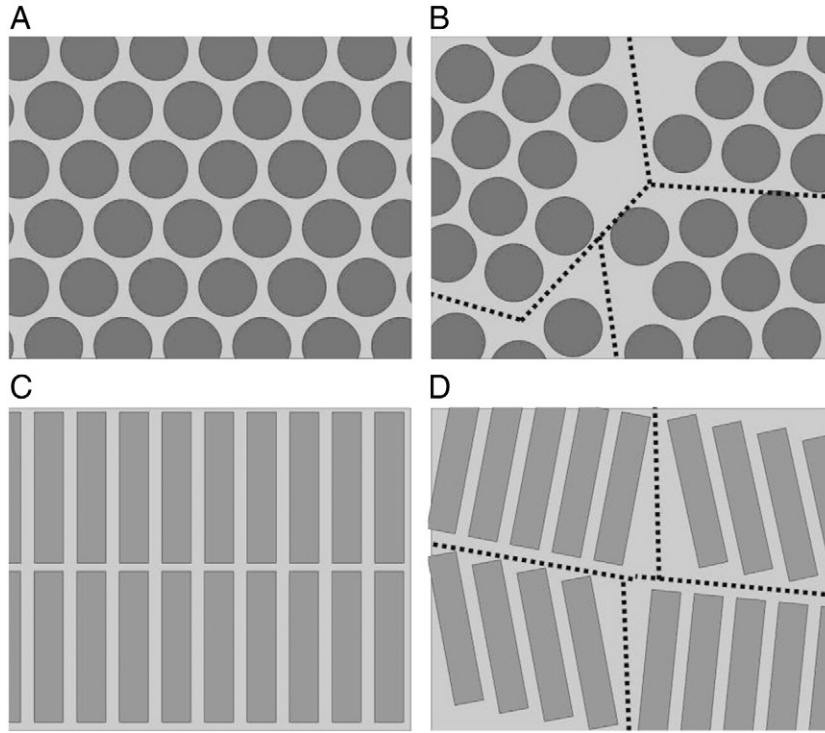
Fig. 5. Scheme of a perfect single crystalline lattice of ordered spheres (A) and the corresponding macroscopically isotropic multi-domain structure consisting of small nanoscale domains (B). Also shown is a perfect single crystalline lattice of ordered, perfectly oriented cylinders (C) and a partially oriented multi-domain structure consisting of a mosaic-type arrangement of similarly oriented nanoscale domains (D). Within the domains there is perfect positional and orientational order. The formation of domains is typical for ordered mesoscale structures.

We further assume that the Debye–Waller factor is isotropic, which implies that the mean deviations from the lattice points are the same in all directions, which is generally a good approximation for mesoscale materials, so that $\langle G(\mathbf{q},\mathbf{g})Z(\mathbf{q},\mathbf{g})\rangle_{or} = \langle Z(\mathbf{q},\mathbf{g})\rangle_{or}G(q,g)$. Then Eq. (20) can be recast in the form

$$I(\mathbf{q}) = (b_1 - b_2)^2 \rho_N \left\langle \left\langle F^2(\mathbf{q},\mathbf{L},\mathbf{R}) \right\rangle_{L,R} \right\rangle_{or} \left[1 + \frac{\left\langle \left\langle F(\mathbf{q},\mathbf{L},\mathbf{R}) \right\rangle_{L,R}^2 \right\rangle_{or}}{\left\langle \left\langle F^2(\mathbf{q},\mathbf{L},\mathbf{R}) \right\rangle_{L,R} \right\rangle_{or}} (\langle Z(\mathbf{q},\mathbf{g})\rangle_{or} - 1)G(q,g) \right]$$

(22)

By introducing the ratio

$$\beta(\mathbf{q},\mathbf{L},\mathbf{R}) = \frac{\left\langle \left\langle F(\mathbf{q},\mathbf{L},\mathbf{R}) \right\rangle_{L,R}^2 \right\rangle_{or}}{\left\langle \left\langle F^2(\mathbf{q},\mathbf{L},\mathbf{R}) \right\rangle_{L,R} \right\rangle_{or}}$$

(23)

and the formfactor

$$P(\mathbf{q},\mathbf{L},\mathbf{R}) = \left\langle F^2(\mathbf{q},\mathbf{L},\mathbf{R}) \right\rangle_{L,R}$$

(24)

we can rewrite the Eq. (22) in a more convenient form as

$$I(\mathbf{q}) = (b_1 - b_2)^2 \rho_N \langle P(\mathbf{q},\mathbf{L},\mathbf{R})\rangle_{or} [1 + \beta(\mathbf{q},\mathbf{L},\mathbf{R})(\langle Z(\mathbf{q},\mathbf{g})\rangle_{or} - 1)G(q,g)]$$

(25)

The effect of the ratio $\beta(\mathbf{q},\mathbf{L},\mathbf{R})$ on the scattered intensity is similar to the Debye–Waller factor, resulting in a decay of the Bragg-intensities with increasing scattering vector q. Eq. (25) is the main equation that is used for the calculation of scattering patterns throughout the following sections. Eq. (25) considers the effect of the particles – via their first and second moment of the particle size distribution that affect the formfactor and the ratio β – and of the

lattice – via the first and second moment of the distribution of lattice points that affect the lattice factor and the Debye–Waller factor – on the scattered intensity $I(q)$. Both effects lead to damping of the higher order Bragg-reflections [3].

3.3. Particle form factors

Since spheres are isometric particles, the scattering amplitude depends only on the moduli of the scattering vector q and the radius R. The scattering amplitude for spheres of radius R is given by

$$F_3(q,R) = \frac{3}{(qR)^3}(\sin(qR) - qR\cos(qR))$$

(26)

The index "3" refers to the dimensionality of the particle which is $d = 1$ for lamellae or bilayers, $d = 2$ for cylinders, and $d = 3$ for spheres. The scattering amplitude $F(\mathbf{L},\mathbf{R},\mathbf{q})$ for cylindrical particles of cross-sectional radius R and length L can be factorized into

$$F_2(\mathbf{q},\mathbf{L},\mathbf{R}) = F_{2\parallel}(\mathbf{q},\mathbf{L})F_{2\perp}(\mathbf{q},\mathbf{R})$$

(27)

where $F_{2\parallel}(\mathbf{q},\mathbf{L})$ is the longitudinal contribution parallel to the cylinder axis, and $F_{2\perp}(\mathbf{q},\mathbf{R})$ is the contribution from the cross-section of the cylinder. The longitudinal and cross-sectional contributions for cylinders are given by

$$F_{2\parallel}(\mathbf{q},\mathbf{L}) = \frac{\sin(\mathbf{q}\mathbf{L}/2)}{\mathbf{q}\mathbf{L}/2}$$

(28)

$$F_{2\perp}(\mathbf{q},\mathbf{R}) = \frac{2J_1(\mathbf{q}\mathbf{R})}{\mathbf{q}\mathbf{R}}$$

(29)

where $J_1(z)$ is the Bessel function of the first kind.

The structure of disks can be described by their lateral radius R_D and half the thickness of the disk R. Since disks could equivalently been considered to be very short cylinders, where the cross-sectional radius R is larger than the length L, the scattering amplitudes can be obtained by substituting $\mathbf{L}/2 \rightarrow \mathbf{R}$ and $\mathbf{R} \rightarrow \mathbf{R}_D$ in Eqs. (27)–(29) to obtain

$$F_1(\mathbf{q}, \mathbf{R}_D, \mathbf{R}) = F_{1\parallel}(\mathbf{q}, \mathbf{R}_D,) F_{1\perp}(\mathbf{q}, \mathbf{R}) \tag{30}$$

where $F_{1\parallel}(\mathbf{q}, \mathbf{R}_D)$ is now the contribution in the lateral direction and $F_{1\perp}(\mathbf{q}, \mathbf{R})$ is the contribution from the cross-section of the disk. The normal and cross-sectional contributions for disks are given by

$$F_{1\parallel}(\mathbf{q}, \mathbf{R}_D) = \frac{2J_1(\mathbf{qR}_D)}{\mathbf{qR}_D} \tag{31}$$

$$F_{1\perp}(\mathbf{q}, \mathbf{R}) = \frac{\sin(\mathbf{qR})}{\mathbf{qR}} \tag{32}$$

A vesicle is characterized by the radius R and the thickness of the bilayer d. Since vesicles are isometric particles, the scattering amplitude depends only on the moduli of the scattering vector q and the structural parameters R and d. For vesicles with a homogeneous bilayer the scattering amplitude can be calculated from the integral

$$F(q, R, d) = \frac{\int\limits_{R-d/2}^{R+d/2} \frac{\sin(qr)}{qr} 4\pi r^2 dr}{\int\limits_{R-d/2}^{R+d/2} 4\pi r^2 dr} \tag{33}$$

where R is the radius of the vesicle taken to be at the center of the bilayer (see Fig. 4). Evaluating the integral and recasting the resulting cosine and sine functions as functions of either R or d, one obtains

$$F(q, R, d) = \frac{1}{\left(1 + \frac{d^2}{12R^2}\right)} \left[\frac{\cos x_R}{x_R^2} \frac{\sin x_d}{x_d} - \frac{\cos x_R}{x_R^2} \cos x_d + \frac{\sin x_R}{x_R} \frac{\sin x_d}{x_d} \right] \tag{34}$$

where $x_R = qR$ and $x_d = qd/2$.

The isotropic form factors $P(q, L, R)$ (Eq. (24)) have the asymptotes

$$\lim_{q \to \infty} q^4 P(q) = P_{d\infty} \tag{35}$$

where the $P_{d\infty}$ are given in Table 2 together with the particle volumes V_{dp}. It provides a useful relation to Porod's law

$$V \lim_{q \to \infty} q^4 I(q) = 2\pi (b_1 - b_2)^2 S_V \tag{36}$$

where S_V is the surface area per volume. For an isotropic, dilute system where $Z(q) = 1$, the scattered intensity (Eq. (17)) for a given volume V becomes $VI(q) = (b_1 - b_2)^2 NP(q)$. If for the case of $N = 1$ particles this is inserted into Eq. (36), it reduces to the identity $V_{dp}(b_1 - b_2)^2 P_{d\infty} = 2\pi(b_1 - b_2)^2 S_V$ with the volume of the particle, V_{dp}, and the asymptote $P_{d\infty}$ given in Table 2.

3.4. Core–shell structures

The factorization of the scattering amplitude into a contribution $F_{d\parallel}(\mathbf{q})$ and $F_{d\perp}(\mathbf{q})$ allows a straightforward extension to include also core-shell structures. For this the cross-sectional part $F_{d\perp}(\mathbf{q})$ has to be modified to include also the contributions and interferences with the shells as outlined in [11]. It considers the case of homogeneous cores and shells, as well as the case of homogeneous cores and inhomogeneous shells exhibiting density profiles of the form $\rho \sim r^{-\alpha}$ (scaling laws) characteristic for spherical ($d = 3$), cylindrical ($d = 2$) and planar ($d = 1$) polymer

brushes. The scattering amplitude for the cross-section of a d-dimensional core-shell particle is then given by

$$F_{d\perp}(\mathbf{q}, \mathbf{R}_c, \mathbf{R}_m, \alpha) = \frac{\left[\frac{1}{d} F_d(\mathbf{q}, \mathbf{R}_c, 0) - \frac{\rho}{(d-\alpha)} F_d(\mathbf{q}, \mathbf{R}_c, \alpha) + \frac{\rho p^{\alpha-d}}{(d-\alpha)} F_d(\mathbf{q}, \mathbf{R}_m \alpha) \right]}{\left[\frac{1}{d} - \frac{\rho}{(d-\alpha)} + \frac{\rho p^{\alpha-d}}{(d-\alpha)} \right]} \tag{37}$$

where

$$F_d(\mathbf{q}, \mathbf{R}, \alpha) = {}_1F_2\left[\frac{d-\alpha}{2}, \frac{d}{2}, \frac{d+2-\alpha}{2}; -\frac{(\mathbf{qR})^2}{4} \right] \tag{38}$$

$\rho = \frac{\rho_s}{\rho_c}$ is the ratio of the scattering contrast of the shell, ρ_s, and the core, ρ_c, at the core/shell interface, and $p = R_c/R_m$ is the ratio of core radius, R_c, and overall radius, R_m. For homogeneous shells of constant density ($\alpha = 0$), Eq. (37) reduces to

$$F_{d\perp}(\mathbf{q}, \mathbf{R}_c, \mathbf{R}_m) = \frac{\left[(1-\rho)_0 F_1\left[\frac{(d+2)}{2}; -\frac{(\mathbf{qR}_c)^2}{4} \right] + \rho p^{-d}{}_0 F_1\left[\frac{(d+2)}{2}; -\frac{(\mathbf{qR}_m)^2}{4} \right] \right]}{\left[1 - \rho(1-p^{-d}) \right]} \tag{39}$$

for which the respective expressions ${}_0F_1[x]$ for spheres, cylinders and lamellae have been compiled in ref. [11]. ${}_0F_1[x]$ and ${}_1F_2[x]$ are hypergeometric functions that are defined in the Appendix (Section A.4). For homogenous particles ($p = 1$ or $\rho = 1$), Eq. (39) reduces further to $F_{d\perp}(\mathbf{q}, \mathbf{R}_m)$, and for $\rho = 0$ to $F_{d\perp}(\mathbf{q}, \mathbf{R}_c)$ as given in Eq. (26) for $d = 3$, Eq. (29) for $d = 2$, and Eq. (32) for $d = 1$.

It is straightforward to consider also other polymer or colloid structures with their respective form factors $P(q)$ and structure factors $Z_0(q)$ which e.g. are well compiled in [12].

3.5. Particle size distribution

The scattered intensity I for a distribution of particles of different sizes is the z-average defined by

$$I_z = \frac{\sum_i I_i n_i m_i^2}{\sum_i n_i m_i^2} \tag{40}$$

where n_i is the number of particles with mass m_i. For homogeneous particles the mass can be related to the volume by $m_i = \rho V_i$. For spheres the volume is given by $V_i = \frac{4\pi}{3} R_i^3$. Substitution and writing as an integral we have

$$I_z = \frac{\int\limits_0^\infty I(R) n(R) R^m dR}{\int\limits_0^\infty n(R) R^m dR} \tag{41}$$

where for the special case of spheres we would have an exponent $m = 6$. Particles of other geometries such as cylinders or disks have different relations between volume and dimension which together with the corresponding exponent m are given in Table 1.

For the calculation of the averages in case of cylinders, disks and vesicles the form factors can be factorized and integrated with respect to each of the variables $X = L, R_D, d, R$. In many cases, the Schulz–Zimm is a useful distribution that can be used for the number distribution of the particles, so that one obtains for the z-averages of a function $f(q, X)$

$$\langle f(q, X) \rangle_X = \int\limits_0^\infty f(q, X) X^m h(X) dX \tag{42}$$

with

$$h(X) = \frac{(z+1)^{z+m+1}X^z}{\overline{X}^{z+m+1}\Gamma(z+m+1)}\exp\left[-(z+1)\frac{X}{\overline{X}}\right] \qquad (43)$$

with m the weighting factor for the variable X, the average $\overline{X}$, and the relative standard deviation $\sigma_X = (z+1)^{-1/2}$. The distribution is normalized such that $\int_0^\infty X^m h(X)dX = 1$.

For the Schulz–Zimm-distribution the mean square radius is given by (see Appendix, Section A.4)

$$\langle x^2 \rangle_z = \frac{(z+m+1)(z+m+2)}{(z+1)^2}\overline{X}^2 \qquad (44)$$

which for very small σ_X reduces to $\langle x^2\rangle_z = \overline{X}^2$. Otherwise $\langle x^2\rangle_z > \overline{X}^2$, because the larger particles contribute stronger to the average value.

The averages for the particle scattering amplitudes and form factors can be analytically calculated according to Eqs. (42) and (43) and are summarized in Table 2. The expressions for vesicles (Eqs. (T15) and (T16)) are an approximation where the prefactors $\left(1+\frac{d^2}{12R^2}\right)^{-1}$ and $\left(1+\frac{d^2}{12R^2}\right)^{-2}$ have been assumed to be independent of both size distributions to separate the variables R and d in the sine and cosine functions in order to obtain a closed analytical solution. This assumption is a very good approximation for large vesicles, i.e. $R \gg d$, for which the prefactor is approximately equal to unity. Even for the case of relatively small vesicles with $R > 4d$, the prefactor deviates from unity only by < 1%.

3.6. Orientational distributions

For anisometric particles such as cylinders and disks, the orientational distribution has to be explicitly taken into account. The orientational distribution of the particles can be obtained by averaging the scattering amplitudes $\langle F(\mathbf{q},\mathbf{L},\mathbf{R})\rangle_{L,R}$ and $\langle F^2(\mathbf{q},\mathbf{L},\mathbf{R})\rangle_{L,R}$ over a distribution of angles β between the cylinder axis or lateral direction of the disk, $\mathbf{l}_\parallel$, and the scattering vector $\mathbf{q}$. We will first consider the orientational average for cylinders. The scalar products

Fig. 6. Different types of distribution functions as a function of the deviation angle δ. The steepness of the distribution increases from the Onsager-, Boltzmann-, Maier-Saupe-, Gauss-, Laguerre- to the Heaviside-function.

are $\mathbf{qL} = L\mathbf{q}\mathbf{l}_\parallel = qL\cos\beta$ and $\mathbf{qR} = R\mathbf{q}\mathbf{l}_\perp = qR\sin\beta$. The orientational average is then calculated as

$$\left\langle \langle F_2^2(\mathbf{q},\mathbf{L},\mathbf{R})\rangle_{L,R}\right\rangle_{or} = \int_0^{\pi/2}\langle F_{2\parallel}^2(qL\cos\beta)\rangle_L\langle F_{2\perp}^2(qR\sin\beta)\rangle_R h(\beta)\sin\beta d\beta \qquad (45)$$

and similarly for $\langle\langle F_2(\mathbf{q},\mathbf{L},\mathbf{R})\rangle_{L,R}^2\rangle_{or}$ with a normalized distribution function $h(\beta)$. However, it is difficult to give approximations for the distribution function $h(\beta)$.

It is much simpler to specify the orientational distribution of the cylinders $h(\delta)$ which is defined by the angle δ between a director given by the unit vector $\mathbf{D}$ and the cylinder axis $\mathbf{l}_\parallel$. For the distribution $h(\delta)$ simple approximations can be made which involve Gaussian, Onsager, Boltzmann, Maier-Saupe, Laguerre, or Heaviside-type distribution functions [13]. These functions are given by

$$h(\delta) = \begin{cases} \exp[-\sin\delta/\overline{\delta}] & , \quad \text{Onsager} \\ \exp[-\delta/\overline{\delta}] & , \quad \text{Boltzmann} \\ \exp[(\cos\delta/\overline{\delta})^2]-1 & , \quad \text{Maier}-\text{Saupe} \\ \exp[-(\delta/\overline{\delta})^2] & , \quad \text{Gaussian} \\ \sum_{k=0}^{k\max}(\delta/\overline{\delta})^{2k}\dfrac{\exp\left[-(\delta/\overline{\delta})^2\right]}{k!} & , \quad \text{Laguerre} \\ \Theta[\delta-\overline{\delta}] & , \quad \text{Heaviside} \end{cases} \qquad (46)$$

with $0 \le \overline{\delta} < \infty$. A value of 0 corresponds to a uniform orientation of all cylinders in the direction of the director, whereas a value of $\overline{\delta} \to \infty$ corresponds to an isotropic distribution. With these normalized distribution functions the mean deviation angle can be calculated as $\langle\delta\rangle = \int_0^{\pi/2}\delta h(\delta)\sin\delta d\delta$ with $0 \le \langle\delta\rangle < 1$. The functional forms are shown in Fig. 6 for the case $\overline{\delta} = \pi/8 \approx 22.5°$. In case of the Laguerre function the steepness of the distribution can be varied from Gaussian ($k_{max} = 0$) to the Heaviside step-function ($k_{max} \to \infty$).

If the distribution function is known, the orientational order parameter S defined as

$$S = \langle P_2(\mathbf{D}\mathbf{l}_\parallel)\rangle = \langle P_2(\cos\delta)\rangle = \left\langle\frac{3\cos^2\delta-1}{2}\right\rangle \qquad (47)$$

can be calculated. The values of the order parameter are $-1/2 \le S \le 1$. In this way, the order parameter can be obtained directly from the measured scattering pattern without approximations [13].

With the orientational distribution function $h(\delta)$, the orientational averages of the scattering amplitudes are then calculated as

$$\left\langle \langle F_2(\mathbf{q},\mathbf{L},\mathbf{R})\rangle_{L,R}^2\right\rangle_{or} = \int_0^{\pi/2}\langle F_{2\parallel}(qL\cos\beta(\delta))\rangle_L^2\langle F_{2\perp}(qR\sin\beta(\delta))\rangle_R^2 h(\delta)\sin\delta d\delta \qquad (48)$$

$$\left\langle \langle F_2^2(\mathbf{q},\mathbf{L},\mathbf{R})\rangle_{L,R}\right\rangle_{or} = \int_0^{\pi/2}\langle F_{d\parallel}^2(qL\cos\beta(\delta))\rangle_L\langle F_{d\perp}^2(qR\sin\beta(\delta))\rangle_R h(\delta)\sin\delta d\delta \qquad (49)$$

For cylinders, the integration over the cross-sectional amplitudes involving the hypergeometric functions (Eqs. (T5) and (T8)) is the time-limiting step in the calculations. For well-oriented systems of long cylinders, where $L \gg R$, the longitudinal part strongly suppresses the scattering intensity for all angles β except
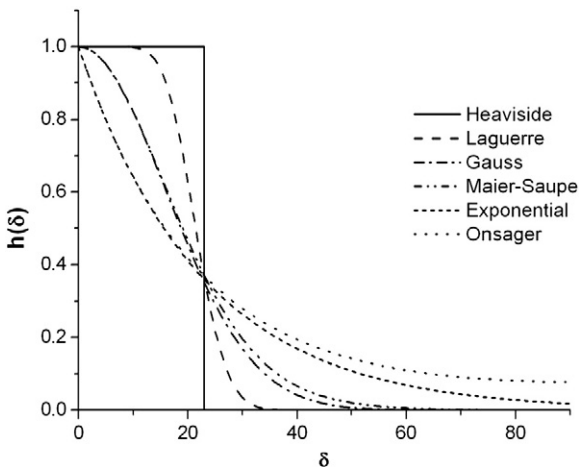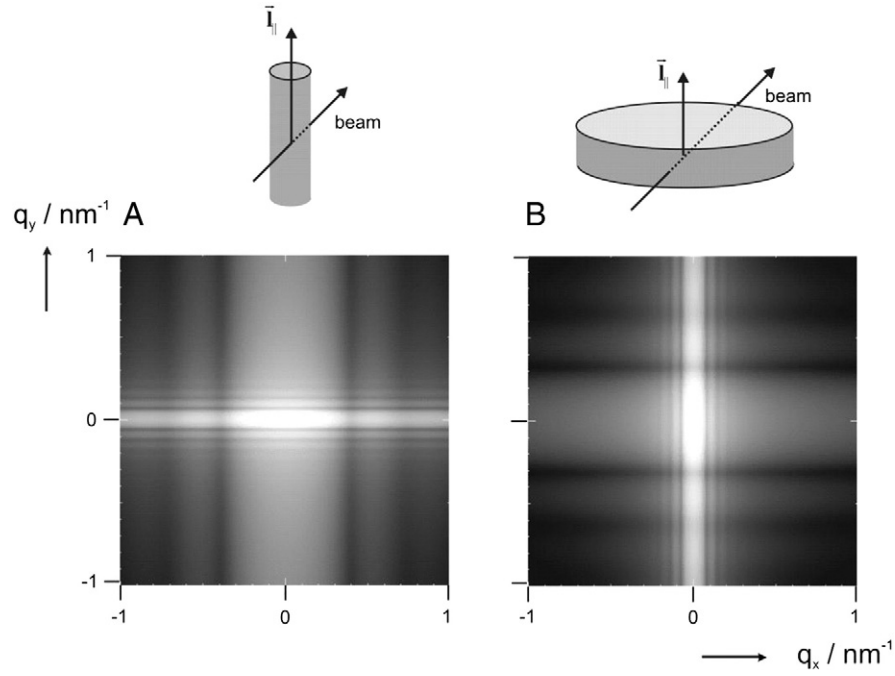
Fig. 7. Scattering patterns calculated for perfectly oriented cylinders (A) and disks (B) according to Eqs. (T3) and (T6) and Eqs. (T9) and (T12). The cylinder and disk orientation with respect to the beam direction is shown above. The cylinders have a length of $L = 100$ nm ($\sigma_L = 0.1$) and a cross-sectional radius of $R = 10$ nm ($\sigma_R = 0.1$). The disks have a thickness of $d = 20$ nm ($\sigma_d = 0.1$) and a lateral radius of $R_D = 20$ nm ($\sigma_{R_D} = 0.1$). In (A) the oscillations at low q_y parallel to the equator are related to the cylinder length and its axial form factor. The oscillations parallel to the meridian are related to the cylinder cross-section and the cross-sectional formfactor. In (B) the oscillations at low q_x parallel to the meridian are related to the the lateral disk dimension and its axial form factor. The oscillations parallel to the equator are related to the disk cross-section and its cross-sectional formfactor. Due to the polydispersity of cylinder lengths and disk radius the high-frequency oscillations are often smeared out and rarely observed in mesoscopic systems.

for $\beta \approx \pi/2$ (equator, see Fig. 7). In this case the argument of the cross-sectional amplitude $qR\sin\beta \approx qR$, so that the integrations can be approximated as

$$\left\langle \left\langle F_2(\mathbf{q}, \mathbf{L}, \mathbf{R}) \right\rangle_{L,R}^2 \right\rangle_{or} = \left\langle F_{2\perp}(q, R) \right\rangle_R^2 \int_0^{\pi/2} \left\langle F_{2\parallel}(qL\cos\beta(\delta)) \right\rangle_L^2 h(\delta)\sin\delta d\delta \tag{50}$$

$$\left\langle \left\langle F_2^2(\mathbf{q}, \mathbf{L}, \mathbf{R}) \right\rangle_{L,R} \right\rangle_{or} = \left\langle F_{2\perp}^2(q, R) \right\rangle_R \int_0^{\pi/2} \left\langle F_{d\parallel}^2(qL\cos\beta(\delta)) \right\rangle_L h(\delta)\sin\delta d\delta \tag{51}$$

which considerably saves calculation time. In case of broader orientational distributions, an approximation can be given for systems for narrow disperse cross-sectional radii $\sigma_R < 0.05$, where the averages $\langle F_{2\perp}(R, q) \rangle$ can be replaced by $F_{2\perp}(R, q)$ which saves calculation time as well.

$$\left\langle \left\langle F_2(\mathbf{q}, \mathbf{L}, \mathbf{R}) \right\rangle_{L,R}^2 \right\rangle_{or} = \int_0^{\pi/2} \left\langle F_{2\parallel}(qL\cos\beta(\delta)) \right\rangle_L^2 F_{2\perp}^2(qR\sin\beta(\delta)) h(\delta)\sin\delta d\delta \tag{52}$$

$$\left\langle \left\langle F_2^2(\mathbf{q}, \mathbf{L}, \mathbf{R}) \right\rangle_{L,R} \right\rangle_{or} = \int_0^{\pi/2} \left\langle F_{d\parallel}^2(qL\cos\beta(\delta)) \right\rangle_L F_{d\perp}^2(qR\sin\beta(\delta)) h(\delta)\sin\delta d\delta \tag{53}$$

However, for larger polydispersities this approximation does not reproduce the damping of the cross-sectional form factor oscillations, a feature that commonly has to be taken into account. Therefore Eqs. (52) and (53) are not used for calculations involving cylinders in

the remaining manuscript. However, for disks this approximation is very useful.

To perform the integration one needs the relation $\beta(\delta)$ between the angles β and δ. We assume that the director $\mathbf{D}$ is a unit vector defined by the angles θ and φ in the polar coordinate system in Fig. 8. In this coordinate system the beam direction $\mathbf{n}$ is parallel to the negative z-direction. To perform the integrations in Eqs. (50) and (51) we need all cylinder unit vectors $\mathbf{l}$ that have a deviation angle δ with respect to the director. These unit vectors are located on a cone around the director axis $\mathbf{D}$ as shown in Fig. 8. They can be obtained from a unit vector $\mathbf{l}_0(\delta)$ by rotation through an angle
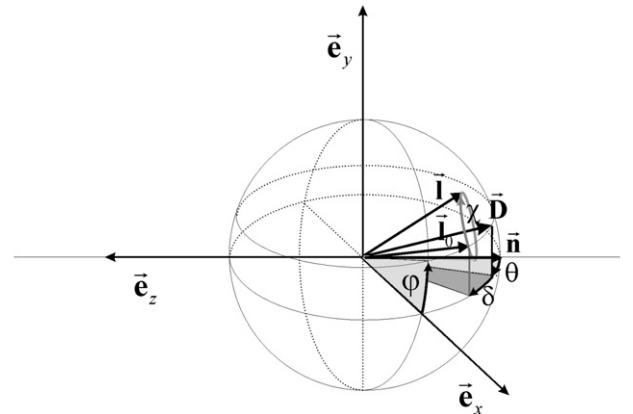
Fig. 8. Scheme of the coordinate system and rotation angles used for calculation of the orientational averages. The orientation of the director $\mathbf{D}$ is specified by the polar angles θ and φ with respect to the direction of the beam $\mathbf{n}$. All cylinders unit vectors $\mathbf{l}$ with a deviation angle δ are located on a cone around $\mathbf{D}$ with an opening angle δ. These vectors are generated from a unit vector $\mathbf{l}_0$ with the same polar angle φ as the director $\mathbf{D}$, but with a larger angle $\theta + \delta$, by rotation with an angle $0 \leq \chi < 2\pi$ around the cone.

$0 \leq \chi < 2\pi$ around **D**. With the director **D** and the cylinder unit vector $\mathbf{l}_0(\delta)$ given by

$$\mathbf{D} = \begin{pmatrix} \sin(\theta)\cos(\varphi) \\ \cos(\theta) \\ -\sin(\theta)\sin(\varphi) \end{pmatrix}, \quad \mathbf{l}_0 = \begin{pmatrix} \sin(\theta-\delta)\cos(\varphi) \\ \cos(\theta-\delta) \\ -\sin(\theta-\delta)\sin(\varphi) \end{pmatrix} \qquad (54)$$

the unit vectors $\mathbf{l}(\delta, \chi)$ can be calculated as $\mathbf{l}(\delta, \chi) = \mathbf{M}(\chi)\mathbf{l}_0(\delta)$, where $\mathbf{M}(\chi)$ is the rotation matrix given by [7]

$$\mathbf{M}(\chi) = \begin{pmatrix} c\chi + (1-c\chi)s^2\theta c^2\varphi & -s\theta s\varphi s\chi + (1-c\chi)c\theta s\theta s\varphi & -c\theta s\chi - (1-c\chi)s^2\theta c\varphi s\varphi \\ s\theta s\varphi s\chi + (1-c\chi)c\theta s\theta c\varphi & c\chi + (1-c\chi)c^2\theta & s\theta c\varphi s\chi - (1-c\chi)c\theta s\theta s\varphi \\ c\theta s\chi - (1-c\chi)s^2\theta c\varphi s\varphi & -s\theta c\varphi s\chi - (1-c\chi)c\theta s\theta s\varphi & c\chi - (1-c\chi)s^2\theta s^2\varphi \end{pmatrix} \qquad (55)$$

where $c(z) = \cos(z)$ and $s(z) = \sin(z)$ and $0 \leq \varphi < 2\pi$ and $0 \leq \theta < \pi$. The angle β between the cylinder axis vector $\mathbf{l}(\delta, \chi)$ and the scattering vector $\mathbf{q}$ is then given by $\beta(\delta, \chi) = \arccos[\mathbf{l}(\delta, \chi)\mathbf{q}]$. The integration of functions $f[\beta(\delta, \chi)]$ as in Eqs. (50) and (51) is then performed as

$$\langle f \rangle = \frac{\int\limits_0^{\pi/2}\int\limits_0^{2\pi} f[\beta(\delta, \chi)]h(\delta)\sin\delta d\chi d\delta}{\int\limits_0^{\pi/2}\int\limits_0^{2\pi} h(\delta)\sin\delta d\chi d\delta} \qquad (56)$$

to obtain the orientationally averaged scattering amplitudes $\left\langle \left\langle F_2(\mathbf{q}, \mathbf{L}, \mathbf{R}) \right\rangle_{L,R}^2 \right\rangle_{or}$ and $\left\langle \left\langle F_2^2(\mathbf{q}, \mathbf{L}, \mathbf{R}) \right\rangle_{L,R} \right\rangle_{or}$.

The calculation of the scattering amplitudes as well as of the mean angle $\langle \delta \rangle_{or}$ and the orientational order parameter $S = \frac{1}{2}\langle(3\cos^2\delta - 1)\rangle_{or}$ for a given distribution function is done numerically. Solutions in terms of higher transcendental functions can be given in some cases, but are generally not useful for numerical calculations.

In the limiting case of perfect orientation where $\langle \delta \rangle_{or} = 0$ and $S = 1$, Eqs. (T3) and (T6) are used for cylinders. In the limiting case of isotropic orientation where $\langle \delta \rangle_{or} = 54.7$ and $S = 0$, assuming monodisperse cylinders, we obtain

$$\left\langle \left\langle F_2(\mathbf{q}, \mathbf{L}, \mathbf{R}) \right\rangle_{L,R}^2 \right\rangle_{or} = \left\langle F_{2\perp}(q, R) \right\rangle_R^2 \int\limits_0^{\pi/2} F_{2\parallel}^2(qL\cos\beta)\sin\beta d\beta \qquad (57)$$

$$\left\langle \left\langle F_2^2(\mathbf{q}, \mathbf{L}, \mathbf{R}) \right\rangle_{L,R} \right\rangle_{or} = \left\langle F_{2\perp}^2(q, R) \right\rangle_R \int\limits_0^{\pi/2} F_{2\parallel}^2(qL\cos\beta)\sin\beta d\beta \qquad (58)$$

The integration can be done analytically yielding

$$\left\langle \left\langle F_2(q, L, R) \right\rangle_{L,R}^2 \right\rangle_{iso} = F_{2\parallel}^2(qL)_{iso}\left\langle F_{2\perp}(q, R) \right\rangle_R^2 \qquad (59)$$

$$\left\langle \left\langle F_2^2(q, L, R) \right\rangle_{L,R} \right\rangle_{iso} = F_{2\parallel}^2(qL)_{iso}\left\langle F_{2\perp}^2(q, R) \right\rangle_R \qquad (60)$$

with

$$F_{2\parallel}^2(qL)_{iso} = \frac{2}{qL}Si(qL) - \left(\frac{\sin(qL/2)}{qL/2}\right)^2 \qquad (61)$$

where the subscript *iso* denotes isotropic distribution. $Si(z)$ is the sine-integral for which excellent numerical approximations are available (see Appendix, Section A.3).

For disks, the averages over the orientational distribution is obtained by averaging the scattering amplitudes $\langle F_1(\mathbf{q}, \mathbf{R}_D, \mathbf{R}) \rangle_{R_D,R}$ and $\langle F_1^2(\mathbf{q}, \mathbf{R}_D, \mathbf{R}) \rangle_{R_D,R}$ over a distribution of angles β between the lateral disk direction, $\mathbf{l}_\parallel$, and the scattering vector $\mathbf{q}$. The scalar products are

$\mathbf{q}\mathbf{R} = Rq\mathbf{l}_\perp = qR\cos\beta$ and $\mathbf{q}\mathbf{R}_D = R_D q\mathbf{l}_\parallel = qR_D\sin\beta$. The orientational average is then calculated as

$$\left\langle \left\langle F_1(\mathbf{q}, \mathbf{L}, \mathbf{R}) \right\rangle_{R_D,R}^2 \right\rangle_{or} = \int\limits_0^{\pi/2} \left\langle F_{1\parallel}(qR_D\sin\beta(\delta)) \right\rangle_{R_D}^2 \left\langle F_{1\perp}(qR\cos\beta(\delta)) \right\rangle_R^2 h(\delta)\sin\delta d\delta \qquad (62)$$

$$\left\langle \left\langle F_1^2(\mathbf{q}, \mathbf{L}, \mathbf{R}) \right\rangle_{R_D,R} \right\rangle_{or} = \int\limits_0^{\pi/2} \left\langle F_{1\parallel}^2(qR_D\sin\beta(\delta)) \right\rangle_{R_D} \left\langle F_{1\perp}^2(qR\cos\beta(\delta)) \right\rangle_R h(\delta)\sin\delta d\delta \qquad (63)$$

For well-oriented thin disks, where $R_D \gg R$, the parallel part F_1 strongly suppresses the scattering intensity for all angles β except for $\beta \approx 0$ (meridian, see Fig. 7). In this case the argument of the cross-sectional amplitude $F_\perp$ $qR\cos\beta \approx qR$, so that a similar approximation could be made as in the case of cylinders. However, then the integration would still involve the hypergeometric functions which is prohibitive for reasonable calculation times. One could approximate it by the monodisperse case, as it was discussed for the cylinders, where it involves integration over the Bessel function. This leads to undamped oscillations on the equator at very low values $\mathbf{q}$, which would not be relevant in many cases.

$$\left\langle \left\langle F_1(\mathbf{q}, \mathbf{L}, \mathbf{R}) \right\rangle_{R_D,R}^2 \right\rangle_{or} = \int\limits_0^{\pi/2} F_{1\parallel}^2(qR_D\sin\beta(\delta))\left\langle F_{1\perp}(qR\cos\beta(\delta)) \right\rangle_R^2 h(\delta)\sin\delta d\delta \qquad (64)$$

$$\left\langle \left\langle F_1^2(\mathbf{q}, \mathbf{L}, \mathbf{R}) \right\rangle_{R_D,R} \right\rangle_{or} = \int\limits_0^{\pi/2} F_{1\parallel}^2(qR_D\sin\beta(\delta))\left\langle F_{1\perp}^2(qR\cos\beta(\delta)) \right\rangle_R h(\delta)\sin\delta d\delta \qquad (65)$$

Here, a useful approximation to the Bessel function which has the correct asymptotic limits, but no oscillations is given by

$$F_{1\parallel}^2(x) = \left(1 + \frac{\pi}{4}x^3\right)^{-1} \qquad (66)$$

For the limits $x \to 0$ and $x \to \infty$ it has the same first terms of the series and asymptotic expansions as the exact expression, and well describes the non-oscillating part over the entire range of x, as outlined in Section A.2 of the Appendix. In the limiting case of perfect orientation where $\langle \delta \rangle_{or} = 0$ and $S = 1$, Eqs. (T9) and (T12) are used for the scattering amplitudes for the disks. Similarly, for disks in the isotropic case we use the equations

$$\left\langle \left\langle F_1(q, R_D, R) \right\rangle_{L,R}^2 \right\rangle_{iso} = F_{1\parallel}^2(qR_D)_{iso}\left\langle F_{1\perp}(q, R) \right\rangle_R^2 \qquad (67)$$

$$\left\langle \left\langle F_1^2(q, R_D, R) \right\rangle_{L,R} \right\rangle_{iso} = F_{1\parallel}^2(qR_D)_{iso}\left\langle F_{1\perp}^2(q, R) \right\rangle_R \qquad (68)$$

with

$$F_{1\parallel}^2(qR_D)_{iso} = \frac{2}{(qR_D)^2}\left(1 - \frac{J_1[2qR_D]}{qR_D}\right) \qquad (69)$$

For all following calculations we use Eqs. (50) and (51) for partially oriented cylinders, Eqs. (T3) and (T6) for perfectly oriented cylinders, and Eqs. (59) and (60) for isotropic cylinders. For partially oriented disks we use Eqs. (64) and (65) with the asymptote Eq. (66), for perfectly oriented disks Eqs. (T9) and (T12), and for isotropic disks we use Eqs. (67) and (68). All scattering amplitudes that are relevant for the forthcoming calculations are summarized in Tables 2 and 3.

For an order parameter of $S = 0.70$ the intensity distribution for different distribution functions are shown in Fig. 9. There is a pronounced increase of the azimuthal intensity at the corresponding

Table 3
Compilation of the main functions and equations that are used for the calculation of the scattering patterns. Starting point is the expression for the scattering intensity $I(\mathbf{q})$ in Eq. (25) contained in the first column, which depends on the functions in the subsequent columns. The last column lists the parameters that need to be specified for calculations.

$I(\mathbf{q})$ (25)			$\mathbf{q}$	(3)	q_x, q_y, q_z
$\langle P(q,L,R)\rangle_{iso}$ (24, isotropic)			$\langle F_2^2(q,R)\rangle_R$	Spheres (T2)	R, σ_R
			$\langle F^2(q,R,d)\rangle_{R,d}$	Vesicles (T16)	R, σ_R, d, σ_d
			$\langle F_2^2(q,L,R)\rangle_R$	Cylinders (60,61,T8)	L, R, σ_R
			$\langle F_1^2(q,R_D,R)\rangle_R$	Disks (67,68,T14)	R_D, R, σ_R
$\langle P(\mathbf{q},\mathbf{L},\mathbf{R})\rangle_{or}$ (24, oriented)	$\langle\langle F_2^2(\mathbf{q},\mathbf{L},\mathbf{R})\rangle_{L,R}\rangle_{or}$ (56; 51)		$\langle F_2^2(\mathbf{q},\mathbf{L},\mathbf{R})\rangle_{L,R}$	Cylinders (T6,T7,T8)	$L, \sigma_L, R, \sigma_R, \overline{\delta}$
	$\langle\langle F_1^2(\mathbf{q},\mathbf{R}_D,\mathbf{R})\rangle_{R_D,d}\rangle_{or}$ (56; 65,66)		$\langle F_1^2(\mathbf{q},\mathbf{R}_D,\mathbf{R})\rangle_{R_D,R}$	Disks (T12,T13,T14)	$R_D, \sigma_{R_D}, R, \sigma_R, \overline{\delta}$
			$h(\delta)$	Distr. Funct. (46)	choice of type
$\beta(q,L,R)$ (23, isotropic)			$\langle F_3(q,R)\rangle_R$	Spheres (T1)	R, σ_R
			$\langle F(q,R,d)\rangle_{R,d}$	Vesicles (T15)	R, σ_R, d, σ_d
			$\langle F_2(q,L,R)\rangle_{L,R}$	Cylinders (59,61,T5)	L, R, σ_R
			$\langle F_1(q,R_D,R)\rangle_{R_D,R}$	Disks (67,69,T11)	R_D, R, σ_R
$\beta(\mathbf{q},\mathbf{L},\mathbf{R})$ (23, oriented)	$\langle\langle F_2(\mathbf{q},\mathbf{L},\mathbf{R})\rangle_{L,R}^2\rangle_{or}$ (56; 50)		$\langle F_2(\mathbf{q},\mathbf{L},\mathbf{R})\rangle_{L,R}$	Cylinders (T4,T5)	$L, \sigma_L, R, \sigma_R, \overline{\delta}$
	$\langle\langle F_1(\mathbf{q},\mathbf{R}_D,\mathbf{R})\rangle_{R_D,R}^2\rangle_{or}$ (56; 64,66)		$\langle F_1(\mathbf{q},\mathbf{R}_D,\mathbf{R})\rangle_{R_D,R}$	Disks (T10,T11)	$R_D, \sigma_{R_D}, R, \sigma_R, \overline{\delta}$
$\langle Z(\mathbf{q},\mathbf{g}_{hkl})\rangle_{or}$ (77)				Lattice (Table 5)	choice of type
			f_{hkl}	Table 4	
		$L_{hkl}(\mathbf{q},\mathbf{g}_{hkl})$		Gaussian (79)	$\sigma_x, \sigma_y, \sigma_z$
		(80)	$L_q(\mathbf{q},\mathbf{g}_{hkl})$	Rad. Peak (82)	δ_q
			$L_\psi(\mathbf{q},\mathbf{g}_{hkl})$	Azim. Peak (90)	δ_ψ
		$\mathbf{g}_{hkl}$	$\mathbf{a}^*, \mathbf{b}^*, \mathbf{c}^*$	Lattice (Fig. 10) (74,75)	a, b, c
				Orientation (8–12, 16)	ψ, θ, φ or $\mathbf{n}, \mathbf{u}$
$G(q,g_{hkl})$(73)				displacement	σ_a

average angle $\langle\delta\rangle = 26.6°$, which is indicated in Fig. 9A. This intensity increase is nearly step-like for the Heaviside function and broad for the Onsager-function.

3.7. Lattice factor

After consideration of the formfactors taking into account size distributions and orientational distributions, we now have to consider the structure factor $Z(\mathbf{q}, \mathbf{g})$. Using the Miller indices (hkl) for a given crystal lattice plane, the lattice factor for an ideal undistorted lattice can be written as [3,8,9]

$$Z(\mathbf{q},\mathbf{g}) = \frac{(2\pi)^3}{nv_d} \sum_{\substack{h,k,l=-\infty \\ (hkl)\neq(000)}}^{\infty} f_{hkl}^2 L_{hkl}(\mathbf{q},\mathbf{g}_{hkl}) \qquad (70)$$

where n is the number of particles per unit cell, f_{hkl} is the structure factor of the unit cell, v_d is the volume ($d = 3$), surface ($d = 2$), or long-period ($d = 1$) of the d-dimensional unit cell, and $L_{hkl}(\mathbf{q}, \mathbf{g}_{hkl})$ is a normalized peak shape function that depends on the reciprocal lattice vectors $\mathbf{g}_{hkl}$.

The summation is over all values of the Miller indices hkl except for $(hkl) = (000)$. The omission of the contribution $Z(\mathbf{q} = 0)$ ensures that the Porod invariant Q is given by

$$(2\pi)^{-3}V\int I(\mathbf{q})d\mathbf{q} = Q = \phi_1(1-\phi_1) \qquad (71)$$

by causing the term $-\phi_1^2$, it imparts consistency with Porod's law (Eq. (36)), and ensures that the limit $q\to 0$ is given by the density fluctuations
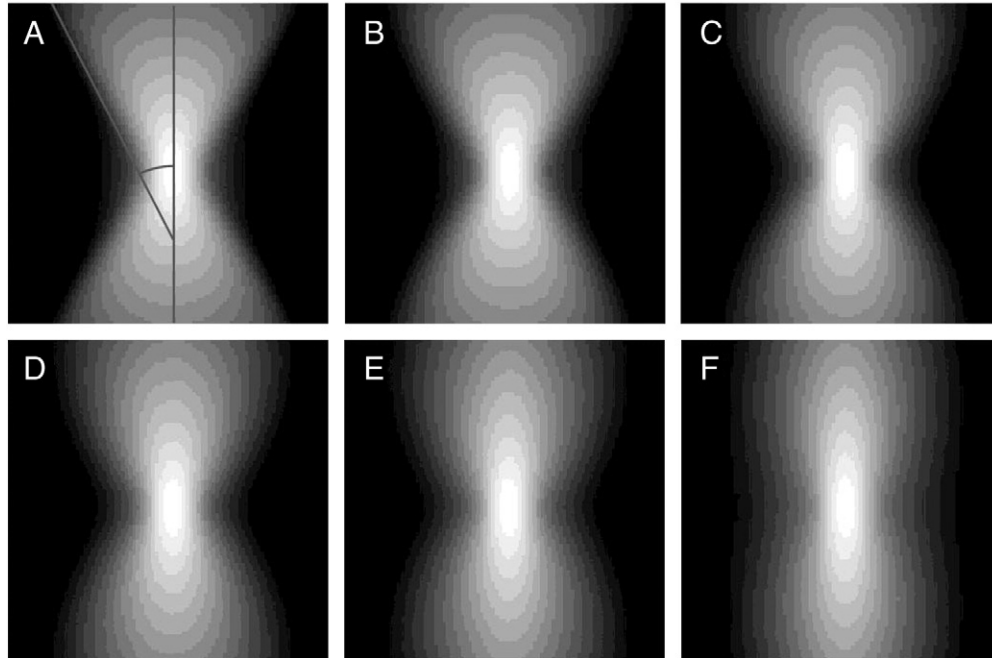

Fig. 9. Calculated scattering patterns for cylinders with length $L = 300$ nm ($\sigma_L = 0.3$) and cross-sectional radius $R = 8.0$ nm ($\sigma_R = 0.13$) with an orientational distribution characterized by a mean deviation angle of $\langle\delta\rangle = 26.56$. As orientational distribution functions the (A) Heaviside ($\overline{\delta} = 38.3$)), (B) Laguerre ($\overline{\delta} = 14.6$), (C) Gauss ($\overline{\delta} = 28.2$), (D) Meier-Saupe ($\overline{\delta} = 24.9$), (E) Exponential ($\overline{\delta} = 12.6$), and (F) Onsager-function ($\overline{\delta} = 9.8$) were used. The angle shown in (A) corresponds to $\langle\delta\rangle = 26.56$.

Table 4
Summary of lattice types that are considered in the calculation of scattering patterns together with the direct space bases vectors (**a**, **b**, **c**), the reciprocal space base vectors (**a***, **b***, **c***), the structure factors f_{hkl}, the volume V, base area A, or linear dimension L of the unit cells, the volume fractions ϕ, and the number of particles per unit cell n. For FCC, BCC and HCP also the reciprocal space base vectors of the twinned structures are given. In case of the cubic bicontinuous structures Ia3d, Im3m, and Pn3m only the indices of the first allowed reflections are given.

Bravais lattice	Primitive vectors			Unit cell volume V	Basic vectors		
	a	**b**	**c**		**a***	**b***	**c***
SC (Pm3m)	$a\mathbf{e}_x$	$a\mathbf{e}_y$	$a\mathbf{e}_z$	$V=a^3$	$\frac{2\pi}{a}\mathbf{e}_x$	$\frac{2\pi}{a}\mathbf{e}_y$	$\frac{2\pi}{a}\mathbf{e}_z$
	$f_{hkl}=1$					$\phi=\frac{4\pi}{3}\frac{R^3}{a^3}$	$n=1$
BCC (Im3m)	$a\mathbf{e}_x$	$a\mathbf{e}_y$	$a\mathbf{e}_z$	$V=a^3$	$\frac{2\pi}{a}\mathbf{e}_x$	$\frac{2\pi}{a}\mathbf{e}_y$	$\frac{2\pi}{a}\mathbf{e}_z$
Twin					$\frac{2\pi}{3a}(2\mathbf{e}_x+\mathbf{e}_y-2\mathbf{e}_z)$	$\frac{2\pi}{3a}(\mathbf{e}_x+2\mathbf{e}_y+2\mathbf{e}_z)$	$\frac{2\pi}{3a}(2\mathbf{e}_x-2\mathbf{e}_y+\mathbf{e}_z)$
	$f_{hkl}=1+\cos[\pi(h+k+l)]$					$\phi=\frac{8\pi}{3}\frac{R^3}{a^3}$	$n=2$
FCC (Im3m)	$a\mathbf{e}_x$	$a\mathbf{e}_y$	$a\mathbf{e}_z$	$V=a^3$	$\frac{2\pi}{a}\mathbf{e}_x$	$\frac{2\pi}{a}\mathbf{e}_y$	$\frac{2\pi}{a}\mathbf{e}_z$
Twin					$\frac{2\pi}{3a}(2\mathbf{e}_x-\mathbf{e}_y+2\mathbf{e}_z)$	$\frac{2\pi}{3a}(2\mathbf{e}_x+2\mathbf{e}_y-\mathbf{e}_z)$	$\frac{2\pi}{3a}(-\mathbf{e}_x+2\mathbf{e}_y+2\mathbf{e}_z)$
	$f_{hkl}=1+\cos[\pi(h+k)]+\cos[\pi(h+l)]+\cos[\pi(k+l)]$					$\phi=\frac{16\pi}{3}\frac{R^3}{a^3}$	$n=4$
BCT (I4/mmm)	$a\mathbf{e}_x$	$a\mathbf{e}_y$	$c\mathbf{e}_z$	$V=a^2c$	$\frac{2\pi}{a}\mathbf{e}_x$	$\frac{2\pi}{a}\mathbf{e}_y$	$\frac{2\pi}{c}\mathbf{e}_z$
	$f_{hkl}=1+\cos[\pi(h+k+l)]$					$\phi=\frac{8\pi}{3}\frac{R^3}{a^2c}$	$n=2$
HCP (P6/mmc)	$a\mathbf{e}_x$	$\frac{1}{2}a\mathbf{e}_x+\frac{\sqrt{3}}{2}a\mathbf{e}_y$	$\sqrt{\frac{8}{3}}a\mathbf{e}_z$	$V=\sqrt{2}a^3$	$\frac{2\pi}{a}\left(\mathbf{e}_x-\frac{1}{\sqrt{3}}\mathbf{e}_y\right)$	$\frac{4\pi}{\sqrt{3}a}\mathbf{e}_y$	$\sqrt{\frac{3}{8}}\frac{2\pi}{a}\mathbf{e}_z$
Twin					$-\frac{2\pi}{a}\mathbf{e}_x$	$\frac{2\pi}{\sqrt{3}a}(\mathbf{e}_x+2\mathbf{e}_y)$	$\sqrt{\frac{3}{8}}\frac{2\pi}{a}\mathbf{e}_z$
	$f_{hkl}=2\cos[2\pi(\frac{h+2k}{3}+\frac{l}{4})]$					$\phi=\frac{8\pi}{3\sqrt{2}}\frac{R^3}{a^3}$	$n=2$
HEX (P/6 mm)	$a\mathbf{e}_x$	$\frac{1}{2}a\mathbf{e}_x+\frac{\sqrt{3}}{2}a\mathbf{e}_y$		$A=\frac{\sqrt{3}}{2}a^2$	$\frac{2\pi}{a}\left(\mathbf{e}_x-\frac{1}{\sqrt{3}}\mathbf{e}_y\right)$	$\frac{4\pi}{\sqrt{3}a}\mathbf{e}_y$	
	$f_{hkl}=1$					$\phi=\frac{2\pi}{\sqrt{3}}\frac{R^2}{a^2}$	$n=1$
CREC (cmm)	$a\mathbf{e}_x$	$b\mathbf{e}_y$		$A=ab$	$\frac{2\pi}{a}\mathbf{e}_x$	$\frac{2\pi}{b}\mathbf{e}_y$	
	$f_{hkl}=1$					$\phi=2\pi\frac{R^2}{ab}$	$n=2$
SQ (P/4 mm)	$a\mathbf{e}_x$	$a\mathbf{e}_y$		$A=a^2$	$\frac{2\pi}{a}\mathbf{e}_x$	$\frac{2\pi}{a}\mathbf{e}_y$	
	$f_{hkl}=1$					$\phi=\pi\frac{R^2}{a^2}$	$n=1$
LAM	$\mathbf{a}=a\mathbf{e}_x$			$L=a$	$\frac{2\pi}{a}\mathbf{e}_x$		
	$f_{hkl}=1$					$\phi=\frac{2R}{a}$	$n=1$
Ia3d	211,220,321,332,400,420,422,431,440,444,521,532,541,543,552						
Im3m	110,200,211,220,222,310,321,330,332,400,411,420,422,431,433						
Pn3m	110,111,200,211,220,221,222,310,311,321,322,330,331,332,333						

$$\lim_{q\to 0} I(q) = \frac{\left\langle N^2\right\rangle-\langle N\rangle^2}{V} \tag{72}$$

The values for n, v_d and expressions for the structure factors f_{hkl} for different crystal lattices (*lam, sq, hex, sc, bcc, fcc, hcp, bct, Ia3d, Pn3m,* and *Im3m*) are given in Table 4. The crystal structures are depicted in Fig. 10.

For lattices with translational disorder where the displacements from the ideal lattice points are statistically independent (static disorder of the first kind), one can assume a Gaussian lattice point distribution with zero mean and a relative mean square displacement σ_α^2. In this case $G(q)$ is given by

$$G(q) = \exp\left[-\sigma_a^2\overline{a}^2 q^2\right] \tag{73}$$

which is known as the Debye–Waller factor for thermal disorder. $\overline{\alpha}$ is the next nearest neighbour distance between adjacent particles, which for SC and HCP is $\overline{a}=a$, for BCC $\overline{a}=\frac{\sqrt{3}}{2}a$, and for FCC $\overline{a}=\frac{\sqrt{2}}{2}a$.

3.7.1. Direct and reciprocal lattice vectors

For any lattice with a set of primitive vectors (**a**, **b**, and **c**) given in terms of the coordinate system spanned by the unit vectors ($\hat{\mathbf{e}}_x$, $\hat{\mathbf{e}}_y$, $\hat{\mathbf{e}}_z$) the basic vectors of the reciprocal lattice are given by [7]

$$\boldsymbol{\alpha}^* = \frac{1}{V}(\mathbf{b}\times\mathbf{c}) = \frac{1}{V}\begin{vmatrix} \hat{\mathbf{e}}_x & \hat{\mathbf{e}}_y & \hat{\mathbf{e}}_z \\ b_x & b_y & b_z \\ c_x & c_y & c_z \end{vmatrix}$$

$$\mathbf{b}^* = \frac{1}{V}(\mathbf{c}\times\mathbf{a}) = \frac{1}{V}\begin{vmatrix} \hat{\mathbf{e}}_x & \hat{\mathbf{e}}_y & \hat{\mathbf{e}}_z \\ c_x & c_y & c_z \\ a_x & a_y & a_z \end{vmatrix} \tag{74}$$

$$\mathbf{c}^* = \frac{1}{V}(\mathbf{a}\times\mathbf{b}) = \frac{1}{V}\begin{vmatrix} \hat{\mathbf{e}}_x & \hat{\mathbf{e}}_y & \hat{\mathbf{e}}_z \\ a_x & a_y & a_z \\ b_x & b_y & b_z \end{vmatrix}$$

where V is the volume of the unit cell of the direct lattice. In case of two-dimensional lattices, $\mathbf{c}=\hat{\mathbf{e}}_z$, in case of a one-dimensional lattice there is $\mathbf{b}=\hat{\mathbf{e}}_y$ and $\mathbf{c}=\hat{\mathbf{e}}_z$. The reciprocal lattice vectors are given by

$$\begin{aligned} \text{3D−lattice: } \mathbf{g}_{hkl} &= h\mathbf{a}^* + k\mathbf{b}^* + l\mathbf{c}^* \\ \text{2D−lattice: } \mathbf{g}_{hk} &= h\mathbf{a}^* + k\mathbf{b}^* \\ \text{1D−lattice: } \mathbf{g}_h &= h\mathbf{a}^* \end{aligned} \tag{75}$$

for three-dimensional, for two-dimensional, and for one-dimensional systems. For the lattices considered in the following the basis vectors in real space and reciprocal space are given in Table 4. Also given are the basis vectors for the twinned structures in case of fcc, bcc, and hcp-lattice as they frequently are observed in soft materials with cubic symmetry.
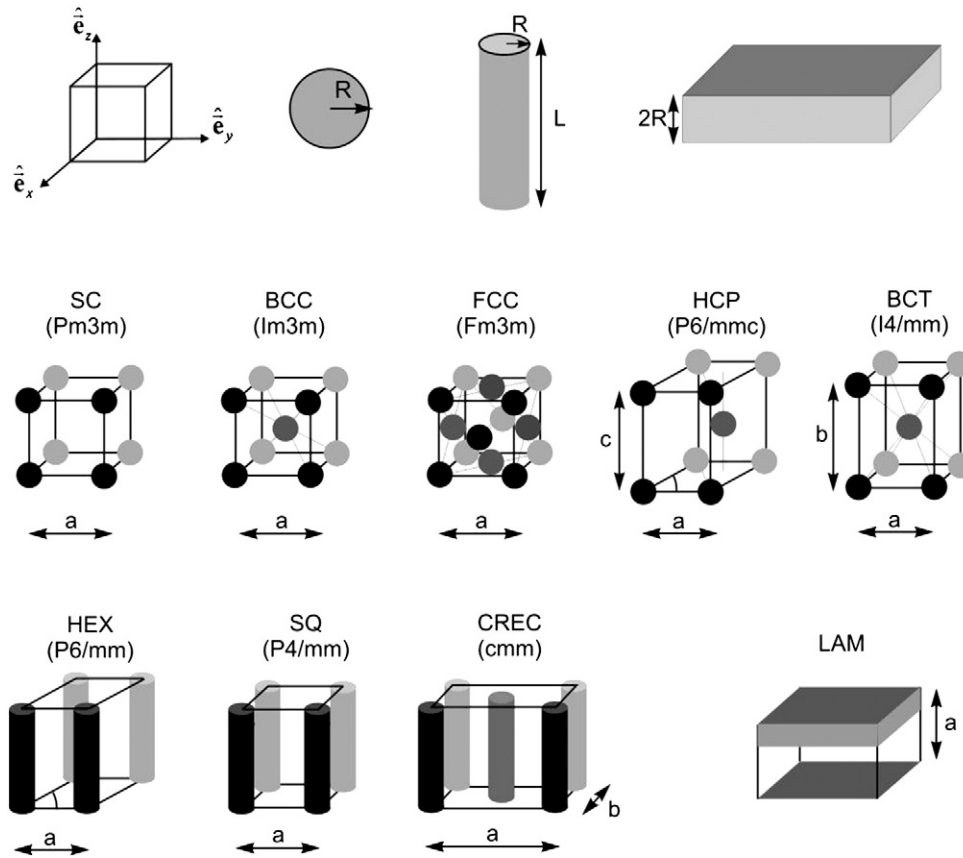
Fig. 10. Scheme of the lattice-types that are considered for the calculation of scattering patterns. The lattices consist of spheres, cylinders and lamellae as building blocks. Detailed structural parameters of the lattices are given in Table 4.

3.7.2. Approximation for bicontinuous ordered structures (Ia3d, Pn3m, and Im3m)

Analytical expressions for the structure factors of the frequently occurring ordered bicontinuous phases that include the G-surface ("gyroid", Ia3d) the D-surface ("double diamond", Pn3m) and the P-surface ("plumbers nightmare", Im3m) are numerically very time-consuming to evaluate. They can be obtained by numerically taking the 3D Fourier transform of level set models of the corresponding surfaces [14]. Within the concept of the decoupling approximation we consider a very simple approximation that involves the separation of the scattered intensity into a contribution of the structure factor and the form factor. For the structure factor we choose the set of allowed reflections as given for each space group in Table 4. For the calculation of the formfactor we approximate the topology of the bicontinous bilayer structure by closed spherical bilayers (vesicles) that are located at the 8 corners

Fig. 11. Approximation of the structure of bicontinuous cubic phases by using vesicles such that the bilayer volume fraction is equal to the bicontinuous volume fraction. The vesicles are characterized by the outer radius R_o and inner radius R_i of the vesicle bilayer. (A) is used for primitive cubic structures, and (B) for body-centered cubic structures.

of the unit cell in case of primitive lattices (Pn3m) and additionally in the center in case of the body-centered lattices (Ia3d and Im3m). This is schematically shown in Fig. 11. To maintain consistency with the actual bilayer structure we require the volume fraction ϕ of the vesicle walls, i.e. the hydrophobic volume, to be identical to the corresponding volume fraction of the bicontinuous phase. The remaining integral structural parameters, i.e. specific surface area, the mean curvature, and the Gaussian curvature, are overestimated with this model. However, their effect on the scattering curve becomes significant only at higher q-values (Porod-regime), so that at lower q-values the approximation describes experimentally measured scattering curves reasonably well, as will be shown below.

As schematically shown in Fig. 11, we assume a close-packing of vesicles within the unit cell, which requires the outer radius R_o of the vesicles to be equal to half of nearest neighbour distance, $R_o = \bar{a}/2$. The inner radius R_i is then determined by the volume fraction ϕ. The volume occupied by the bilayer of a vesicle is given by $V_{ves} = \frac{4\pi}{3}(R_o^3 - R_i^3)$. The volume fraction of the bilayers in the unit cell is then $\phi_{ves} = \frac{nV_{ves}}{a^3}$, where n is the number of vesicles per unit cell (SC: $n = 1$, BCC: $n = 2$) and a is the unit cell dimension. For cubic lattices there is a simple relation between the unit cell dimension and the nearest neighbour distance, which can be expressed as $\bar{a} = ca$ (SC: $c = 1$, BCC: $c = \sqrt{3}/2$). For a given volume fraction the inner radius of the vesicle can then be calculated to be
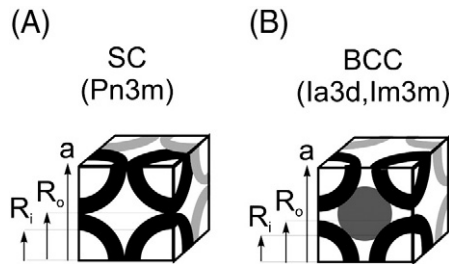
$$R_i = \frac{a}{2}\left(c^3 - \frac{6\phi}{n\pi}\right)^{1/3} \tag{76}$$

which allows to calculate the form factor $\langle R(\mathbf{q}, R, d)\rangle$ using Eqs. (T15) and (T16).

3.8. Anisotropic peak shape functions

To take into account the orientational distribution of the unit cells, the effect of the orientational distribution on the peak shape function has to be considered as

$$\langle Z(\mathbf{q},\mathbf{g})\rangle_{or} = \frac{(2\pi)^3}{nv_d} \sum_{\substack{h,k,l=-\infty \\ (hkl)\neq(000)}}^{\infty} f_{hkl}^2 \langle L_{hkl}(\mathbf{q},\mathbf{g}_{hkl})\rangle_{or} \tag{77}$$

This could be evaluated analogous to Eq. (45)

$$\langle L_{hkl}(\mathbf{q},\mathbf{g}_{hkl})\rangle_{or} = \int_0^{\pi/2} L_{hkl}(q,g_{hkl},\beta)h(\beta)\sin\beta d\beta \tag{78}$$

where β is the angle between the lattice vector and the scattering vector. Since, however, the integration has to be done for all reflections h, k, and l, the calculation time would be prohibitively long. The lattice factor involves a set of Bragg-peaks at certain values and positions of the scattering vector $\mathbf{q}$. An orientational distribution affects the peak widths in different directions in reciprocal space. However, as discussed above, for the lattice factor there are additional effects such as finite domain sizes, lattice defects and other structural features such as strain that limit coherent interference over long distances and affect the peak width. Also the limited primary beam coherence leads to a broadening and smearing of Bragg-peaks in different directions.

We therefore take a different, more pragmatic route and assume, that the Bragg-peaks have certain anisotropic shapes, that can be described in a closed analytical form. If the orientational distribution is the cause of anisotropic peak broadening, then by using the concept of coherence lengths the mean deviation angle and the orientational order parameter can be calculated and compared to the values derived from the orientational distribution functions used for the scattering amplitudes.

Anisotropic peak shapes such as anisotropic Gaussians, Lorentzians or other functions are frequently used to analyze Bragg-peaks of ordered structures. Since in our case we provide quantitative expressions, we need to properly normalize the anisotropic peak shape functions, which is described in the following Sections.

3.8.1. Anisotropic Gaussian

A simple case is to consider an anisotropic Gaussian peak shape function which depends on the scattering vector $\mathbf{q}=(q_x,q_y,q_z)$ and the reciprocal lattice vector $\mathbf{g}_{hkl}=(g_{x,hkl},g_{y,hkl},g_{z,hkl})$ as

$$L(\mathbf{q},\mathbf{g}_{hkl}) = \frac{2^3}{\pi^3\sigma_x\sigma_y\sigma_z}\exp\left[-\frac{4}{\pi}\left(\frac{\left(q_x-g_{x,hkl}\right)^2}{\sigma_x^2}+\frac{\left(q_y-g_{y,hkl}\right)^2}{\sigma_y^2}+\frac{\left(q_z-g_{z,hkl}\right)^2}{\sigma_z^2}\right)\right] \tag{79}$$

with the relative peak widths σ_x, σ_y, and σ_z in each of three orthogonal directions. This distribution is normalized such that $\int_{-\infty}^{\infty}\int_{-\infty}^{\infty}\int_{-\infty}^{\infty} L(\mathbf{q},\mathbf{g}_{hkl})dq_xdq_ydq_z = 1$. This peak shape function is useful in case that the peak widths are determined by the domain size and not by the angular deviations of oriented domains with respect to the macroscopic orientation.

3.8.2. Radial and azimuthal peak shape functions

If angular deviations dominate the azimuthal peak width, then this can be considered in an azimuthal peak shape function. The peak shape function $L(\mathbf{q},\mathbf{g}_{hkl})$ can be factorized into a radial part dependent on the modulus of the scattering vector, $L_q(q,g_{hkl})$, and

an azimuthal part dependent on the deviation angle ψ with respect to the scattering vector, $L_\psi(q,g_{hkl},\psi_{hkl})$ as

$$L(\mathbf{q},\mathbf{g}_{hkl}) = L_q(q,g_{hkl})L_\psi(\mathbf{q},\mathbf{g}_{hkl},\psi_{hkl}) \tag{80}$$

This peak shape function is normalized such that

$$\int_0^{\infty}\int_0^{\pi}\int_0^{2\pi} L_q(q,g_{hkl})L_\psi(q,g_{hkl},\psi_{hkl})q^2\sin\psi d\theta d\psi dq \tag{81}$$
$$= 2\pi\int_0^{\infty} L_q(q,g_{hkl})\int_0^{\pi} L_\psi(q,g_{hkl},\psi_{hkl})q^2\sin\psi d\psi dq = 1$$

with the polar angles ψ and θ.

3.8.3. Radial peak shape functions

The normalized radial peak shape functions are given by

$$L_q(q,g_{hkl}) = \begin{cases} \dfrac{2}{\pi\delta_q}\exp\left[-\dfrac{4(\mathbf{q}-\mathbf{g}_{hkl})^2}{\pi\delta_{Gq}^2}\right] & \text{Gaussian} \\[4mm] \dfrac{2}{\pi\delta_q}\left(1+\dfrac{4(\mathbf{q}-\mathbf{g}_{hkl})^2}{\delta_q^2}\right)^{-1} & \text{Lorentzian} \end{cases} \tag{82}$$

where δ_q is the radial peak width. The radial peak shape functions are normalized such that $\int_0^{\infty} L_{hkl}(q,g_{hkl})dq = 1$. In case of the Lorentzian δ_q is equal to the full width at half maximum (FWHM), whereas in case of the Gaussian δ_{Gq} is related to the standard deviation as $\sigma = \sqrt{\frac{\pi}{8}}\delta_{Gq}$ and to the full width at half maximum $\delta_q = \sqrt{\pi\ln 2}\,\delta_{Gq}$. Other peak shapes including the Pseudo–Voigt and Pearson-VII peak shape functions are considered in the Appendix, Sections A.7 and A.8.

3.8.4. Azimuthal peak shapes

Here we consider peak shape functions of similar type, i.e.

$$\tilde{L}_\psi(q,\psi_{hkl}) = \begin{cases} c_G\exp\left[-\dfrac{4\psi_{hkl}^2 q^2}{\pi\delta_{G\psi}^2}\right] & \text{Gaussian} \\[4mm] c_L\left(1+\dfrac{4\psi_{hkl}^2 q^2}{\delta_\psi^2}\right)^{-1} & \text{Lorentzian} \end{cases} \tag{83}$$

which are obtained from the radial peak shape functions by substituting $(\mathbf{q}-\mathbf{g}_{hkl})\rightarrow\psi_{hkl}$ and $\delta_q\rightarrow\delta_\psi q$. c_G and c_L are the normalization factors that have to be determined. ψ_{hkl} is the angle between the scattering vector $\mathbf{q}$ and the lattice vector $\mathbf{g}_{hkl}$ which is given by $\psi_{hkl} = \arccos\left(\frac{\mathbf{g}_{hkl}\cdot\mathbf{q}}{|\mathbf{g}_{hkl}|\cdot|\mathbf{q}|}\right)$. The azimuthal peak width of the reflections is not characterized by a mean deviation angle, but rather by a mean deviation circular arc $\delta_{hkl}=\psi_{hkl}q$ or azimuthal peak width δ_ψ assumed to be the same for all hkl-reflections (see Fig. 15).

3.8.5. Gaussian azimuthal peak shape function

For the normalization the integral $\int_0^{\pi}\tilde{L}_\psi(q,\psi)\sin\psi d\psi$ in Eq. (81) has to be evaluated. In case of a Gaussian distribution the integration leads to a function

$$K(a) = \int_0^{\pi} e^{-a\psi^2}\sin\psi d\psi = \left(\frac{\pi}{16a}\right)^{1/2}\exp\left[-\frac{1}{4a}\right] \tag{84}$$
$$\times\left(2\text{erfi}\left[\frac{1}{2\sqrt{a}}\right]-\text{erfi}\left[\frac{1}{2\sqrt{a}}-i\pi\sqrt{a}\right]-\text{erfi}\left[\frac{1}{2\sqrt{a}}+i\pi\sqrt{a}\right]\right)$$

with $a = \frac{4q^2}{\pi\delta^2}$. erfi[$z$] is the complex error function [15]. The limiting values of the integral $K(\alpha)$ are $\lim_{a\to\infty} K(a) = \frac{1}{2a}$ and $\lim_{a\to 0} K(a) = 2$ ("isotropic limit"). We are then left with the integration

$$\int_0^\infty \int_0^\pi \int_0^{2\pi} L_q(q, g_{hkl}) L_\psi(q, \psi_{hkl}) q^2 \sin\psi d\theta d\psi dq = 2\pi c_G \int_0^\infty L_q(q, g_{hkl}) q^2 K(a) dq = 1$$

(85)

This integral would have to be numerically evaluated for all values of the Miller-indices h, k, and l which would be very time-consuming. To solve this integral analytically, we note that the radial peak shape function $L_q(q, g_{hkl})$ is a function of the difference $L_q(g_{hkl} - q)$ and is normalized (Eq. (82)). If the radial peak-shape function is sufficiently sharp, it has with respect to the integration in Eq. (85) similar properties as the delta function $\delta(g_{hkl} - q)$, i.e. $\int_0^\infty \delta(g_{hkl} - q) q^2 K(a) dq = g_{hkl}^2 K(a_{hkl})$. We thus approximate the convolution-type integral in Eq. (85) as

$$\int_0^\infty L_q(g_{hkl} - q) q^2 K(a) dq = g_{hkl}^2 K(a_{hkl})$$

(86)

with $a_{hkl} = \frac{4g_{hkl}^2}{\pi\delta^2}$. Then the integral is obtained as

$$\int_0^\infty \int_0^\pi \int_0^{2\pi} L_q(q, g_{hkl}) L_\psi(q, \psi_{hkl}) q^2 \sin\psi d\theta d\psi dq = 2\pi c_G g_{hkl}^2 K(a_{hkl}) = 1 \quad (87)$$

from which the normalization constant can be derived as $c_G = \frac{1}{2\pi g_{hkl}^2 K(a_{hkl})}$. The azimuthal peak shape function has asymptotic values of $\lim_{a\to\infty} L_\psi(q, \psi) = 0$ and $\lim_{a\to 0} L_\psi(q, \psi) = \frac{1}{4\pi q^2}$ ("isotropic" limit). The analytical calculation of the function $K(a_{hkl})$ is described in the Appendix, Section A.5.

3.8.6. Lorentzian azimuthal peak shape function

For the normalization the integral in Eq. (81) involves the integration of the Lorentzian

$$K(b) = \int_0^\pi \frac{1}{b + \psi^2} \sin\psi d\psi$$

(88)

with $b = \frac{4q^2}{\delta^2}$. $K(b)$ has a complicated analytical expression in terms of hyperbolic cosine- and sine integrals which is not useful for numerical

calculations. A description in terms of a series expansion at low q and an asymptotic expansion at high q are given in the Appendix (Section A.6) and allow to compute $K(b)$ over the whole b-range. The limiting values of the integral are $\lim_{b\to\infty} K(b) = \frac{\ln(b\pi^2)}{2b}$ and $\lim_{b\to 0} K(b) = 2$. To solve the integral in Eq. (81) analytically we also assume a sufficiently sharp radial peak shape function to obtain

$$\int_0^\infty \int_0^\pi \int_0^{2\pi} L_q(q, g_{hkl}) L_\psi(q, \psi_{hkl}) q^2 \sin\psi d\theta d\psi dq = 2\pi c_L \int_0^\infty L_q(q, g_{hkl}) q^2 K(b_{hkl}) dq = 1$$

(89)

with $b_{hkl} = \frac{4g_{hkl}^2}{\delta^2}$. We thus obtain the normalization constant as $c_L = \frac{1}{2\pi g_{hkl}^2 K(b_{hkl})}$.

Expressions in terms of other peak shape functions such as the pseudo-Voigt and Pearson VII function, which includes the Modified Lorentz-I and Lorentz-II functions as special cases, are given in the Appendix (Sections A.7 and A.8).

To summarize, the two normalized azimuthal distribution functions are given by

$$\tilde{L}_\psi(q, g_{hkl}, \psi_{hkl}) = \begin{cases} \dfrac{1}{2\pi g_{hkl}^2 K(a_{hkl})} \exp\left[-\dfrac{4\psi_{hkl}^2 q^2}{\pi\delta_\psi^2}\right] & \text{Gaussian} \\[3mm] \dfrac{1}{2\pi g_{hkl}^2 K(b_{hkl})} \left(1 + \dfrac{4\psi_{hkl}^2 q^2}{\delta_\psi^2}\right)^{-1} & \text{Lorentzian} \end{cases}$$

(90)

In the isotropic limit ($\alpha \to 0$, $b \to 0$) they reduce to $L_\psi(g_{hkl}) = \frac{1}{4\pi g_{hkl}^2}$.

We note that closed analytical expressions for peak shape functions derived from cosine-type [16], Cauchy-type and Gaussian-type [17], and a special type orientational distribution function derived by Ruland and Tompa [18,19] have recently been applied to orientational lamellar, cylindrical and spherical microdomains.

3.9. Peak widths and coherence lengths

There are many factors that affect the peak width such as instrumental coherence limitations due to primary beam wavelength distribution and angular spread, or coherence limitations due to the lattice because of finite domain size, impurities, lattice defects, strain,
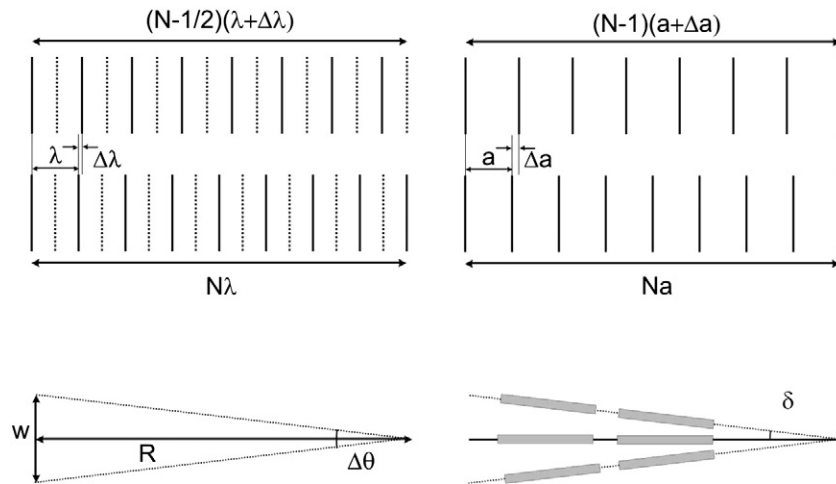

Fig. 12. Scheme illustrating the definition of the longitudinal coherence length l_l and the transverse coherence length l_t. (A) shows two waves propagating to the right, where the wavelength of the upper wave deviates from the wavelength of the lower wave by $\Delta\lambda$. After a distance of $l_l = 8\lambda$, the maximum of the lower wave (solid vertical line) coincides with the minimum of the upper wave (dotted vertical line), leading to destructive interference. The distance along which a lattice diffracts coherently can be defined analogously by considering the distance $l_l = Na$, after which the number of lattice planes differ by one. The definition of the transverse coherence length l_t involves the angular spread of a wave defined by the opening angle $\Delta\theta$. Analogously, the deviation angle δ can be used to define the transverse coherence length for a lattice with orientational deviations.

mosaicity, orientational distributions or other phase-destroying effects. The peak shape functions contain the peak width δ for which in case of Gaussian peak shapes a direct relation to the domain size of the crystallites can be given. The intensity that is coherently scattered by N unit cells of dimension a is for large values of N given by [7]

$$\lim_{N \to \infty} I(q) = \frac{\sin^2[Naq/2]}{\sin^2[aq/2]} \cong N^2 \exp\left[-\frac{N^2 a^2 q^2}{4\pi}\right] \tag{91}$$

A comparison with the normalized Gaussian peak shape function (Eq. (82)) yields for the domain size $D = Na$ a direct relation to the peak width δ_G.

$$D = Na = \frac{4}{\delta_G} \tag{92}$$

The coherence limitations due to the wavelength distribution and angular spread of the primary beam are expressed in terms of the longitudinal and transverse coherence lengths [20]. The longitudinal coherence length l_l considers the coherence limitation due to the wavelength spread $\Delta\lambda$. It is defined as the distance $N\lambda$ after which the phase shift between a wave of wavelength λ and a wave of wavelength $\lambda + \Delta\lambda$ is equal to $\lambda/2$ (see Fig. 12) from which it follows that $l_l = \frac{\lambda^2}{2\Delta\lambda}$. In analogy we introduce a lattice coherence length as the distance Na after which the phase shift between a set of unit cells of size a and a set of unit cells of size $a + \Delta a$ is equal to a, as shown in Fig. 12. From this we obtain

$$l_l = \frac{a^2}{\Delta a} \tag{93}$$

The transverse coherence length l_t considers the coherence limitation due to an angular spread $\Delta\theta$ as shown in Fig. 12. It is defined via the angular spread that gives rise to a phase shift of $\lambda/2$ in the interference pattern of a double-slit experiment, and can be expressed in terms of the opening angle $\Delta\theta$ of the beam as seen from the position of the sample $l_t = \frac{\lambda R}{w} = \frac{\lambda}{\tan}(\Delta\theta)$, where R is the distance between source and sample and w the width of the beam (see Fig. 12). If in analogy we consider sets of unit cells that differ in their orientation by an angle $\Delta\theta$ leading to a phase shift of a, then the transverse lattice coherence length is given by

$$l_t = \frac{2a}{\tan(\Delta\theta)} \tag{94}$$

Accordingly the radial peak width δ_{Gq} or the corresponding domain size D_l can be related by

$$D_l = \frac{4}{\delta_{Gq}} = l_l = \frac{a^2}{\Delta a} \tag{95}$$

to a mean deviation Δa from the ideal lattice points. Similarly, the azimuthal peak width $\delta_{G\psi}$ or the corresponding domain size D_ψ can be related by

$$D_\psi = \frac{4}{\delta_{G\psi}} = l_t = \frac{2a}{\tan 2\delta} \tag{96}$$

where the angular spread $\Delta\theta = 2\delta$ has been expressed in terms of the deviation angle. If the peak width is determined by these types of lattice defects, then the parameters $\Delta a/a = a\delta_{Gq}/4$ and $\delta = \arctan(2a/D_\psi)/2$ should be comparable to the mean deviation of the lattice sites σ_a in the Debye–Waller factor (Eq. (73)) and the mean deviation angle $\langle\delta\rangle$ of the orientational distribution of the particles. If, however, due other phase destroying effect, e.g. also limited primary beam coherence, the coherently scattering domain size is smaller, i.e. $D \ll D_l, D_\psi$, then the peak width is determined by these effects and Eqs. (95) and (96) cannot be used. In any of these cases the peak widths δ_{Gq} and $\delta_{G\psi}$ are determined by coherence limitations and are therefore q-independent. This is the case for most of the scattering patterns of nano- and mesoscale materials that we have investigated or that have been reported in literature. In some cases the peak widths are observed to be q-dependent, so that more elaborate methods such paracrystal theory [21] or the Caille-model [22,23] have to be considered. They take into account that the displacements of adjacent particle positions are not independent and yield a closed expression for the lattice factor that is characterized by an approximately Lorentzian peak shape and an integral peak width that increases linearly with q^2. Their consideration to calculate two-dimensional scattering patterns is, however, beyond the scope of the present work.

3.10. Bragg-peaks beyond the Ewald Plane

The explicit consideration of radial and azimuthal peak widths, or equivalently of finite and rather small longitudinal and transverse coherence lengths, leads to the appearance of crystallographically forbidden Bragg-peaks in the calculated scattering patterns. Since peak widths are usually quite large for soft crystals, the observation of these peaks is more a rule than an exception. Attempts to interpret these peaks in terms of crystallographically allowed Bragg-peaks have always been difficult. To facilitate their interpretation, we introduced the concept of
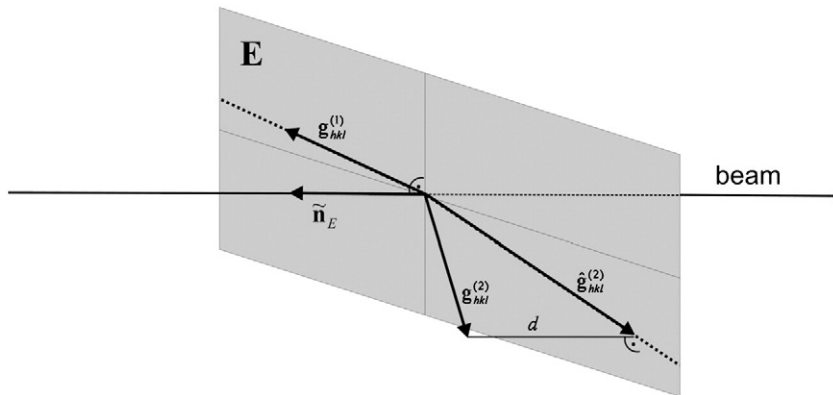

Fig. 13. Scheme showing the Ewald plane **E** and the location of two reciprocal lattice points corresponding to a primary Bragg peak, $\mathbf{g}_{hkl}^{(1)} \in \mathbf{E}$, and a secondary Bragg-peak, $\mathbf{g}_{hkl}^{(2)} \notin \mathbf{E}$, which is located a distance d away from the Ewald plane. A spread of the intensity distribution around $\mathbf{g}_{hkl}^{(2)}$ can lead to reflections at a scattering vector $\mathbf{q} = \hat{\mathbf{g}}_{hkl}^{(2)}$, which would be considered a crystallographically 'forbidden' reflection.

primary and secondary peaks in relation to the Ewald sphere construction [10].

In case of a single crystal, reflections are observed if a reciprocal lattice vector $\mathbf{g}_{hkl}$ is equal to a value of the scattering vector $\mathbf{q}$ observable on the detector plane. This is known as the Laue-condition and is the basis for the Ewald sphere construction. In the small-angle approximation, the component $q_z \approx 0$ so that the Ewald sphere radius becomes infinitely large. Then the Ewald sphere can be approximated by its tangential plane $\mathbf{E}$ through the origin of reciprocal space with (q_x, q_y, $q_z = 0$), which we call Ewald plane. Fulfilment of the Laue-condition then means that the lattice vector $\mathbf{g}_{hkl} = \mathbf{q} \in \mathbf{E}$ is located on the Ewald plane (see Fig. 13).

The orientation of the Ewald plane can be specified by its normal vector $\tilde{\mathbf{n}} = \mathbf{n}/|\mathbf{n}|$ which we assume to be parallel to the primary beam direction and expressed in terms of its coordinates ($\tilde{h}_n, \tilde{k}_n, \tilde{l}_n$). Then the distance of a reciprocal lattice vector $\mathbf{g}_{hkl} = h\mathbf{a}^* + k\mathbf{b}^* + l\mathbf{c}^*$ from the Ewald plane is

$$\mathbf{g}_{hkl}\tilde{\mathbf{n}} = d \tag{97}$$

This is schematically shown in Fig. 13. If $d = 0$ then the vector $\mathbf{g}_{hkl}$ is located in the plane, fulfilling the Laue-condition $\mathbf{g}_{hkl} = \mathbf{q} \in \mathbf{E}$, and gives rise to the hkl-reflection on the area detector. Peaks for which $d = 0$ are called primary Bragg-peaks.

Peaks of finite width have a certain spread in reciprocal space. If this spread is sufficiently large, then also peaks with $d > 0$ can extend into the Ewald plane, thereby fulfilling the Laue-condition $\hat{\mathbf{g}}_{hkl} = \mathbf{q} \in \mathbf{E}$ (see Fig. 13), giving rise to the corresponding hkl-reflection on the area detector. Peaks for which $d > 0$ are called secondary Bragg-peaks. They would be considered as crystallographically "forbidden" Bragg-peaks [10]. The smaller the distance d, or the larger the peak width δ, the higher the intensity of this reflection will be. Their exact location will depend on the detailed peak shape, but for fairly symmetric peak shapes it can be calculated via their projection $\mathbf{g}'_{hkl} = \mathbf{g}_{hkl} - d\tilde{\mathbf{n}}$ on the Ewald plane (see Fig. 13) to be

$$\mathbf{q}^*_{hkl} = \mathbf{g}'_{hkl} \frac{|\mathbf{g}_{hkl}|}{|\mathbf{g}'_{hkl}|} \tag{98}$$

This allows one to estimate the position of secondary Bragg-peaks on the detector in terms of the coordinates in the ($\mathbf{u}$ $\mathbf{v}$) coordinate system, i.e. $q_u = \mathbf{u} \cdot \mathbf{g}^*_{hkl}$ and $q_v = \mathbf{v} \cdot \mathbf{g}^*_{hkl}$.

The effect of finite lattice coherence on the diffraction patterns can now be investigated by model calculations. They allow one to address the fundamental question of how Debye–Scherrer rings transform into Bragg-peaks if an originally isotropic multi-domain structure is oriented in a particular direction. Intuitively, one would expect Debye–Scherrer rings that correspond to (hkl)-lattice planes
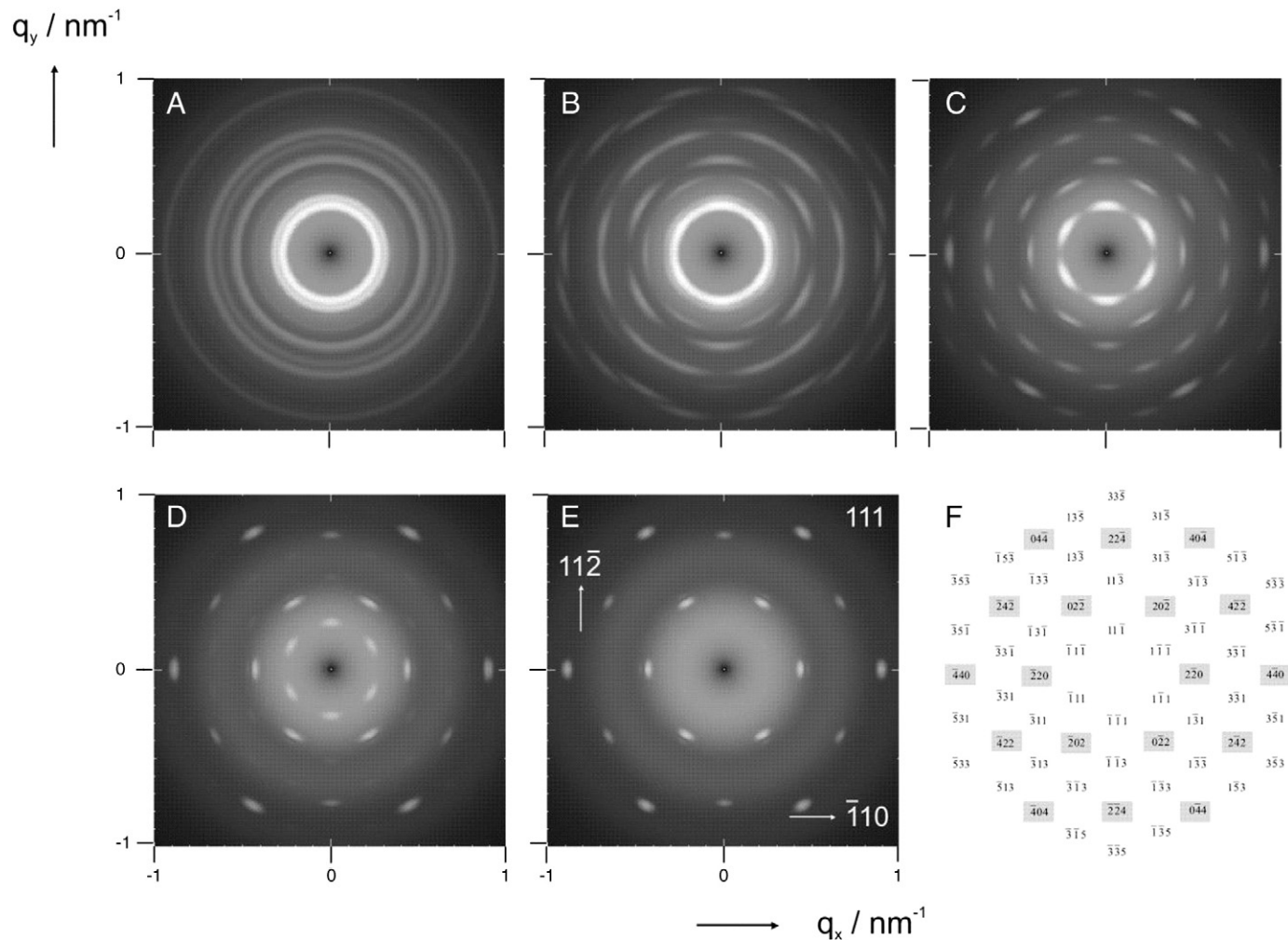

Fig. 14. Development of primary and secondary Bragg-peaks with increasing transverse coherence length. The scattering patterns are calculated for an fcc-lattice with a unit cell dimension $a = 40$ nm, spheres of a radius $R = 10$ nm ($\sigma_R = 0.1$), a mean displacement of $\delta = 2$ nm, and a longitudinal coherence length of $l_l = 200$ nm that determines the radial peak width. The transverse coherence length l_t is increased from 1 nm (A), 30 nm (B), 60 nm (C), 90 nm (D), and 120 nm (E). It is observed that the Debye–Scherrer rings all develop reflections, where the primary reflections stay with increasing orientational order, whereas the secondary reflections gradually disappear. (F) gives the indices of the reflections with the primary reflections indicated by grey.

which are forbidden in this direction to gradually disappear, whereas Debye–Scherrer rings that correspond to (hkl)-lattice planes that are allowed to gradually develop Bragg-peaks. Eventually, all Debye–Scherrer rings would disappear and only allowed Bragg-peaks would remain. The calculations show, however, that there exists a broad intermediate state, where all Debye–Scherrer rings — even those that correspond to forbidden (hkl)-lattice planes – develop Bragg-peaks. Eventually, at higher orientations the Bragg-peaks that belong to forbidden (hkl)-lattice planes loose intensity and disappear.

This is illustrated in Fig. 14 where for an fcc-lattice the transverse coherence length has been increased from a very small value ($l_t = 1$ nm, orientational order parameter $S = 0$) corresponding to an orientationally isotropic state (Fig. 14A) to a large value ($l_t = 120$ nm, $S = 0.99$) corresponding to a highly oriented state aligned in the [111]-direction (Fig. 14E). At the lowest values one observes Debye–Scherrer rings. All of them then develop arc-shaped maxima (Fig. 14B) which then sharpen into well-defined reflections (Fig. 14C). Upon further increase of orientational order all quasi-forbidden reflections weaken (Fig. 14D) and eventually disappear (Fig. 14E), whereas all allowed reflections remain. The diffraction patterns in Fig. 14C and D are characterized by a large number of well-defined, but quasi-forbidden Bragg-peaks. We found with one notable exception in literature [24], that all reported FCC diffraction patterns of soft materials such as block copolymers and their lyotropic liquid crystalline phases [25–30], colloidal dispersions [31–34] and photonic crystals [35] that are oriented in the [111]-direction exhibit such type of diffraction patterns with a large number of quasi-forbidden Bragg-peaks.

To be specific, we consider the case of the quasi-forbidden [11$\bar{1}$]-reflection in Fig. 14 with a modulus of the reciprocal lattice vector of $g_{11\bar{1}} = 2\pi\sqrt{3}/40 = 0.272$ nm^{-1} and a distance $d_{11\bar{1}} = 1/\left(2\pi\sqrt{3}\right) = 0.091$ nm^{-1} (Eq. (97)) to the Ewald plane. For Fig. 14C the transverse coherence length is $l_t = 60$ nm corresponding to a peak width of $\delta = 4/l_t = 0.067$ nm^{-1} (Eq. (96)) so that at a moderate relative peak width of $\delta/q_{11\bar{1}} = 0.25$ (25%) the ratio $\delta/d_{11\bar{1}} = 0.74$ is already of the order unity meaning that a noticeable part of the scattering intensity is located on the Ewald plane giving rise to a Bragg-peak.

The interrelation between peak broadening and the occurrence of secondary Bragg-peaks has been noted early in crystallography [36] and is occasionally observed in electron microscopy when dealing with truncation rod effects or high beam convergence which limits coherence. For soft materials their presence is more a rule than an exception because of two reasons. Firstly, the lattice parameters are typically larger then in "hard" materials. Since the ratio of peak broadening to peak position depends on the coherence measured in the number of unit cells over a certain distance, this effect is more pronounced for materials with large unit cells. Secondly, soft materials are usually multi domain structures. As domains are easy to orient, an external field will lead to the alignment of each individual domain resulting in a macroscopically oriented multidomain structure. Such a material has a limited coherence, because of the finite dimensions of the crystalline domains and in addition, because the domains can be tilted very slightly relative to each other and with respect to the macroscopic orientation such as in the mosaic-type model in Fig. 5D.

3.11. Validity of approach

Since structural features on length scales larger than the unit cell dimension a, such as packing defects, grain boundaries or grain shapes are only indirectly considered via the domain size D, Eq. (25) is not expected to give good agreement with experimentally determined scattering patterns in the range of scattering vectors $q < 2\pi/a$. However, for $q \geq 2\pi/a$, this approach remarkably well describes experimentally measured high-resolution scattering patterns of mesoscopically ordered materials as will be shown and discussed below.

Most of the structural variables discussed above, i.e. unit-cell dimension a and relative displacement σ_a, particle radius R and relative standard deviation σ_R, have a specific effect on the scattering curve:

- unit-cell dimension $a \rightarrow$ absolute peak positions,
- lattice-type $\rightarrow$ relative ratio of peak positions,
- lattice-orientation $\rightarrow$ peak positions,
- domain size, longitudinal coherence $\rightarrow$ radial peak width,
- azimuthal domain size, transverse coherence $\rightarrow$ azimuthal peak width,
- displacement $\rightarrow$ damping of higher-order reflections,
- particle radius $\rightarrow$ position of form factor oscillations,
- particle shape $\rightarrow$ relative position of form factor oscillations,
- particle polydispersity $\rightarrow$ damping of higher-order oscillations,
- particle orientational distribution $\rightarrow$ azimuthal intensity distribution of form factor

This is favorable for adjusting the parameters in model calculations to obtain good agreement between measured and calculated scattering patterns. In principle, it is even possible to fit calculated scattering patterns to measured scattering patterns using the expression for $I(q)$ in Eq. (25). As the number of data points is often of the order of 10^6, and because the structural information contained in most regions of the scattering patterns is highly redundant, this is not the most practical way to analyze scattering patterns. It is more efficient to select regions or lines and circles from the scattering pattern that contain characteristic features such as peaks or oscillations and fit Eq. (25) to these regions as is possible with a freely available software *Scatter* that uses the equations derived in this manuscript and employs Simplex/Levenberg–Marquardt algorithms in the fitting routines [37,38]. Since each fit parameter has a specific effect on the scattering curve, the off-diagonal elements of the covariance matrix, as obtained from the Levenberg–Marquardt algorithm, are in most cases low indicating reasonable statistical independence. This allows one to quickly determine the set of structural parameters from measured scattering patterns. We are not aware of any other currently available approach that could similarly model or fit scattering patterns to quantitatively describe high-resolution synchrotron SAXS- and SANS-patterns of many different mesoscopically ordered materials to extract the full structural information.

In the following we consider some examples of scattering patterns measured for nano- and mesoscale materials to demonstrate the potential of the method to describe experimental scattering patterns whose quantitative descriptions have represented a considerable challenge. These include the interpretation of the gyroid "10-spot pattern" (Section 4.2), the quantitative determination of the orientational distribution of shear-oriented cylindrical micelles from measured SANS-patterns (Section 4.3), and the quantitative description of the scattering patterns of stretched SBS thermoplastic elastomers (Section 4.4), the quantitative description of scattering patterns of highly ordered sheared lyotropic liquid crystalline phases (Section 4.5), shear-oriented nanocomposites (Section 4.6), and mesoporous single crystalline materials (Section 4.7).

4. Results and discussion

In the following we will use the equations derived in Section 3 to provide model calculations for a number of particularly relevant examples or cases that have been challenging. To give an overview of the equations that are used in the following and how they are related, a summary is given in Table 3.

4.1. Model calculations

Throughout the following examples the scattering patterns $I(\mathbf{q}) = I(q_x, q_y, q_z)$ are calculated for the case $q_z = 0$ which corresponds to the small-angle approximation (Eq. (7)). It is convenient, because the vectors **u** and **v** as well as the components q_x and q_y are linearly
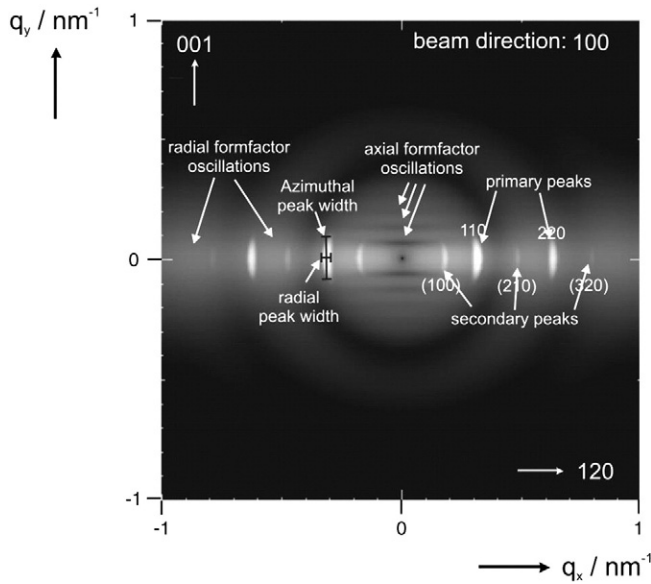
Fig. 15. Calculated scattering pattern for hexagonally packed and oriented cylinders. The pattern exhibits typical features such as primary and secondary reflections as well as form factor oscillations related to the cylinder length and cross-section.

from the primary beam source, can be calculated by numerically integrating

$$\rho(x,y) = \int\limits_{z_-}^{z_+} \rho(x,y,z)dz \tag{99}$$

where the integration limits z_+ and z_- are chosen to extend the integration over at least one unit cell. This provides an image of the sample as would be obtained from a transmission electron micrograph, where the difference $|z_+ - z_-|$ would correspond to the sample thickness of the specimen. A real space visualization of structures is in many cases very useful for the interpretation of data extracted from the scattering patterns.

As an example, we calculated the scattering pattern of hexagonally packed cylinders probed with the beam parallel to the [100]-direction, which is perpendicular to the cylinder axis ([001] direction). We used a cylinder-to-cylinder distance of $a = 40$ nm, a cylinder length of $L = 100$ nm ($\sigma_L = 0.1$), and a cylinder radius of $R = 10$ nm ($\sigma_R = 0.1$). This corresponds to a cylinder volume fraction of $\phi = 0.23$ which is typical e.g. for block copolymers. We used a radial domain size or longitudinal coherence length of $l_l = 400$ nm, and an azimuthal domain size of transverse coherence length of $l_t = 100$ nm, which are typical values for soft, mesoscopic systems. The orientational distribution of the cylinders is chosen to be of Onsager-type with a value of $\overline{\delta} = 2.8°$ corresponding to a mean deviation angle of $\langle\delta\rangle = 5.7°$ which is chosen to be consistent with the mean deviation angle derived from the transverse coherence length (Eq. (96)). This corresponds to a quite narrow orientational distribution with an order parameter of $S = 0.98$. The mean deviation from the lattice points (Debye–Waller factor, Eq. (73)) was $\sigma_a = 2$ nm, chosen to be consistent with the mean deviation calculated from the longitudinal coherence length (Eq. (95)). The intensity is displayed on a logarithmic scale over 6 orders of magnitude. The image exhibits typical features often encountered in experimental scattering patterns of soft materials. These comprise the damped radial and axial form factor oscillations, as well as primary and secondary Bragg-peaks with certain radial and azimuthal peak widths. These features are indicated in Fig. 15. The chosen approach provides a mathematical description that is as exact as necessary, while being as fast as possible. The calculation of the whole scattering pattern took ca. 60 s for an image of 240×240 pixels on a standard laptop computer.

4.2. Gyroid scattering patterns

The gyroid is an infinitely connected triply periodic minimal surface with space group Ia3d discovered by Schoen in 1970. [39] In
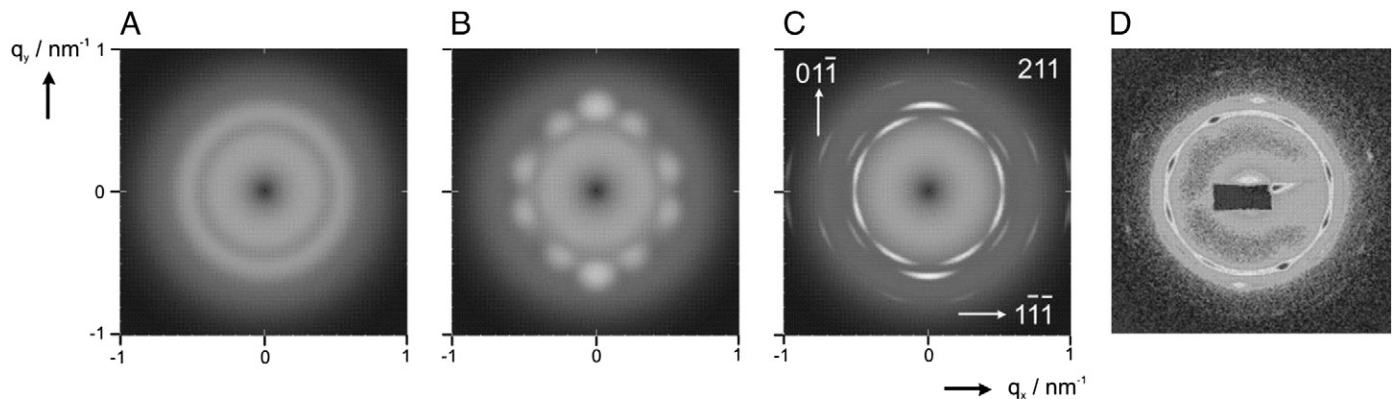
related to the dimensions l_x and l_y on the detector (see Fig. 1), which simplifies calculations, and for the chosen examples this is a very good approximation. In general, scattering patterns can also be calculated without relying on the small-angle approximation. The values of q_x and q_y, and also of q_z then depend on the position (l_x, l_y) on the detector. With a given sample-distance d the scattering angle $\theta = \arctan(l/d)$ (Eq. (5)) and the polar angles $\vartheta = \arctan(l_x/d)$ and $\varphi = \arctan(l_y/l_x)$ (Eq. (4)) can be calculated from which the components of the scattering vector $\mathbf{q} = (q_x, q_y, q_z)$ can be obtained from Eq. (3).

The orientation of the unit cell in terms of the reciprocal lattice vectors ($\mathbf{a}^*$, $\mathbf{b}^*$, $\mathbf{c}^*$) is specified by the beam direction, $\mathbf{n}_{hkl} = h_n\mathbf{a}^* + k_n\mathbf{b}^* + l_n\mathbf{c}^* = (h_n, k_n, l_n)$, as well as the direction parallel to the x-axis of the detector, $\mathbf{u}_{hkl} = h_u\mathbf{a}^* + k_u\mathbf{b}^* + l_u\mathbf{c}^* = (h_u, k_u, l_u)$. With the reciprocal lattice vectors ($\mathbf{a}^*$, $\mathbf{b}^*$, $\mathbf{c}^*$) given, the lattice vectors $g_{hkl} = h\mathbf{a}^* + k\mathbf{b}^* + l\mathbf{c}^*$ can be calculated which is needed in Eq. (70) for the calculation of the lattice factor. With Eq. (16), also the orientation of the unit cell in terms of the lab-fixed coordinate system can be calculated. From the orientation and dimension of the unit cell and the structural parameters of the particles, a real-space projection of the sample parallel to the direction of the primary beam, as viewed

Fig. 16. (A) Calculated scattering pattern for a gyroid in the isotropic state (A) and oriented with the 211-direction parallel to the beam. The characteristic 10-spot pattern is obtained for small domain sizes ($l_l = 40$ nm) (B). For larger domain sizes ($l_l = 300$ nm) the peaks develop into sharp arcs (C). This well reproduces the measured scattering pattern of a shear-oriented gyroid phase (D) [47].
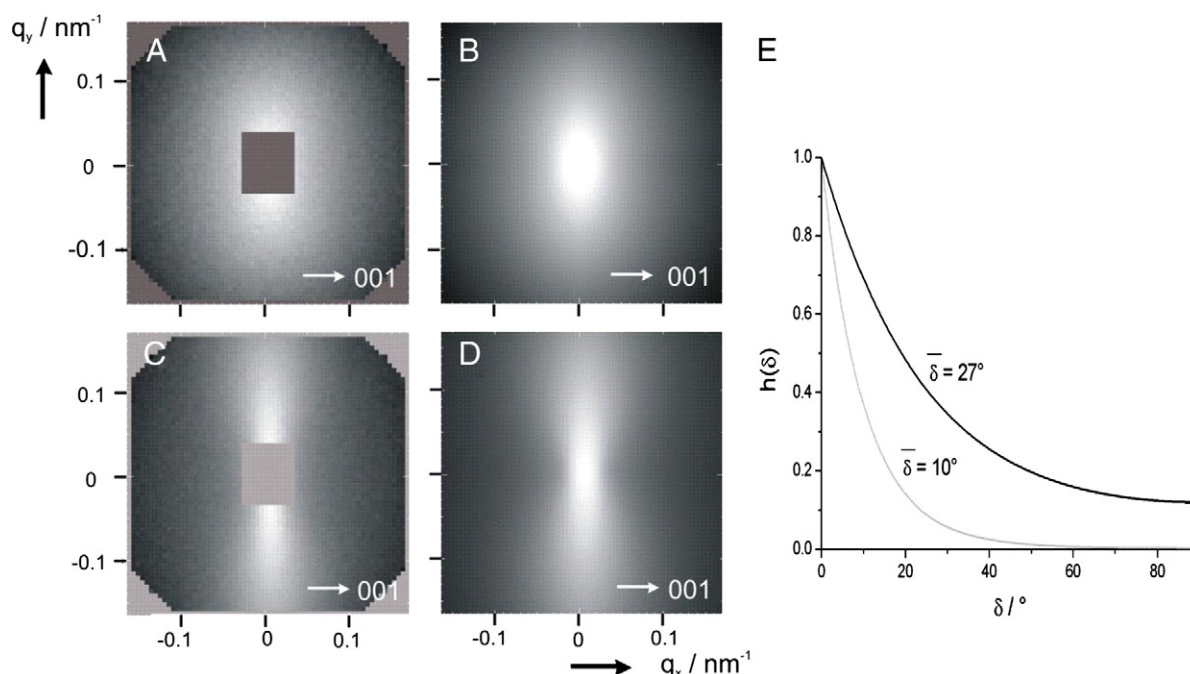
Fig. 17. Measured SANS scattering patterns of cylindrical micelles shear-oriented with a shear rate of $\dot{\gamma} = 1\ s^{-1}$ (A) and $\dot{\gamma} = 500\ s^{-1}$ (C) together with the calculated scattering patterns (B, D). The calculations were performed for cylinders having a length of $L = 250$ nm ($\sigma_L = 0.3$), a cross-sectional radius of $R = 10$ nm ($\sigma_R = 0.13$) assuming an Onsager distribution function with a value of $\overline{\delta} = 27°$ corresponding to $\langle\delta\rangle = 45.4°$ and $S = 0.25$ for the low shear rate, and a value of $\overline{\delta} = 10$ corresponding to $\langle\delta\rangle = 23.9$ and $S = 0.69$ for the high shear rate. The two distribution functions are shown in (E) as a function of the deviation angle.

nature, gyroid structures are found for certain lipids, surfactants, and block copolymers [40–42]. Because of its characteristic texture, the diffraction pattern observed for shear-oriented samples has been called the "ten-spot pattern", as ten distinctive Bragg peaks are observed on the first Debye–Scherrer ring. This scattering pattern is a typical example for the occurrence of secondary Bragg-peaks. In Fig. 16 calculated scattering patterns for the gyroid phase are shown for the isotropic case ($l_t = 2$ nm, $l_r = 40$ nm) and for an oriented state ($l_t = 40$ nm) with the [211]-direction parallel to the beam. The calculation was done for a unit cell of $\alpha = 30$ nm and a volume fraction of $\phi = 0.35$. For small domain sizes ($l_l = 40$ nm) the characteristic ten-spot pattern can be well reproduced (Fig. 16B). The 10 peaks on the inner Debye–Scherrer ring that give rise to the 10-spot pattern are all secondary, quasi-forbidden 211 reflections. For larger domain sizes ($l_l = 300$ nm) the 211-reflection on the meridian disappears and the allowed 220 reflection becomes dominant on the meridian (Fig. 16C). This calculation can be well compared to a measured scattering pattern for a diblock copolymer gyroid phase (Fig. 16D) [43]. The agreement, also for the higher order reflections, is remarkable indicating that the approximation discussed in Section 3.8 can give very satisfactory descriptions of the scattering patterns of ordered bicontinuous structures.

4.3. Shear-oriented cylindrical micelles

When applying continuous shear, cylindrical micelles orient in shear direction. With increasing shear rate, the degree of orientation increases which is accompanied by a pronounced shear thinning of the solution. Such systems can be well investigated by rheo-SANS experiments which measure the rheological response of the sample while probing structural changes on a scale of 1–100 nm. The example in Fig. 17 shows measured SANS-patterns from dilute solutions of cylindrical micelles at two different shear rates. The experiments were performed at the instrument D11 at ILL, Grenoble. At a low shear rate of $\dot{\gamma} = 1\ s^{-1}$, the measured scattering pattern is slightly anisotropic, whereas at a higher shear of $\dot{\gamma} = 500\ s^{-1}$, there is a strong anisotropy.

The "8"-shaped scattering patterns indicate the cylindrical micelles to be oriented in the horizontal direction, i.e. in the direction of shear. The calculated scattering patterns in Fig. 17 show good agreement with the measured scattering patterns. For the calculations we assumed the cylindrical micelles to have a length of $L = 250$ nm ($\sigma_L = 0.3$) and a radius of $R = 10$ nm ($\sigma_R = 0.13$). For the orientational distribution an Onsager distribution function was used, as would be theoretically expected. The scattering pattern for the high degree of orientation was calculated with a parameter $\overline{\delta} = 10°$, which corresponds to a mean angle of $\langle\delta\rangle = 24°$ and an orientational order parameter of $S = 0.69$. The scattering pattern for low degree of orientation was calculated with a parameter $\overline{\delta} = 27°$, which corresponds to a mean angle of $\langle\delta\rangle = 45°$ and an orientational order parameter of $S = 0.25$. The greyscale is the same for all images. We observe nearly quantitative agreement between measured and calculated scattering patterns. The corresponding orientational distributions of the cylinders as a function of the deviation angle δ are shown for the two shear rates in Fig. 17E. This demonstrates that systems of oriented cylinders can well be described by using the approximations in Eqs. (50) and (51).

4.4. Oriented Kraton thermoplastic elastomer

Styrene–butadiene–styrene (SBS) triblock copolymers (Kraton) are widely used as thermoplastic elastomers. SBS elastomers have a microphase separated structure with spherical or cylindrical polystyrene domains that form an ordered lattice in a continuous polybutadiene matrix. The macroscopic properties of these materials depend very much on the exact microstructure. SBS with highly oriented cylindrical microdomains can be prepared by roll-casting. Such highly anisotropic samples behave mechanically different when stretched perpendicular or parallel to the cylinder axis. To obtain detailed structural information, such samples can be stretched in a particular direction while the microstructure is probed by small-angle x-ray scattering. The scattering pattern in Fig. 18A is from a stretched SBS-thermoplastic elastomer (molecular weight 140,000 g/mol, 30 wt.% PS) that was strained to 38% of its original length perpendicular to the
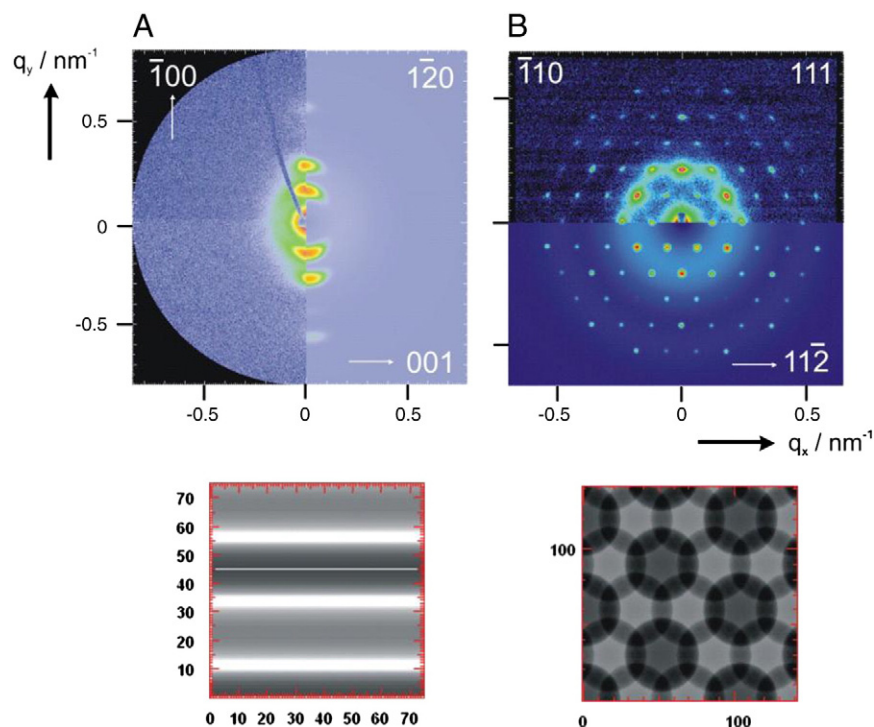
Fig. 18. Examples of measured synchrotron SAXS patterns recorded for a stretched SBS thermoplastic elastomer (A), and a shear-oriented lyotropic block copolymer phase with fcc-structure (B). The corresponding calculated scattering patterns are merged into the right half (A) and the lower half (B) of the measured patterns. Below the scattering patterns are the calculated real space projections of the structures. The scales are in [nm].

cylinder axis [44]. The measurement was performed on the beamline BW4 at HASYLAB/DESY, Hamburg. It shows a set of nearly equidistant reflections on the meridian indicating that the polystyrene cylinders are highly ordered and oriented horizontally.

The calculated scattering pattern is in good agreement with the measured scattering pattern. The calculations assume the beam direction to be perpendicular to the cylinder axis, more specifically, parallel to the $[1\bar{2}0]$-direction of the 2-dimensional hexagonal unit cell defined in Fig. 10. This gives rise to a set of equidistant peaks on the meridian of the scattering pattern. The radial peak width is smaller than the azimuthal peak width which is quite generally the case for ordered soft materials. Both, the radial and the azimuthal peak widths are q-independent, indicating that the peak widths are determined by coherence-limiting effects specified by the longitudinal and transverse coherence length as discussed in Section 3.9. From the peak width values for the longitudinal and transverse coherence lengths of $l_l = 200$ nm and $l_t = 65$ nm are obtained, which is of the order of a few unit cell dimensions. This seems surprisingly small, but investigations using electron microscopy [10] show that domain sizes and angular deviations derived from the analysis of the scattering patterns are in good agreement with the electron micrographs. From the peak positions a value of $a = 45.0$ nm for the hexagonal unit cell size, i.e. the distance between two adjacent cylinders, can be derived. The formfactor determines the decay of the intensity with increasing q and the relative height of the higher order peaks. In particular, the cylinder cross-section primarily affects the intensity of the peaks along the meridian. From this the cylinder radius is obtained as $R = 9.5$ nm ($\sigma_R = 0.15$). The cylinder length affects the intensity along the equator, and from this the cylinder length is determined to be $L = 120$ nm ($\sigma_L = 0.3$). The cylinders are oriented 2.5° off the horizontal direction, which is taken into account in the calculation. In order to provide a quantitative comparison between measured and calculated scattering pattern, the calculated scattering pattern has been merged into the right half of the measured scattering pattern in Fig. 18A. Also shown is the real space projection calculated from Eq. (99).

4.5. Lyotropic FCC phase

Lyotropic liquid crystalline phases can show remarkably high degrees of order. These phases can be shear-aligned to form single-crystalline samples that show a large number of Bragg-peaks. Often the analysis of these scattering patterns is difficult due to the occurrence of secondary Bragg-peaks. The scattering pattern in Fig. 18B is from a 15 wt.% solution of poly(isoprene-b-ethylene oxide) (PI-PEO, molecular weight 12,700 g/mol) in water oriented by using continuous shear at a shear rate of $\dot{\gamma} = 500$ s^{-1} in a Couette shear cell and then stopped to trap the oriented structure. Experiments were performed at the beamline ID02 at ESRF, Grenoble [45]. At this concentration the PI-PEO block copolymer forms spherical micelles that form a highly ordered FCC lattice.

For the calculated scattering pattern the sample was assumed to be oriented such that the [111]-direction is parallel to the beam. This corresponds to an orientation of the hexagonally packed sphere layers in the shear direction, normal to the beam. For the calculations a core radius of the micelles with a value of $R = 12.4$ nm ($\sigma_R = 0.06$), and a unit cell dimension of $a = 85$ nm was used. The peak shape was assumed to be anisotropic Gaussian with domain sizes of $D_{110} = D_{211} = 500$ nm and $D_{111} = 120$ nm, indicating that the coherence in the [111]-direction, perpendicular to the hexagonally packed sphere-layers, is much smaller compared to the in-layer coherence. The mean deviation from the lattice points (Debye-Waller factor) was assumed to be $\sigma_a = 3$ nm. For quantitative comparison, the calculated scattering pattern was merged into the lower half of the measured scattering pattern. The observed agreement is remarkable. The real-space projection as calculated from Eq. (99) is shown below. The particular pattern results from an overlap of the projected spheres in adjacent (111)-layers.

4.6. Nanoparticle superlattice

Nanoparticles dispersed in solution or polymeric matrices often show pronounced aggregation so that scattering patterns show only
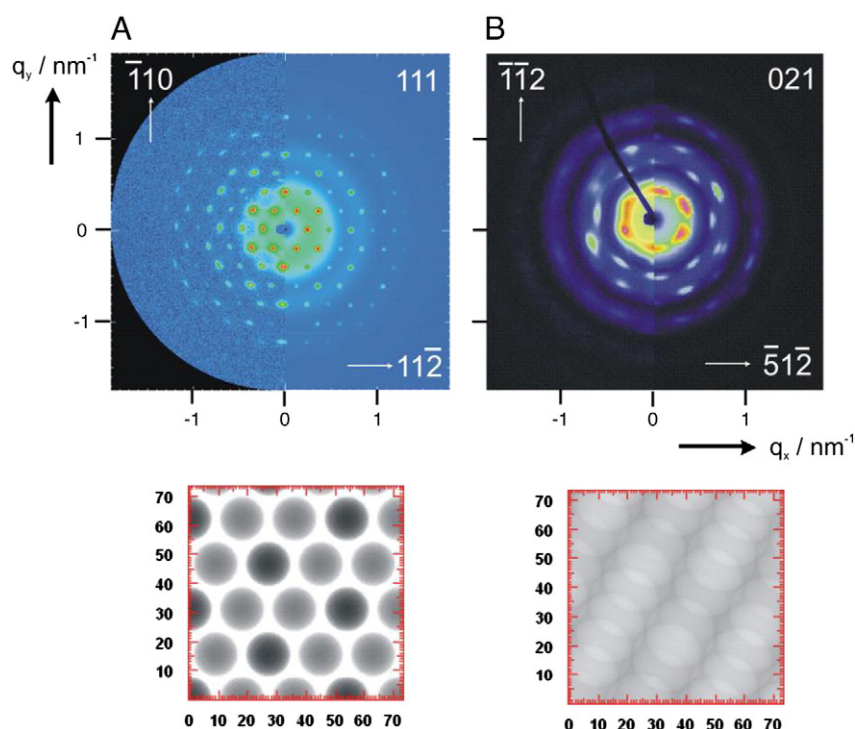
Fig. 19. Examples of measured synchrotron SAXS patterns recorded for a shear-oriented magnetite nanoparticle gel (A), and a mesoporous silica single crystal, that has been rotated on a goniometer stage (B). The corresponding calculated scattering patterns are merged into the right half of the measured patterns. Below the scattering patterns are the calculated real space projections of the structures. The scales are in [nm].

few distinct features. When nanoparticles are coated with a stabilizing layer of polymers they can be well dispersed in solvents up to concentrations where they start to form superlattices resulting in scattering patterns with a large number of Bragg-peaks. The scattering pattern in Fig. 19A has been obtained from a concentrated solution of polystyrene-coated magnetite nanoparticles in toluene. The sample was oriented using oscillatory shear and investigated at the beamline BW4 at HASYLAB/DESY, Hamburg [35]. The nanoparticles arrange into an FCC-structure with the [111]-direction oriented parallel to the x-ray beam, very similar to the lyotropic liquid crystalline phase in Fig. 18B.

For the calculated scattering pattern the unit cell dimension was assumed to be $a = 44$ nm, with a radius of the nanoparticles of $R = 7.7$ nm ($\sigma_R = 0.09$). For the peak shape we assumed an anisotropic Gaussian with widths of $D_{110} = D_{211} = 200$ nm and $D_{111} = 50$ nm. As the mean deviation from the lattice points we used $\sigma_\alpha = 1$ nm. For quantitative comparison the calculated scattering pattern was merged into the right half of the measured scattering pattern. Also in this case the agreement is remarkable. The real space projection is also shown.

4.7. Mesoporous silica

When mesoporous oxides are prepared from well-ordered lyotropic templates, highly ordered mesoporous structures can be obtained [1,6]. The templating procedure even allows the preparation of mesopore single crystals [10]. The scattering pattern in Fig. 19B is from a mesoporous silica that has been prepared from a shear-oriented lyotropic single crystalline template (FCC) by sol/gel-synthesis. The mesoporous single crystal was mounted on a goniometer stage at the beamline BW4 at HASYLAB/DESY, Hamburg. The sample was mounted such that the [111]-direction was oriented parallel to the x-ray beam and rotated by 180° around its vertical $\overline{11}2$-axis [10,46]. The diffraction pattern in Fig. 19B was recorded at a rotation angle of $\alpha = 39°$. which corresponds to

probing the [210]-direction of the FCC-pore lattice. The pore radius was $R = 10.3$ nm, the unit cell $a = 41.5$ nm. Twinning of the sample had been taken into account with a ratio of 85:15. For quantitative comparison the calculated scattering pattern was merged into the right half of the measured scattering pattern. Also in this case the agreement is remarkable. The real space projection of the major twin is also shown.

5. Conclusions

We have outlined a general and versatile mathematical framework that yields analytical expressions for the scattering patterns of a wide variety of particles and lattices of nano- and mesostructured materials. It considers particle size and orientational distributions, takes into account radial and azimuthal peak shapes of different kind, and provides means for the transformation of coordinates and directions between lab-based and sample-based coordinate systems. It outlines approximations that leave calculations as exact as necessary, while enabling a computational speed that is as fast as possible. It allows for the first time to quantitatively describe, model and even fit experimentally measured SAXS and SANS-patterns of nano- and mesoscale materials with examples shown for micellar solutions, block copolymers, lyotropic liquid crystals, nanocomposites and mesoporous structures. The method has been implemented into a software to make it publically available for the analysis of scattering experiments of a wide variety of materials.

Appendix A

A.1. Factorization of the orientational distribution function

We assume that the orientational distribution of the cylinders, $h(\delta)$, is determined by the orientational distribution of the domains, $h'(\delta')$, and the orientational distribution of the cylinders within each domain, $h''(\delta-\delta')$. Then the orientational distribution of the cylinders can be written as a convolution

$$h(\delta) = h'(\delta)*h''(\delta) = \int h''(\delta-\delta')h'(\delta')d\delta' \tag{A1}$$

If the domains are perfectly oriented, then $h'(\delta')$ approaches a delta function, i.e. $h'(\delta') \rightarrow \delta[\delta']$, so that $h(\delta) = \int h''(\delta-\delta')h'(\delta')d\delta' = \int h''(\delta-\delta')\delta[\delta']d\delta' = h''(\delta)$ which means that the orientational distribution of the cylinders is equal to the orientational distribution within the domains. If the cylinders are perfectly aligned within the domains, then $h''(\delta-\delta')$ approaches a delta function, i.e. $h''(\delta-\delta') \rightarrow \delta[\delta-\delta']$ so that $h(\delta) = \int h''(\delta-\delta')h'(\delta')d\delta' = \int \delta[\delta-\delta']h'(\delta')d\delta' = h'(\delta)$ which means that the distribution function of the cylinders is equal to the orientational distribution of the domains.

We assume we have a formfactor-type function $f(\delta)$ and a lattice factor-type function $g(\delta')$ that depend on the deviation angle δ of the cylinders and the deviation angle δ' of the domains. For the calculation of the average over the orientational distribution as in Eq. (20) we have to evaluate the integral

$$\langle f(\delta)g(\delta') \rangle = \int f(\delta)g(\delta')h(\delta)d\delta = \int\int f(\delta)g(\delta')h''(\delta-\delta')h'(\delta')d\delta d\delta' \tag{A2}$$

We can distinguish between three cases:
A) If the domains are nearly perfectly oriented, then $h'(\delta')$ approaches a delta function, i.e. $h'(\delta') \rightarrow \delta[\delta']$ so that

$$\langle f(\delta)g(\delta') \rangle = \int\int f(\delta)g(\delta')h''(\delta-\delta')\delta[\delta']d\delta d\delta' = g(0)\int f(\delta)h''(\delta)d\delta = g(0)\langle f \rangle'' \tag{A3}$$

This means that the orientational average of the product is the product of the lattice-type function $g(\delta'=0)$ and the average of the formfactor-type function $f(\delta)$ over the orientational distribution within the domains.
B) If the cylinders are perfectly aligned within the domains, then $h''(\delta-\delta')$ approaches a delta function, i.e. $h'(\delta-\delta') \rightarrow \delta[\delta-\delta']$ so that

$$\langle f(\delta)g(\delta') \rangle = \int\int f(\delta)g(\delta')\delta[\delta-\delta']h'(\delta')d\delta d\delta' = \int f(\delta)g(\delta)h'(\delta)d\delta = \langle fg \rangle' \tag{A4}$$

which means that the two functions cannot be decoupled.
C) If the two functions $g(\delta')$ and $h'(\delta')$ are strongly peaked at small values of δ', then upon integration over δ', $h''(\delta-\delta') \approx h''(\delta)$ is nearly constant over the relevant range of δ' such that

$$\begin{aligned}\langle f(\delta)g(\delta') \rangle &= \int f(\delta)g(\delta')h(\delta)d\delta = \int\int f(\delta)g(\delta')h''(\delta-\delta')h'(\delta')d\delta d\delta' \\ &= \int f(\delta)h''(\delta)d\delta \int g(\delta')h'(\delta')d\delta' = \langle f \rangle''\langle g \rangle'\end{aligned} \tag{A5}$$

Then the two functions are decoupled and the formfactor is an average of the orientational distribution within the domains, and the lattice factor is an average over the orientational distribution of the domains. This approximation is valid if the function $g(\delta')$ is sufficiently peaked and the domains are sufficiently well aligned. If $h'(\delta')$ approaches a delta function, i.e. $h'(\delta') \rightarrow \delta[\delta']$, then

$$\langle f(\delta)g(\delta') \rangle = \int f(\delta)h''(\delta)d\delta \int g(\delta')\delta[\delta']d\delta' = g(0)\langle f \rangle'' \tag{A6}$$

as in Eq. (A3).

A.2. Approximation of the Bessel function $J_1(x)$

The calculation of the formfactor of oriented polydisperse cylinders and disks involves the repeated evaluation of the Bessel function $J_1(x)$ which can be critically time-consuming. An approximation can be derived from the series expansion of the Bessel function for small values of the argument x, which is [15]

$$J_1(x) = \sum_{n=0}^{\infty} \frac{(-1)^n(x/2)^{2n+1}}{n!(n+1)!} \approx \frac{x}{2} - \frac{x^3}{16} + \cdots \tag{A7}$$

Keeping only the first two terms for the calculation of the scattering amplitude $F(x) = \left(\frac{2J_1(x)}{x}\right)^2$ (Eqs. (29) and (31)) we obtain

$$F(x) = \left(1-\frac{x^2}{8} + \cdots\right)^2 \approx 1-\frac{x^2}{4} + \cdots \tag{A8}$$

For large arguments the Bessel function has an asymptote [15]

$$J_1(x) = \sqrt{\frac{2}{\pi x}} \cos\left[x - \frac{3}{4}\pi\right] \tag{A9}$$

which yields for the corresponding asymptote of the scattering amplitude

$$F(x) = \frac{8}{\pi x^3} \cos^2\left[x - \frac{3}{4}\pi\right] \tag{A10}$$

Polydispersity of cylinder length or disk diameter will in most cases smear out the oscillation of the scattering amplitude. Taking the average of the cosine function $\langle \cos^2(z) \rangle = 1/2$, we obtain the non-oscillating asymptote of the scattering amplitude

$$F(x) = \frac{4}{\pi x^3} \tag{A11}$$

We now introduce the function

$$\tilde{F}(x) = \left(1 + \frac{\pi}{4}x^3\right)^{-1} \tag{A12}$$

which has the same limits $\lim_{x \to 0} F(x) = 1$ and $\lim_{x \to \infty} F(x) = \frac{4}{\pi x^3}$ as the scattering amplitude. It smoothly interpolates between both limits without oscillations. Fig. A1 compares the function $\tilde{F}(x)$ with the exact calculation of the scattering amplitude $\langle F(x) \rangle$ (Eqs. (29), (T5)) for a polydispersity of $\sigma = 0.1$. Polydispersity leads to smearing out of the oscillations for large arguments, so that $\langle F(x) \rangle$ becomes equal to $\tilde{F}(x)$. However, the calculation of $\tilde{F}(x)$ is 100-times faster.
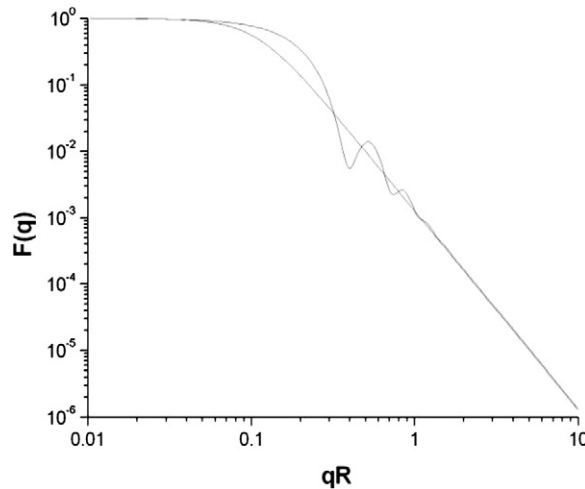

Fig. A1. Comparison of the function $\tilde{F}(qR)$ with the exact calculation of the scattering amplitude $\langle F(x) \rangle$ for a polydispersity of $\sigma = 0.1$. The non-oscillating part of the scattering amplitude can be well reproduced by $\tilde{F}(qR)$ while the numerical calculation is 100-times faster.

A.3. Approximation of the sine integral

The sine integral is defined by $Si(x) = \int_0^x \frac{\sin t}{t}\, dt$. Limiting cases are $Si(0) = 0$ and $Si(\infty) = \frac{\pi}{2}$. A useful expansion is

$$Si(x) = \sum_{n=0}^{\infty} \frac{(-1)^n x^{2n+1}}{(2n+1)(2n+1)!} = x - \frac{x^3}{3 \cdot 3!} + \frac{x^5}{5 \cdot 5!} - \frac{x^7}{7 \cdot 7!} + \cdots \tag{A13}$$

which converges also for $|x| > 1$. For large arguments, a quickly converging asymptotic expansion is given by

$$Si(x) = \frac{\pi}{2} - \frac{\cos x}{x}\left(1 - \frac{2!}{x^2} + \frac{4!}{x^4} - \cdots\right) - \frac{\sin x}{x}\left(\frac{1}{x} - \frac{3!}{x^3} + \frac{5!}{x^5} - \cdots\right) \tag{A14}$$

For numerical calculations, the first three terms of the asymptotic expansion and the first eight terms of the series expansion are sufficient. Fig. A2 compares the 8-term series expansion, the 3-term asymptotic expansion to the exact function obtained by numerical integration. By combination of both expansions, the function can be efficiently computed over the whole range of x.
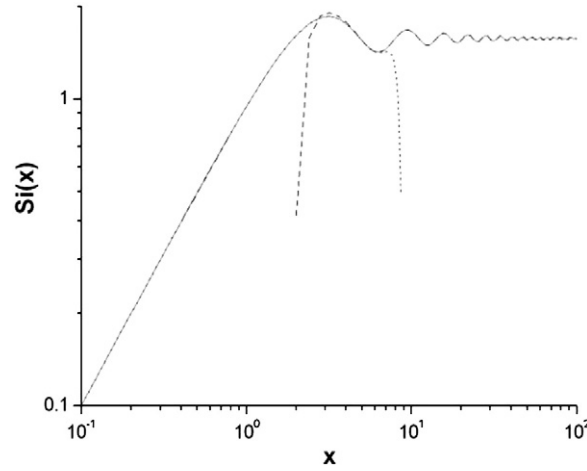
Fig. A2. The sine integral obtained by numerical integration (solid line) together with the series expansion (dotted line) and the asymptotic expansion (dashed line).

A.4. Hypergeometric functions

The hypergeometric functions $_pF_Q$ can be written in terms of series expansions

$$_pF_Q[a_1,...,a_P,b_1,...,b_Q;x] = \sum_{n=0}^{\infty} \frac{(a_1)_n(a_2)_n \cdots (a_P)_n}{(b_1)_n(b_2)_n \cdots (b_Q)_n} \frac{x^n}{n!} \tag{A15}$$

where $(c)_n$ are the Pochhammer factorials given by

$$(c)_n = \frac{\Gamma(c+n)}{\Gamma(c)} = c(c+1)(c+2)...(c+n-1) \tag{A16}$$

In the derivation of the scattering functions, the hypergeometric functions $_0F_1[b_1;x]$ (Eq. (39)), $_1F_2[a_1, b_1, b_2; x]$ (Eqs. (37), (38), (T5), and (T10)), and $_3F_2[a_1, a_2, a_3, b_1, b_2;x]$ (Eqs. (T8) and (T13)) had been considered. The sums in Eq. (A9) can be efficiently calculated via the recurrence relation of the Pochhammer factorial $(c)_{n+1} = (c+n)(c)_n$ without the need to evaluate all Gamma functions (Eq. (A16)). This enables an efficient implementation of these functions in fitting algorithms.

In cases where the expression for $\langle F_{d\perp}(q)\rangle$ and $\langle F_{d\perp}^2(q)\rangle$ involve averages of trigonometric functions over the Schulz–Zimm distribution, useful relations are

$$\left\langle x^{2n}\right\rangle = \frac{\Gamma[z+m+2n+1]}{\Gamma[z+m+1]}u^{2n} = \left(\frac{z+m+1}{2}\right)_n\left(\frac{z+m+2}{2}\right)_n(2u)^{2n} \tag{A17}$$

$$\left\langle \sin(ax)x^n\right\rangle = (z+m+1)_n u^n \frac{\sin[(z+m+n+1)\arctan(au)]}{(1+a^2u^2)^{(z+m+n+1)/2}} \tag{A18}$$

$$\left\langle \cos(ax)x^n\right\rangle = (z+m+1)_n u^n \frac{\cos[(z+m+n+1)\arctan(au)]}{(1+a^2u^2)^{(z+m+n+1)/2}} \tag{A19}$$

$$\left\langle \sin^2(ax)x^n\right\rangle = (z+m+1)_n \frac{u^n}{2}\left(1-\frac{\cos[(z+m+n+1)\arctan(2au)]}{(1+4a^2u^2)^{(z+m+n+1)/2}}\right) \tag{A20}$$

$$\left\langle \cos^2(ax)x^n\right\rangle = (z+m+1)_n \frac{u^n}{2}\left(1+\frac{\cos[(z+m+n+1)\arctan(2au)]}{(1+4a^2u^2)^{(z+m+n+1)/2}}\right) \tag{A21}$$

$$\left\langle \sin(ax)\cos(ax)x^n\right\rangle = (z+m+1)_n \frac{u^n}{2}\frac{\sin[(z+m+n+1)\arctan(2au)]}{(1+4a^2u^2)^{(z+m+n+1)/2}} \tag{A22}$$

with $u=\overline{x}/(z+1)$.

For the average $\langle x^{2n}\rangle$, the relation in terms of Pochhammer factorials as given in Eq. (A11) leads to the general relation

$$\left\langle {}_PF_Q\left[a_1,...,a_P,b_1,...,b_Q;-x^2\right]\right\rangle = {}_{P+2}F\left[a_1,...,a_P,\frac{z+m+1}{2},\frac{z+m+2}{2},b_1,...,b_Q;(-2u)^2\right]$$ (A23)

A.5. Gaussian azimuthal peak shape function

The calculation of the Gaussian azimuthal peak shape function (Eq. (84)) involves the complex error function erfi$[x]$. This function has the following limiting values [15]

$$\lim_{x\to 0}\text{erfi}[x]=\frac{2x}{\sqrt{\pi}},$$
$$\lim_{\substack{x\to 0\\y\to\infty}}(\text{erfi}[x+iy]+\text{erfi}[x-iy])=0,$$
$$\lim_{\substack{x\to\infty\\y\to 0}}(\text{erfi}[x+iy]+\text{erfi}[x-iy])=\frac{2e^{x^2}}{\sqrt{\pi}x}.$$

$$\lim_{x\to\infty}\text{erfi}[x]=\frac{e^{x^2}}{\sqrt{\pi}x}$$
$$\lim_{\substack{x\to 0\\y\to 0}}(\text{erfi}[x+iy]+\text{erfi}[x-iy])=\frac{4x}{\sqrt{\pi}},$$

Hence the limiting values of the integral $K(a)$ in Eq. (84) are $\lim_{a\to\infty}K(a)=\frac{1}{2a}$ and $\lim_{a\to 0}K(a)=2$. The azimuthal peak shape function therefore has asymptotic values of $\lim_{a\to\infty}L_\psi(q,\psi)=0$ and $\lim_{a\to 0}L_\psi(q,\psi)=\frac{1}{4\pi q^2}$ (isotropic limit).

To calculate the integral $K(a)$ over the complete range of the argument, we consider first the limit $a\to 0$ where the integral can be approximated via the series expansion of the exponential, i.e.

$$K(a)=\int_0^\pi e^{-a\psi^2}\sin\psi d\psi=\sum_{n=0}^\infty\frac{(-1)^n a^n}{n!}\int_0^\pi \psi^{2n}\sin\psi d\psi$$
$$=2-\left(\pi^2-4\right)a+\frac{\left(48-12\pi^2+\pi^4\right)a^2}{2}-\frac{\left(-1440+360\pi^2-30\pi^4+\pi^6\right)a^3}{6}+\cdots$$ (A24)

For $a\to\infty$ the integral can be approximated via the series expansion of the sine-function, i.e.

$$K(a)=\int_0^\pi e^{-a\psi^2}\sin\psi d\psi=\sum_{n=0}^\infty\frac{(-1)^n}{(2n+1)!}\int_0^\pi e^{-a\psi^2}\psi^{2n+1}d\psi$$
$$=\sum_{n=0}^\infty\frac{(-1)^n}{(2n+1)!}\frac{\left(\Gamma[n+1]-\Gamma\left[n+1,a\pi^2\right]\right)}{2a^{n+1}}=\frac{\left(1-e^{-a\pi^2}\right)}{2a}-\frac{1-e^{-a\pi^2}\left(1+a\pi^2\right)}{12a^2}+\frac{2-e^{-a\pi^2}\left(2+2a\pi^2+a^2\pi^4\right)}{240a^3}-\frac{6-e^{-a\pi^2}\left(6+6a\pi^2+3a^2\pi^4+a^3\pi^6\right)}{10080a^4}+\cdots$$ (A25)

Fig. A3 compares the 4-term series expansion and the 4-term asymptotic expansion to the exact function obtained by numerical integration. By combination of both expansions, the function can be computed over the whole range of a.
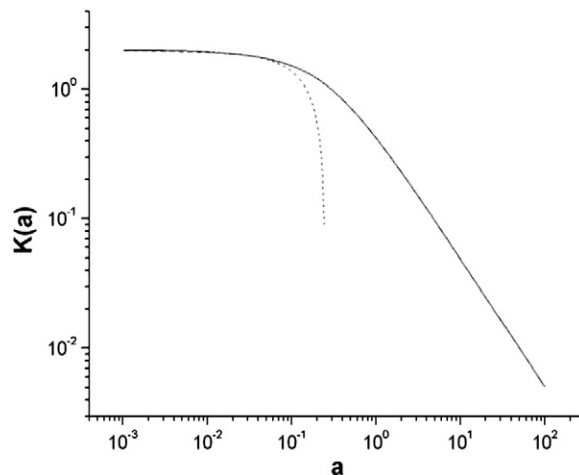

Fig. A3. Function $K_3(a)$ calculated by numerical integration (solid line) together with its series expansion (dotted line) and asymptotic expansion (dashed line).

A.6. Lorentzian azimuthal peak shape function

At low b the integral in Eq. (88) can be approximated via the series expansion of the Lorentzian [15], i.e.

$$K(b) = \int_0^\pi \frac{1}{1 + b\psi^2} \sin\psi d\psi = \sum_{n=0}^\infty (-1)^n b^n \int_0^\pi \psi^{2n} \sin\psi d\psi = 2 - \left(\pi^2 - 4\right)b + \left(48 - 12\pi^2 + \pi^4\right)b^2 - \left(-1440 + 360\pi^2 - 30\pi^4 + \pi^6\right)b^3 + \cdots$$

(A26)

At high b the integral can be approximated via the series expansion of the sine-function, i.e.

$$K_3(b) = \int_0^\pi \frac{1}{1 + b\psi^2} \sin\varphi d\varphi = \sum_{n=0}^\infty \frac{(-1)^n}{(2n+1)!} \int_0^\pi \frac{1}{1 + b\psi^2} \psi^{2n+1} d\psi$$

$$= \sum_{n=0}^\infty \frac{(-1)^n}{(2n+1)!} \frac{\pi^{2(n+1)} {}_2F_1\left[1, n+1, n+2; -b\pi^2\right]}{2(n+1)} = \frac{\ln\left(1 + b\pi^2\right)}{2b} - \frac{b\pi^2 - \ln\left(1 + b\pi^2\right)}{12b^2} + \frac{-2b\pi^2 + b^2\pi^4 + 2\ln\left(1 + b\pi^2\right)}{480b^2} -$$

$$- \frac{b\pi^2\left(6 - 3b\pi^2 + 2b^2\pi^4\right) - 6\ln\left(1 + b\pi^2\right)}{60480b^4} + \cdots$$

(A27)

Fig. A4 compares the 4-term series expansion and the 4-term asymptotic expansion to the exact function obtained by numerical integration. By combination of both expansions, the function can be computed over the whole range of b.
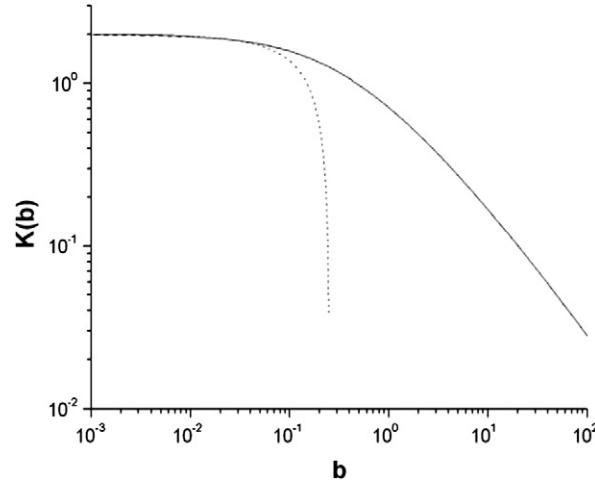

Fig. A4. Function $K(b)$ calculated by numerical integration (solid line) together with its series expansion (dotted line) and asymptotic expansion (dashed line).

The limiting values of the integral in Eq. (88) are $\lim\limits_{b\to\infty} K_3(b) = \dfrac{\ln\left(b\pi^2\right)}{2b}$ and $\lim\limits_{b\to 0} K_3(b) = 2$. The normalized peak shape function therefore has asymptotic values of $\lim\limits_{b\to\infty} L_3(q, \psi) = 0$ and $\lim\limits_{b\to 0} L_3(q, \psi) = \dfrac{1}{4\pi q^2}$ (isotropic limit).

A.7. Pseudo-Voigt azimuthal peak shape function

The Pseudo-Voigt peak shape function is given by linear combination of the Lorentz and Gaussian function and is therefore given by

$$L_3(\psi) = \frac{1}{2\pi q^2} \frac{\eta\left(1 + b\psi^2\right)^{-1} + (1-\eta)\exp\left[-a\psi^2\right]}{\eta K_3(b) + (1-\eta)K_3(a)}$$

(A28)

In the isotropic case all this function has a value of $\lim\limits_{\substack{a\to 0 \\ b\to 0}} L_d(\psi) = \dfrac{1}{4\pi q^2}$.

A.8. Pearson VII-type peak shape functions (Modified Lorentzians)

The normalized Pearson-VII function can be given in terms of the integral peak width B [47]

$$L(\psi) = \frac{1}{B\left(1 + \dfrac{\pi\Gamma^2[\beta - 1/2]q^2\psi^2}{\Gamma^2[\beta]B^2}\right)^\beta}$$

(A29)

where the integral peak width B is related to the peak width δ (FWHM) by

$$\frac{B}{\delta} = \frac{\pi^{1/2}}{2}\frac{\Gamma[\beta-1/2]}{\Gamma[\beta]\left(2^{1/\beta}-1\right)^{1/2}} \tag{A30}$$

The ratio B/δ is a measure of the sharpness of the peak-shape function, which increases with decreasing β. The Pearson-VII function reduces to the Modified Lorentzian I for the case $\beta = 2$

$$L(\psi) = \frac{1}{B\left(1+\frac{\pi^2 q^2\psi^2}{4B^2}\right)^2} \tag{A31}$$

with $\dfrac{B}{\delta} = \dfrac{\pi}{4}\dfrac{1}{\left(2^{1/2}-1\right)^{1/2}} = 1.22033....$ In case of $\beta = 3/2$ one obtains the Modified Lorentzian II or Intermediate Lorentzian function given by

$$L(\psi) = \frac{1}{B\left(1+\frac{4q^2\psi^2}{B^2}\right)^{3/2}} \tag{A32}$$

with $\dfrac{B}{\delta} = \dfrac{1}{\left(2^{2/3}-1\right)^{1/2}} = 1.30477....$ In case of $\beta = 1$ it reduces to the Lorentzian

$$L(\psi) = \frac{1}{B\left(1+\frac{\pi^2 q^2\psi^2}{B^2}\right)} \tag{A33}$$

with $\dfrac{B}{\delta} = \dfrac{\pi}{2} = 1.5708...,$ for which Eq. (A27) is identical to Eqs. (82) and (83). The Gaussian peak shape function as given in terms of the integral peak width is given by

$$L(\psi) = \frac{1}{B}\exp\left[-\frac{\pi q^2\psi^2}{B^2}\right] \tag{A34}$$

with $\dfrac{B}{\delta} = \dfrac{\pi^{1/2}}{2(\ln 2)^{1/2}} = 1.06447....$ The integral peak width B is related to the Gaussian peak width δ_G via $B = \dfrac{\pi\delta_G}{2}$. Inserted into Eq. (A28) it becomes identical to Eqs. (82) and (83).

The Pearson VII function is of the form

$$L(\psi) = \frac{1}{(1+c\psi^2)^\beta} \tag{A35}$$

with $c = \dfrac{\pi\Gamma^2[\beta-1/2]q^2}{\Gamma^2[\beta]B^2}$. The corresponding integral in Eq. (81) does not have an analytical solution. Therefore for small c we approximated the integral via the series expansion of the Pearson function

$$
\begin{aligned}
K(c) = \int_0^\pi \frac{1}{(1+c\psi^2)^\beta}\sin\psi\, d\psi &= \sum_{n=0}^\infty \frac{(-1)^n\Gamma[\beta+n]c^n}{\Gamma[\beta]n!}\int_0^\pi \psi^{2n}\sin\psi\, d\psi = \\
&= 2-\left(\pi^2-4\right)\beta c + \frac{\left(48-12\pi^2+\pi^4\right)\beta(\beta+1)c^2}{2} - \frac{\left(-1440+360\pi^2-30\pi^4+\pi^6\right)\beta(\beta+1)(\beta+2)c^3}{6} + \cdots
\end{aligned} \tag{A36}
$$

At high c the integral can be approximated via the series expansion of the sine-function, i.e.

$$
\begin{aligned}
K(c) = \int_0^\pi \frac{1}{(1+c\psi^2)^\beta}\sin\varphi\, d\varphi &= \sum_{n=0}^\infty \frac{(-1)^n}{(2n+1)!}\int_0^\pi \frac{1}{(1+c\psi^2)^\beta}\psi^{2n+1}d\psi \\
&= \sum_{n=0}^\infty \frac{(-1)^n}{(2n+1)!}\frac{\pi^{2(n+1)}{}_2F_1\left[\beta,n+1,n+2;-c\pi^2\right]}{2(n+1)} \\
&= \frac{1-\left(1+c\pi^2\right)^{1-\beta}}{2(\beta-1)c} - \frac{-1+c^2\pi^2-\beta c\pi^2\left(1+c\pi^2\right)+\left(1+c\pi^2\right)^\beta}{12(\beta-2)(\beta-1)\left(1+c\pi^2\right)^\beta c^2} + \\
&\quad + \frac{-\beta^2 c^2\pi^4\left(1+c\pi^2\right)+\beta c\pi^2\left(-2+c\pi^2+3c^2\pi^4\right)+2\left[-1-c^3\pi^6+\left(1+c\pi^2\right)^\beta\right]}{240(\beta-3)(\beta-2)(\beta-1)\left(1+c\pi^2\right)^\beta c^3} \\
&\quad - \frac{-\beta^3 c^3\pi^6\left(1+c\pi^2\right)+3\beta^2 c^2\pi^4\left(-1+c\pi^2+2c^2\pi^4\right)-\beta c\pi^2\left(6-3c\pi^2+2c^2\pi^4+11c^3\pi^6\right)+6\left(-1+c^4\pi^8+\left(1+c\pi^2\right)^\beta\right)}{10080(\beta-4)(\beta-3)(\beta-2)(\beta-1)\left(1+c\pi^2\right)^\beta c^4} + \cdots
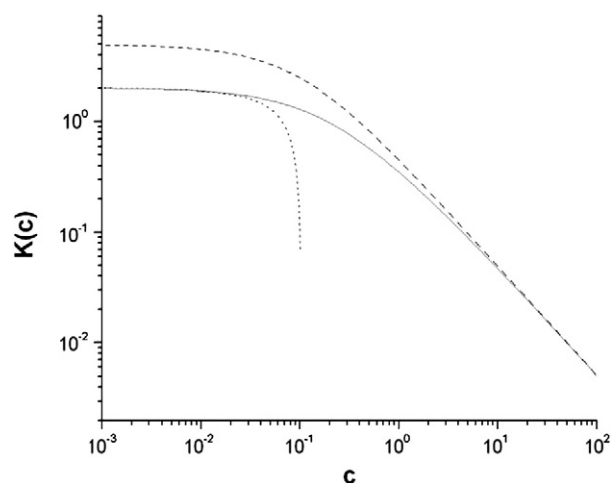\end{aligned} \tag{A37}
$$

Fig. A5. Function $K(c, \beta = 2)$ calculated by numerical integration (solid line) together with its series expansion (dotted line) and asymptotic expansion (dashed line). There is a large intermediate range where the function can only be evaluated by numerical integration.

The limiting values of the integral are $\lim_{c \to 0} K(c) = 2$ ("isotropic limit") and $\lim_{c \to \infty} K_3(c) = \frac{1}{2(\beta-1)c}$. The azimuthal peak shape function has asymptotic value of $\lim_{c \to 0} L_3(\psi) = \frac{1}{4\pi q^2}$ (isotropic limit).

References

[1] Förster S, Plantenberg T. Angew Chem Int Ed 2002;41:688.
[2] Kotlarchyk M, Chen SH. J Chem Phys 1983;79:2461.
[3] Förster S, Timman A, Konrad M, Schellbach C, Meyer A, Funari SS, et al. J Phys Chem B 2005;109:1347.
[4] Lindner P. In: Lindner P, Zemb T, editors. Neutrons, X-rays and Light: Scattering Methods Applied to Soft Condensed Matter. Amsterdam: Elsevier; 2002.
[5] Schellbach, C, Diploma Thesis, University of Hamburg (2003).
[6] Förster S. Top Curr Chem 2003;226:1.
[7] Giacovazzo C. Fundamentals of Crystallography. Oxford University Press; 2002.
[8] Ruland W, personal communication.
[9] Wolff T, Ph.D. thesis, University of Marburg (1994).
[10] Förster S, Timman A, Schellbach C, Fromsdorf A, Kornowski A, Weller H, et al. Nat Mater 2007;6:888.
[11] Förster S, Burger C. Macromolecules 1998;31:879.
[12] Pedersen JS. Adv Colloid Interface Sci 1997;70:171.
[13] Förster S, Konrad M, Lindner P. Phys Rev Lett 2005;94:017803.
[14] Saranathan V, Osuji CO, Mochrie SGJ, Noh H, Narayanan S, Sandy A, et al. Proc Natl Acad Sci 2010;107:11676–81.
[15] Abramowitz M, Stegun I. Handbook of Mathematical Functions; 1965. Dover, New York.
[16] Ruland W, Smarsly B. J Appl Cryst 2005;38:78.
[17] Ruland W, Smarsly B. J Appl Cryst 2007;40:409.
[18] Ruland W, Tompa H. Acta Cryst 1968;A24:93.
[19] Ruland W, Smarsy B. Acta Cryst 2004;37:575.
[20] Van der Veen JF. Materials Research using Synchrotron Radiation; 2007.
[21] Iizuka N, Bodycomb J, Hasegawa H, Hashimoto T. Macromoleucles 1998;31:7256.
[22] Caille ACR. Acad Sci Paris 1972;B274:891.
[23] Nallet F, Laversanne R, Roux D. J Phys II (France) 1993;3:487.
[24] Molino FR, Berret JF, Porte G, Diat O, Lindner P. Eur Phys J B 1998;3:59–72.
[25] McConnell GA, Lin MY, Gast AP. Macromolecules 1995;28:6754–64.
[26] Diat O, Porte G, Berret JF. Phys Rev B 1996;54:14869–72.
[27] Park MJ, Char K, Bang J, Lodge TP. Langmuir 2005;21:1403–11.
[28] Leyh B, Creutz S, Gaspard JP, Bourgaux C, Jerome R. Macromolecules 1998;31:9258–64.
[29] Deng Y, Young RN, Ryan AJ, Fairclough JPA, Norman AI, Tack RD. Polymer 2002;43:7155–60.
[30] Park MJ, Bang J, Harada T, Char K, Lodge TP. Macromolecules 2004;37:9064–75.
[31] Ackerson BJ, Hayter JB, Clark NA, Cotter L. J Chem Phys 1986;84:2344–9.
[32] Ashdown S, et al. Langmuir 1990;6:303–7.
[33] Laun HM, et al. J Rheol 1992;36:743–87.
[34] Panine P, Narayanan T, Vermant J, Mewis J. Phys Rev E 2002;66:022401.
[35] Vos WL, Megens M, v Kats CM, Bösecke P. Langmuir 1997;13:6004–8.
[36] Azaroff LV. Elements of x-ray crystallography. New York: McGraw-Hill; 1968.
[37] Forster S, Apostol L, Bras W. J Appl Cryst 2010;43:639–46.
[38] http://www.chemie.uni-hamburg.de/pc/sfoerster/software.html.
[39] Schoen Alan H. NASA Technical Note TN D-5541; 1970.
[40] Hajduk DA, Harper PE, Gruner SM, Honeker CC, Kim G, Thomas EL, et al. Macromolecules 1994;27:4063–75.
[41] Schulz MF, Bates FS, Almdal K, Mortensen K. Phys Rev Lett 1994;73:86–9.
[42] Förster S, Khandpur AK, Zhao J, Bates FS, Hamley IW, Ryan AJ, et al. Macromolecules 1994;27:6922–35.
[43] Scattering image courtesy of A. J. Ryan, University of Sheffield.
[44] Zielske K. Ph.D. thesis, University of Hamburg, 2009.
[45] Fischer S, Ph.D. thesis, University of Hamburg, 2009.
[46] Schellbach, Ph.D. thesis, University of Hamburg, 2007.
[47] Ida T. J Appl Cryst 2008;41:393–401.